Searches for rare nuclear decays in the LUX-ZEPLIN experiment

Aiham K. Al Musalhi

St Catherine's College

University of Oxford

A thesis submitted for the degree of

Doctor of Philosophy

Trinity 2023

> No thinking being lives who, at some luminous point of his life of thought, has not felt himself lost amid the surges of futile efforts at understanding, or believing, that anything exists greater than his own soul.

— Edgar Allan Poe, *Eureka* (1848)

Abstract

The fundamental nature of dark matter stands as one of the greatest mysteries in physics. A compelling body of evidence indicates that dark matter accounts for 84% of the total matter density of the universe, and yet the detection of its constituent particles remains elusive. Stationed deep underground, the LUX-ZEPLIN (LZ) experiment utilises several tonnes of xenon in a dual-phase time projection chamber to conduct direct searches for particle dark matter. A world-leading limit was recently set by the LZ experiment for interactions between nucleons and weakly interacting massive particles, the most promising dark matter candidate. The work of this thesis leverages the unprecedented sensitivity and versatility of the LZ detector to expand the scientific programme to searches for rare phenomena beyond dark matter.

A comprehensive background model of detector materials is constructed in this work, using a combination of real data and simulations within a novel approach, as informed by expectations from an extensive radioassay campaign. This result is primarily applicable to searches for hypothesised neutrinoless double beta decays, the observation of which would shed light on the underlying properties of massive neutrinos, and is tied to the matter-antimatter asymmetry of the universe. With a large quantity of xenon, an ultra-low background environment, and excellent energy resolution, LZ is projected to achieve a sensitivity that is competitive with dedicated experiments.

The first LZ measurement of ^{124}Xe decay through the process of two-neutrino double electron capture is also presented here. This is the rarest nuclear decay observed to date, with a half-life that significantly exceeds the age of the universe. The dominant ^{125}I background is constrained with a detailed neutron activation model, and the exposure is maximised with an optimised fiducial volume. A half-life of $(1.09 \pm 0.18_{\text{stat}} \pm 0.03_{\text{sys}}) \times 10^{22}$ years is observed with a statistical significance of 7σ. In future runs, the discovery of even rarer ^{124}Xe decay modes, namely two-neutrino electron capture with associated positron emission, will be within the physics reach of LZ.

Declaration

I hereby declare that the work presented in this thesis is my own, and that any information derived from other sources has been referenced appropriately.

Aiham K. Al Musalhi
September 2023

The work contained in this thesis has directly contributed to the following papers:

- J. Aalbers *et al.* (LZ Collaboration), "Background determination for the LUX-ZEPLIN dark matter experiment", *Phys. Rev. D*, vol. 108, no. 1, p. 012 010, 2022.
- J. Aalbers *et al.* (LZ Collaboration), "Two-neutrino double electron capture of ^{124}Xe in the LUX-ZEPLIN experiment", (in preparation).

Acknowledgements

The time I have spent at Oxford has provided many opportunities for me to grow and reflect both as a person and as a scientist. Though I hope that I have at least made my mark with this thesis, what has been accomplished stems from the support of many others. To those who have shared their time with me, I dedicate this page to you.

First of all, I would like to thank my supervisor Hans for his wisdom and guidance throughout this DPhil. I also owe special thanks to Amy – the insights gained from our countless discussions have been immensely valuable. To my peers in the Oxford LZ group: Andrew, Niamh, Dan, Sparshita, Josh, and Nick, I'm grateful for your camaraderie, and hope that you continue to find pride and joy in your work. I also extend my thanks to the LZ collaboration: Kevin, Alex, Guilherme, Ibles, Theresa, Kim, Nicolas, and many more, for their commitment and advice.

I'm thankful to my parents and sisters for keeping me grounded, and for reminding me to stop for a breath every once in a while. To my dear friends: Mohit, Siyuan, Claude, Anh, and Casey, I appreciate you for keeping me humble, and I cherish our late night chats and escapades. Most importantly, I'm indebted to Jade for her unwavering love and encouragement, and for always inspiring me to be better.

Contents

List of Figures

List of Tables

List of Abbreviations

BACCARAT . LZ simulation package built on GEANT4
CMB . . . . . cosmic microwave background
CSD . . . . . . calibration source deployment
DAQ . . . . . . data acquisition
DD . . . . deuterium-deuterium
DER . . . . . . detector electronics response
EC . . . . electron capture
eCDF . . . . . empirical cumulative distribution function
ER . . . . electronic recoil
ET . . . . effective theory
FV . . . . fiducial volume
GXe . . . . . . gaseous xenon
HX . . . . heat exchanger
ICV . . . . . . inner cryostat vessel
iRRS . . . . . . in-line radon reduction system
KS . . . . Kolmogorov-Smirnov
ΛCDM . . . . Lambda cold dark matter
LXe . . . . . . liquid xenon
LSR . . . . . . local standard of rest
LZ . . . . LUX-ZEPLIN
MACHO . . . massive astrophysical compact halo object
MS . . . . multiple scatter
MSSI . . . . . multiple scatter single ionisation
NEST . . . . . Noble Element Simulation Technique

NME . . . . . nuclear matrix element

NR . . . . nuclear recoil

NSM . . . . . . nuclear shell model

OCV . . . . . . outer cryostat vessel

OD . . . . outer detector

PBH . . . . . . primordial black hole

PDF . . . . . . probability density function

phd . . . . . . photons detected

PLR . . . . . . profile likelihood ratio

PMT . . . . . . photomultiplier tube

PTFE . . . . . polytetrafluoroethylene

QRPA . . . . . quasiparticle random-phase approximation

RFR . . . . . . reverse-field region

ROI . . . . . . region of interest

S1c . . . . corrected primary scintillation signal

S2c . . . . corrected secondary scintillation signal

SD . . . . spin-dependent

SI . . . . spin-independent

SR1 . . . . . . Science Run 1

SS . . . . single scatter

SURF . . . . . Sanford Underground Research Facility

TeVeS . . . . . tensor-vector-scalar

TPC . . . . . . time projection chamber

VUV . . . . . . vacuum ultraviolet

WIMP . . . . weakly interacting massive particle

$0/2\nu\beta\beta$ . . . . neutrinoless/two-neutrino double beta

$0/2\nu$2EC . . . neutrinoless/two-neutrino double electron capture

$0/2\nu$ECβ^+ . . neutrinoless/two-neutrino electron capture & positron emission

$0/2\nu\beta^+\beta^+$ . . neutrinoless/two-neutrino double positron emission

Introduction

The Standard Model of particle physics has successfully described a variety of precise experimental measurements, and represents the culmination of over a century of innovation, collaboration, and discovery. However, many questions are left unanswered, and a substantial part of the universe remains unknown. There is compelling astrophysical evidence that points to the existence of dark matter – a non-luminous substance that accounts for 84% of the total mass density of the universe. A worldwide experimental effort has been involved in the search for particle dark matter, and thus far it has eluded detection. The LUX-ZEPLIN (LZ) experiment conducts direct searches for dark matter through scatters with ordinary matter, utilising seven active tonnes of xenon in a dual-phase time projection chamber stationed deep underground. The focus of the work presented in this thesis is on leveraging the high sensitivity and versatility of the LZ detector to probe for rare physics beyond the primary dark matter search. A breakdown of the content structure is given below.

Chapter 1 motivates the existence of dark matter with a summary of the key pieces of observational evidence, and lists particle candidates with desirable properties for dark matter. This is followed by an overview of complementary dark matter searches, with a focus on direct detection. The main detector technologies are reviewed along with the current status of the field.

Chapter 2 briefly introduces the theoretical motivation for studies of second-order weak decays, and how their measurement is linked to the fundamental nature of massive neutrinos. Processes such as double beta decays and double electron captures are highlighted, as well as hypothetical neutrinoless interactions in which neutrinos behave as their own antiparticles. The experimental strategy for the detection of such rare nuclear decays is discussed, and recent results are summarised for a range of isotopes and experiments.

Chapter 3 outlines the operational principles, detector systems, analysis procedures, and recent results of the LZ experiment. The underlying mechanisms for signal production in a xenon medium are covered in the context of the dual-phase xenon time projection chamber detector technology.

Chapter 4 describes the construction of a background model of detector materials, as informed by an extensive radioassay campaign. This features numerous components, which translates into an inflated number of parameters. A novel sub-volume approach and a component grouping algorithm are developed to reduce the level of complexity, whilst still exploiting the full set of assay measurements. A modified energy calibration is performed to enhance the fit robustness, along with additional data-driven corrections to optimise the energy reconstruction and resolution. The impact of the fit results is evaluated for the LZ sensitivity to neutrinoless double beta decays of ^{136}Xe.

Chapter 5 delves into a self-contained analysis of ^{124}Xe decay through the process of two-neutrino double electron capture. This is the rarest nuclear decay observed to date, with a half-life that significantly exceeds the age of the universe. The first LZ measurement of the half-life is conducted, which establishes the foundations for searches of even rarer exotic decays in future runs of the experiment.

The final chapter provides a summary of the key themes and findings of this thesis, and concludes with an outlook on future work, both in the context of LZ and the next generation of dark matter detectors.

1 Dark matter

Humankind has studied the skies and motions of celestial bodies throughout history, seeking to comprehend the nature of its existence within a vast universe. With each scientific era, technological advancements enabled the discovery of phenomena that were previously imperceptible. The term 'dark matter' is not exclusive to the modern definition – it was used by astronomers as early as the 19th century to describe objects that were effectively invisible, such as dark planets, stars, and nebulae [1]. Over the course of the 20th century, collections of astrophysical observations hinted at the presence of an intrinsically non-luminous substance, discernible only by its gravitational influence on surrounding objects. The key pieces of evidence motivating the dark matter hypothesis are discussed in this chapter, along with a formal definition of its properties and its role in cosmology. A summary of the main dark matter candidates is also given, as well as a brief overview of the current state of experimental searches for dark matter.

1.1 Motivation and evidence for dark matter

With mounting observational evidence supporting the existence of dark matter, it has become established as a core ingredient of modern cosmology. As covered in the next few sections, these observations span a range of scales, and provide insight into some of the properties of dark matter.

1.1.1 Velocity dispersions

In the 1930s, Zwicky produced an estimate for the mass of the Coma Cluster using the virial theorem, which relates the time-averaged kinetic energy and potential energy of a given system [2, 3]. Similar dynamical estimates of the mass contained by galaxies had already been previously attempted in order to interpret the anisotropic distribution of stars in the sky [4–8], though it was initially concluded that the amount of dark matter was less than that of visible matter, and that it predominantly consisted of faint stars. With a measured velocity dispersion of 700 km/s and a few simplifying assumptions for the number of galaxies and their luminosities, Zwicky obtained a remarkably high mass-to-light ratio of ∼500 for the Coma Cluster, which suggested that there exists a significantly larger proportion of non-luminous mass driving the high velocity dispersion. This result was eventually followed by a number of publications reporting elevated mass-to-light ratios for more galaxy clusters [9], leaving the astronomical community divided.

1.1.2 Galactic rotation curves

The consensus began to shift during the 1970s, with refined measurements for the rotation curve of the Andromeda Galaxy (M31). For a galaxy with a mass distribution $M(r)$, the orbital velocity $v(r)$ of the stars and gas comprising it is described by Newtonian dynamics as

$$v(r) = \sqrt{\frac{GM(r)}{r}}, \tag{1.1}$$

where G is the gravitational constant and r is the radial distance from the galactic centre. With a spherical mass concentration of radius R and constant density $\rho(r) \equiv \rho$ as an approximation for $M(r)$, the velocity is expected to grow linearly as $v(r) \propto r$ for $(r \leq R)$, and then subsequently decay as $v(r) \propto r^{-1/2}$ for $(r > R)$, beyond the region where most visible matter is situated. However, Rubin and Ford demonstrated with precise spectroscopic measurements that $v(r)$ approaches a constant value at high radii for M31 [10], in agreement with previous radio measurements by Roberts [11] and initial observations by Babcock [12].

The same behaviour was soon documented for numerous galaxies [13–15], and ultimately provided a strong case for the presence of great amounts of additional non-luminous mass in the outer regions of galaxies [16, 17].

To reproduce constant orbital velocities at large radii, as exemplified by the galactic rotation curve for NGC 3198 in Figure 1.1, the mass distribution must vary as $M(r) \propto r$, which requires that the density varies as $\rho(r) \propto r^{-2}$; this contribution can be introduced in the form of a spherical dark matter halo surrounding the galaxy [18]. Since the formation of flat galactic disks depends on radiative cooling processes, an assumed spherical distribution for the halo implies that dark matter does not cool efficiently, which suggests that it is electrically neutral and effectively collisionless [19].

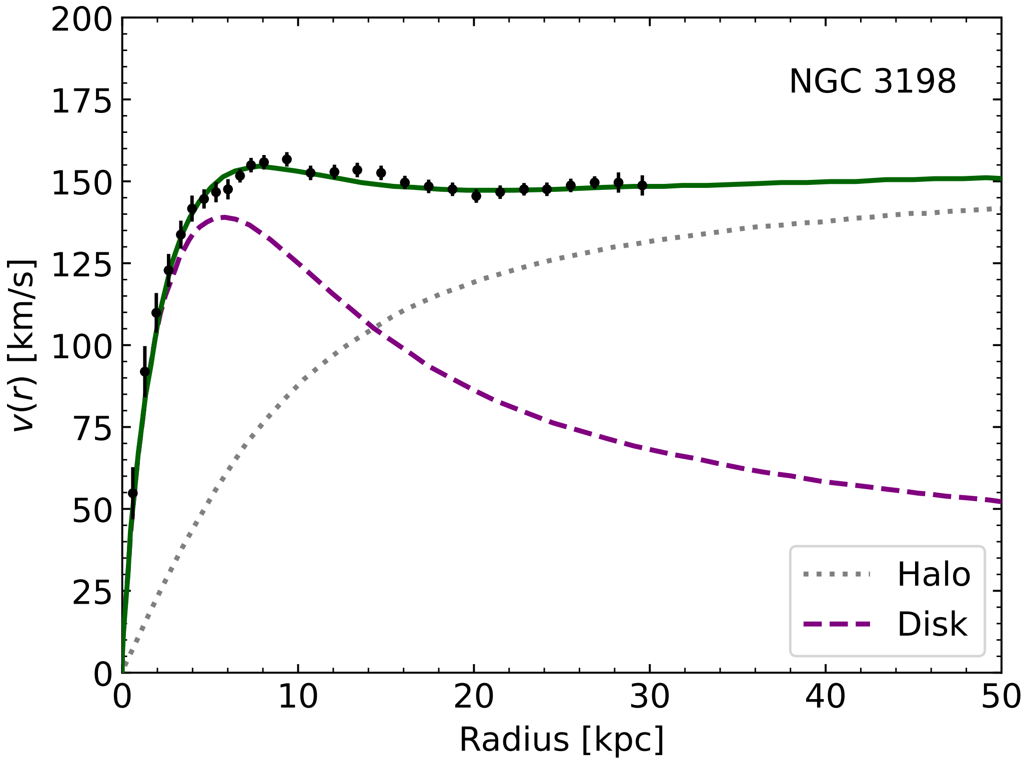

Figure 1.1: Galactic rotation curve for NGC 3198, a barred spiral galaxy in the Virgo Supercluster, with the modelled optical disk and dark matter halo components included. Data points and curves were digitised and reproduced from [20].

1.1.3 Gravitational lensing

General relativity predicts the deflection of light along curvatures in spacetime induced by massive objects – a phenomenon referred to as gravitational lensing [21]. Manifestations of this effect range from minute distortions to arcs and duplicates in astronomical images. The total mass of intervening objects along the path of observed light can be inferred by analysing the extent of these distortions [22]. This enables estimates of the mass-to-light ratio without relying on dynamical measurements [23], as well as mapping of large-scale dark matter structures [24, 25].

A prominent case study is that of the Bullet Cluster, which features the aftermath of a collision between two galaxy clusters [26, 27]. As visualised by the image in Figure 1.2, the event resulted in spatial separation of the dense intergalactic plasma as mapped by corresponding X-ray emission, whereas the stars and galaxies essentially passed by each other unimpeded. Weak gravitational lensing reveals that the expected distribution of mass does not coincide with the centroid from visible baryonic matter – it is more consistent with the presence of two dominant populations of collisionless dark matter. Similar configurations have been observed for other merging cluster systems, such as Abell 2146 [28] and A1758 [29].

1.1.4 The cosmic microwave background

Approximately 380,000 years after the Big Bang, the universe reached the end of the recombination epoch; it had cooled sufficiently from expansion to allow for the formation of neutral light elements. After this transition from a radiation-dominated era—in which photons were trapped by Thomson scattering in an opaque plasma—to a matter-dominated one, the universe became transparent for the first time as photons decoupled from the newly-formed atoms [30]. Remnant free-streaming photons from this surface of last scattering are observed today as the cosmic microwave background (CMB), the earliest known snapshot of the universe [31].

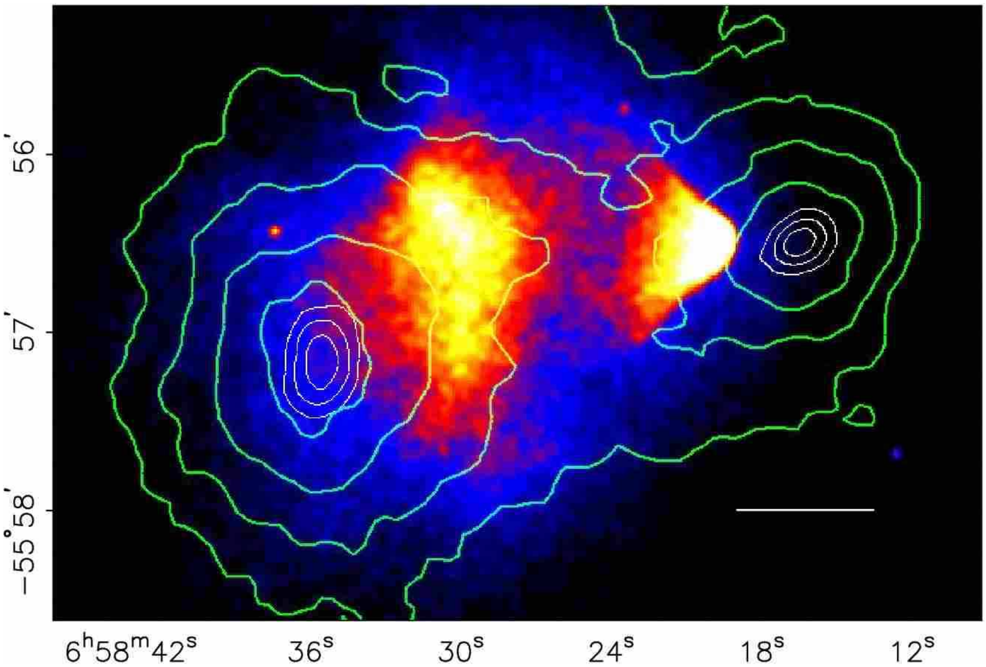

Figure 1.2: Map of the Bullet Cluster imaged by the Chandra X-ray Observatory. X-ray emission by the hot intergalactic gas is indicated with a red colour map. The contour lines denote the weak lensing signal reconstruction, with the inferred mass distribution highlighted in blue. A 200 kpc white bar is included for scale. This diagram was obtained from [27].

In the early universe, the interplay between radiation pressure and gravitational attraction induced density waves in the photon-baryon plasma known as baryon acoustic oscillations. These produced fluctuations in the matter density, which manifest as temperature anisotropies in precise measurements of the CMB black-body spectrum [32, 33]. The anisotropies are studied by decomposing the CMB map of the sky into spherical harmonics to separate it into various angular scales. The observed temperature fluctuations are displayed in a power spectrum as shown in Figure 1.3, with a larger multipole moment ℓ representing a smaller angular scale and vice versa. The peak positions and relative heights are related to various cosmological parameters; the curvature of the universe can be determined from the angular scale of the first peak, whereas the ratio of odd and even peaks provides information about the baryonic and dark matter densities [34, 35]. With lower proportions of dark matter, reduced baryon drag would enhance the odd acoustic peaks associated with compression [36].

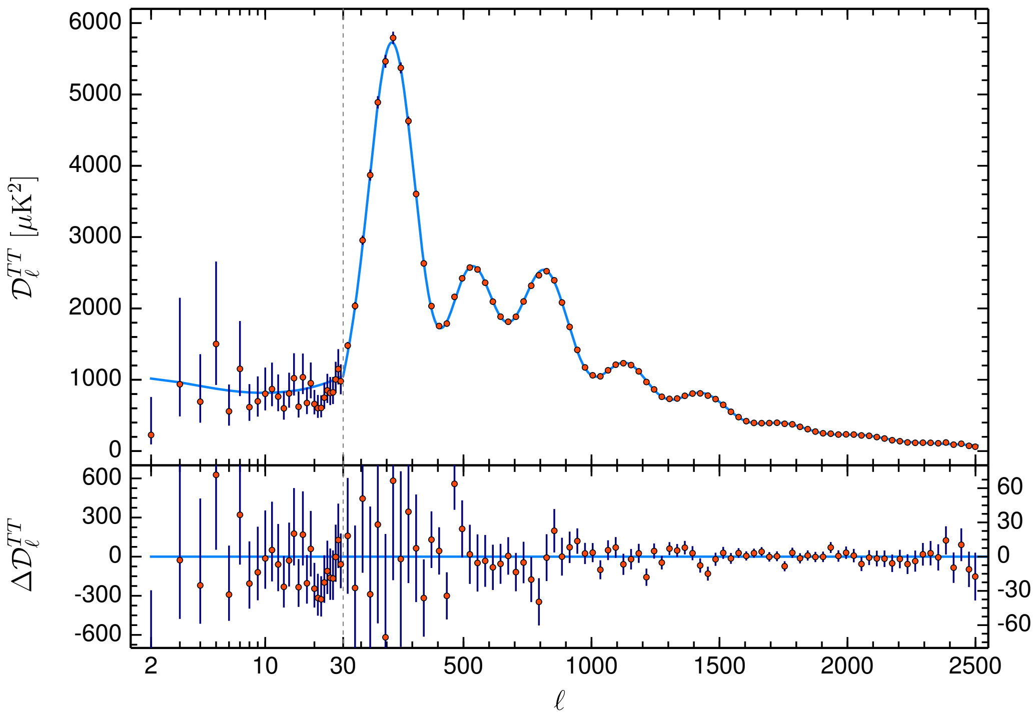

Figure 1.3: The angular power spectrum of temperature anisotropies in the cosmic microwave background, as a function of angular scale expressed in terms of the spherical multipole moment ℓ. Larger values of ℓ correspond to smaller angular scales, with the primary peak at $\ell \sim 225$ corresponding to 1°. The data is well-matched by a fit of the standard model of Big Bang cosmology. These measurements were conducted by the Planck collaboration, with a level of precision down to one part in 10^5. The plot was sourced from [35].

Dark matter is hypothesised to play an important role in the formation of large-scale structures in the universe. In the radiation era, whilst small-scale fluctuations in the baryonic matter density were erased by photon pressure, dark matter over-densities would have already begun to cluster, creating gravitational wells that would seed the growth of structures after decoupling [37–39]. This requires that dark matter is both collisionless and non-relativistic (cold), such that its ability to accumulate is not hindered. Understanding the contribution of dark matter to structure evolution has been mainly driven by N-body numerical simulations, which generally display hierarchical clustering through a range of scales, spanning from condensation of galaxies within halos to filament networks of dark matter woven into a cosmic web [40, 41].

1.1.5 The ΛCDM model

The Lambda cold dark matter (ΛCDM) model, commonly referred to as the standard model of cosmology, successfully provides a reasonable account for observed astrophysical phenomena such as the aforementioned baryon acoustic oscillations and large-scale structure formation, as well as the measured abundances for hydrogen, deuterium, and helium [42, 43]. It also describes the accelerating expansion of the universe with the inclusion of the cosmological constant Λ, which is associated with dark energy. Key assumptions of the standard ΛCDM model include the cosmological principle—the homogeneous and isotropic distribution of matter at large scales—and that there exist five basic cosmological constituents: dark energy, dark matter, baryonic matter, CMB radiation, and relic neutrinos that decoupled from matter very shortly after the Big Bang. Violations of the core assumptions, such as that of homogeneity by observation of enormous structures like the ∼310 Mpc-long Sloan Great Wall [44], are usually sources of shortcomings; the development of model extensions to address these challenges is an active area of research [45]. Fits of ΛCDM models involve six independent free parameters, from which relative density parameters for dark energy Ω_Λ, dark matter Ω_c, and baryonic matter Ω_b can be derived [46]. The latest constraints from the Planck collaboration are:

$$\Omega_\Lambda = (0.68890 \pm 0.00560),$$
$$\Omega_c = (0.26070 \pm 0.00199),$$
$$\Omega_b = (0.04898 \pm 0.00031),$$

which imply dark matter accounts for approximately $(83.8 \pm 1.6)\%$ of the total mass density of the universe [35].

1.2 Dark matter candidates

The conclusions outlined in the previous sections paint a basic picture of the expected properties of particle dark matter; proposed candidates must adhere to a minimal set of model-independent criteria in order to maintain consistency with observations across different astronomical scales [47]. The main requirements are that dark matter particles must be:

- **Cold** – the evolution of density perturbations in the early universe, and hence the onset of structure formation around the resulting gravitational wells, depends on the free-streaming length of dark matter particles. Although N-body simulations effectively reproduced large-scale structures with non-relativistic dark matter, several discrepancies also emerged, such as the overestimated proportion of subhalos – known as the missing satellites problem [48, 49]. Such features nudge towards alternative models like warm dark matter [50] or self-interacting dark matter [51].

- **Long-lived** – although there is no formal motivation for the absolute stability of dark matter, it appears to persist over cosmological timescales with a lifetime that is comparable to or greater than the age of the universe [52].

- **Non-baryonic** – in combination with precision measurements of the CMB, predictions from Big Bang nucleosynthesis models suggest that baryonic matter comprises only ∼5% of the total energy density of the universe [53]. This is closely tied to the measured abundance of deuterium in particular, which is highly sensitive to the baryon density in the early universe, and necessitates that most of the matter density must be non-baryonic [54].

- **Dissipationless** – dark matter cannot cool by radiating photons, and hence it is intrinsically dark. Moreover, this implies that it is electrically neutral, with constraints on its millicharge informed by CMB fluctuation measurements [55, 56].

- **Collisionless** – interactions between dark matter particles or with ordinary matter must be mediated by gravity, and possibly by the weak force. Upper bounds on the dark matter self-interaction cross section are placed from cluster mergers at $\sigma/m_{\mathrm{DM}} < 0.47\,\mathrm{cm}^2/\mathrm{g}$, with larger values expected to facilitate dissipation and hence result in the disruption of halo sphericity [57, 58].

There is no shortage of hypotheses for what dark matter could be, from exotic particles beyond the Standard Model to modified theories of gravity. It is also worth noting that dark matter does not necessarily consist of exclusively one particle type, and in fact some formulations like mirror dark matter [59] propose the existence of several species. A brief overview of the most popular candidates is given in the following sections, though this is by no means comprehensive and only lightly touches upon other contenders such as supersymmetry and Kaluza-Klein states [60].

1.2.1 Axions

The axion is a pseudo-Nambu-Goldstone boson produced by the Peccei-Quinn mechanism, postulated to explain the absence of expected CP-symmetry violation in the strong interaction [61]. Although the original axion was ruled out [62], this led to a broader definition of axion-like particles, which share properties with the standard axion except without a presumed relationship between the mass and coupling strength [63]. This class of particles presents suitable dark matter candidates for the $1\,\mu\mathrm{eV/c^2} \lesssim m_a \lesssim 10\,\mathrm{meV/c^2}$ mass range, with the lower bound required to reproduce an appropriate relic density, and the upper bound set by observations of stellar cooling [64, 65]. In addition, axions are cold despite their low mass as their production is non-thermal. Axions may be detected by their weak coupling with ordinary matter, through either the inverse Primakoff effect [66], whereby conversion to photons occurs in the presence of a strong magnetic field, or the axioelectric effect [67], which is analogous to the photoelectric effect and results in the ionisation of an atomic electron.

1.2.2 Neutrinos

Standard Model neutrinos were an early candidate for dark matter as they satisfy most of the necessary criteria, with the main exception being that they are ultrarelativistic (hot); primordial perturbations would have been washed out, implying a top-down formation hierarchy in which large structures would emerge first, rather than the bottom-up clustering route described by the ΛCDM model

[68]. Considering the Gerstein-Zeldovich limit $\Omega_\nu h^2 = \sum m_\nu/(94\,\mathrm{eV/c^2})$ for three neutrino flavours [69], along with the latest result from the KATRIN experiment $m_\nu < 0.8\,\mathrm{eV/c^2}$ [70], the upper bound on the total neutrino relic density is roughly $\Omega_\nu h^2 \lesssim 0.026$. Therefore, given the value of $\Omega_c h^2 = (0.120 \pm 0.001)$ measured by the Planck collaboration [35], neutrinos could only account for $\lesssim$21.7% of the total dark matter density, and hence their abundance is not sufficient to constitute a dominant component of dark matter.

A proposed extension is sterile neutrinos – heavier right-handed neutrinos that are weakly coupled to the left-handed Standard Model active neutrinos, and otherwise only interact through gravity [71]. Their production occurs through mixing with active neutrinos, which is non-thermal if the oscillations are slower than the rate of expansion. As such, sterile neutrinos are mainly viable as a warm dark matter candidate for a mass at the keV/c^2 scale [72].

1.2.3 Weakly interacting massive particles

It is assumed that dark and baryonic matter were in thermodynamic equilibrium in the very early universe, with equal rates of production and annihilation. As the temperature dropped with the expansion of the universe, dark matter production became suppressed and annihilation dominated. Consequently, the dark matter density decreased exponentially up until the Hubble expansion rate exceeded the annihilation rate, after which the density approached a constant value – this moment of chemical decoupling is referred to as the freeze-out point [73]. For non-relativistic species, the dark matter relic density is approximately related to the thermally-averaged annihilation cross section by

$$\Omega_c h^2 \approx \frac{3 \times 10^{-27}\,\mathrm{cm^3/s}}{\langle \sigma_A v \rangle}, \tag{1.2}$$

such that a higher annihilation cross section translates into a later freeze-out point and hence a lower density.

Various extensions to the Standard Model predict the existence of heavy and stable particles that interact only through the weak force and gravity, such as neutralinos in the Minimal Supersymmetric Standard Model and the lightest Kaluza-Klein particle in theories of universal extra dimensions; candidates with these characteristics are termed weakly interacting massive particles (WIMPs) [74]. For particles coupled to the weak interaction and possessing a GeV/c^2-scale mass, the annihilation cross section $\langle \sigma_A v \rangle \sim G_F^2 m_\chi^2$ naturally reproduces the correct thermal relic density. This apparent coincidence, commonly known as the 'WIMP miracle', has established WIMPs as the leading dark matter candidate and prompted an expansive experimental programme designed for their detection [75].

1.2.4 Massive astrophysical compact halo objects

It is still expected that some portion of dark matter may exist in the form of non-luminous baryonic matter such as large planets, white dwarfs, and neutron stars, all of which are encompassed within the class of massive astrophysical compact halo objects (MACHOs) [76, 77]. Searches for gravitational microlensing in the Large Magellanic Cloud place the MACHO halo content at approximately 20%, and with a typical mass of around 0.15–0.90 $\mathrm{M}_\odot$ [78]. A distinct sub-category of MACHOs is primordial black holes (PBHs), which are theorised to have formed from the gravitational collapse of overdense regions induced by perturbations in the very early universe [79]. These are both microscopic and macroscopic in nature, spanning a vast range of masses; although PBHs with $m_{\mathrm{PBH}} \lesssim 10^{-18}\,\mathrm{M}_\odot$ are expected to have evaporated due to Hawking radiation, larger ones could continue to grow through accretion or merging with other PBHs [80]. Recent limits primarily relying on gravitational microlensing techniques generally point towards a low fraction of PBHs as dark matter, with $\Omega_{\mathrm{PBH}}/\Omega_c \lesssim 10^{-2}$ [81]. Observations of gravitational waves generated by PBH merger processes could be used to further constrain their abundance [82], as facilitated by large interferometry experiments such as LIGO, Virgo, and the future LISA probe.

1.2.5 Modified gravity

Alterations to theories of gravity offer an alternative to the dark matter hypothesis. The earliest form of this is referred to as modified Newtonian dynamics (MOND), which introduced adjustments to Newton's second law of motion in the regime of very small accelerations [83]. Following this, a relativistic generalisation known as tensor-vector-scalar (TeVeS) gravity was developed to accommodate phenomena such as gravitational lensing, whilst adhering to conservation laws violated by the initial version of MOND [84]. Although these models have been primarily successful in application to galactic rotation curves [85], they struggle to simultaneously reconcile all anomalous observations associated with dark matter [86].

1.3 Searches for dark matter

As depicted in Figure 1.4, three complementary strategies are available to probe for the extensive list of dark matter candidates: missing energy from production in particle colliders, indirect detection through astronomical observations of secondary radiation from pair annihilation, and direct detection of scatters with atomic nuclei in ultra-low background environments. In the following sections, the concepts and status of each approach are briefly outlined, with a focus on direct detection.

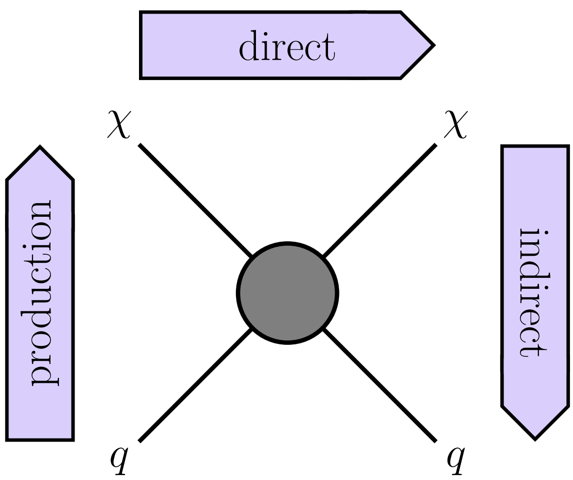

Figure 1.4: A pseudo-Feynman diagram of the interactions that underpin each of the three approaches to dark matter searches. Dark matter and Standard Model particles are represented by χ and q, respectively. This type of diagram is often accompanied by the colloquial phrase 'make it, break it, shake it'.

1.3.1 Dark matter production

In collider experiments, the presence of invisible particles produced in high-energy collisions is inferred from missing transverse momentum ($p_{\mathrm{T}}^{\mathrm{miss}}$). Although invisible particles are expected to predominantly consist of outgoing neutrinos, they could also result from the pair production of dark matter. The real-time selection of such events from a barrage of proton-proton collisions is tricky; whereas model-agnostic triggers broadly preserve events with substantial $p_{\mathrm{T}}^{\mathrm{miss}}$, some assumptions must be made for models that predict a low $p_{\mathrm{T}}^{\mathrm{miss}}$, which can complicate comparability with direct and indirect detection modes [87]. The model dependence of collider searches can be reduced by requiring that Standard Model processes govern the recoil of visible particles, such as through the emission of initial state radiation in the form of hadronic jets [88, 89], Z bosons [90, 91], or Higgs bosons [92, 93]. In addition, exceedingly precise measurements of the Z decay width paired with robust Standard Model predictions are also sensitive to contributions from invisible channels [94–96]. Stringent limits have been set for various model parameter spaces by the ATLAS and CMS experiments at the Large Hadron Collider, though evidence for the production of dark matter at colliders has yet to emerge.

1.3.2 Indirect detection

Indirect searches for dark matter seek to observe the products of its self-annihilation or decay. In particular, the focus is on the detection of anomalous flux originating from regions with an enhanced dark matter concentration, such as spheroidal dwarf galaxies, the galactic core and halo of the Milky Way, and the core of the Sun [97]. Tight constraints have been set on the annihilation cross section of dark matter into neutrinos [98], as well as the flux of high-energy neutrinos, primarily by ANTARES [99, 100], IceCube [101, 102], and Super-Kamiokande [103, 104]. Astrophysical gamma-ray sources have also been studied by several projects, most notably the Fermi Gamma-ray Space Telescope [105], the AMS-02 module on the International Space Station [106], and the terrestrial HESS [107]. This led to the discovery of an excess of $\sim$1–3 GeV gamma rays around the galactic centre [108], initially attributed to possible dark matter annihilation, though the same behaviour has not been seen for other galaxies [109] and hence alternative explanations point to unresolved pulsars [110]. In addition, an excess of positrons has been observed by PAMELA [111] and AMS-02 [112], as well as a higher ratio of antiprotons to protons [113], which are likely due to large uncertainties in the background model [114].

1.3.3 Direct detection

Laboratory-based direct detection experiments aim to observe the exchange of energy between dark matter—primarily WIMPs—and Standard Model particles, in the form of low-energy nuclear recoils. The relevant scattering formalism is discussed here, along with a review of the different detector technologies and the present state of the field.

Velocity distribution

To model the kinematics of WIMP-nucleus scattering, it is necessary to consider the local velocity distribution of incident dark matter particles. As it is not possible to characterise this directly, it is deduced from studies of halo formation in cosmological N-body simulations. The standard halo model is conventionally adopted, which assumes that the Milky Way dark matter halo is an isotropic and isothermal sphere with a density described by the Navarro-Frenk-White profile as $\rho(r) \propto r^{-2}$ [115]. This yields a Maxwell-Boltzmann distribution for the WIMP velocity $\boldsymbol{v}$ in the galactic rest frame [116]:

$$f_g(\boldsymbol{v}) = \begin{cases} \dfrac{N_{\mathrm{SHM}}}{(2\pi\sigma_v^2)^{3/2}} e^{-|\boldsymbol{v}|^2/2\sigma_v^2}, & |\boldsymbol{v}| < v_{\mathrm{esc}} \\ 0, & |\boldsymbol{v}| \geq v_{\mathrm{esc}} \end{cases} \tag{1.3}$$

which is truncated at the escape velocity of the Milky Way $v_{\mathrm{esc}} = 544\,\mathrm{km/s}$ [117]. The normalisation factor N_{SHM} converges to 1 at high values of v_{esc}, and the radial velocity dispersion σ_v is related to the local circular velocity by $\sigma_v = v_0/\sqrt{2}$, where $v_0 = 220\,\mathrm{km/s}$ [118]. Although the standard halo model is a suitable approximation, recent refinements have been made to account for a radially anisotropic population known as the 'Gaia sausage' [119].

For practical purposes, this must be reframed to account for the motion of the Earth around the Sun, which concurrently orbits the galactic centre. This is accomplished with the Galilean transformation $\boldsymbol{v} \to \boldsymbol{v} + \boldsymbol{v}_E(t)$ such that $f(\boldsymbol{v}, t) = f_g(\boldsymbol{v} + \boldsymbol{v}_E(t))$. The Earth's velocity with respect to the galactic centre, $\boldsymbol{v}_E(t)$, is composed of three components: the local standard of rest (LSR) $\boldsymbol{v}_{\mathrm{LSR}}$, the peculiar motion of the Sun relative to the LSR $\boldsymbol{v}_{\odot}^{\mathrm{p}}$, and the orbit of the Earth around the Sun $\boldsymbol{v}_{\mathrm{orb}}(t)$ [120].

Scattering formalism

For elastic scattering between a WIMP and nucleus of respective masses m_χ and m_N, the differential rate is expressed as

$$\frac{dR}{dE_R} = \frac{\rho_0}{m_\chi m_N} \int_{v_{\min}}^{\infty} v f(\boldsymbol{v}, t) \frac{d\sigma_N}{dE_R} d\boldsymbol{v}, \tag{1.4}$$

where $v \equiv |\boldsymbol{v}|$, σ_N is the WIMP-nucleus cross section, and $\rho_0 = 0.3\,\mathrm{GeV/cm^3}$ is the canonical local WIMP density [120]. The lower limit of integration $v_{\min}$ corresponds to the minimum WIMP velocity required to induce a nuclear recoil of energy E_R, given by

$$v_{\min} = \sqrt{\frac{m_N E_R}{2\mu_N^2}}, \tag{1.5}$$

with the reduced mass of the system denoted by $\mu_N = m_\chi m_N/(m_\chi + m_N)$. Since experiments are only sensitive to interactions beyond a specific energy threshold, only part of $f(\boldsymbol{v}, t)$ is ever probed for a given WIMP mass. In combination with the upper limit set by v_{esc}, this imposes a limitation for the detection of lower WIMP masses – the recoil spectrum is restricted to a narrow window between the threshold and a low maximum E_R.

The WIMP-nucleus differential cross section encodes the details of non-relativistc interactions between WIMPs and nuclei. This fundamentally depends on the underlying coupling of WIMPs to quarks, often modelled at specific scales using effective field theories [121]. In practice, the cross section is generally separated into two contributions: spin-independent (SI), which arises from scalar and vector couplings in the effective Lagrangian, and spin-dependent (SD), which originates from axial-vector couplings. The differential cross section is thus defined as follows:

$$\frac{d\sigma_N}{dE_R} = \frac{m_N}{2\mu_N^2 v^2}\left(\sigma_0^{\rm SI} F_{\rm SI}^2(E_R) + \sigma_0^{\rm SD} F_{\rm SD}^2(E_R)\right), \tag{1.6}$$

where $\sigma_0^{\rm SI}$ and $\sigma_0^{\rm SD}$ denote cross sections in the limit of zero momentum transfer. While WIMPs undergo coherent scattering with the entire nucleus for low momentum transfers $q = \sqrt{2m_N E_R}$, nuclear substructure can be resolved at high q due to the shorter de Broglie wavelength, resulting in a loss of coherence and hence a suppressed rate for heavy WIMPs. This momentum dependence is parametrised by the nuclear form factors $F_{\rm SI}^2(E_R)$ and $F_{\rm SD}^2(E_R)$.

The SI WIMP-nucleus cross section is expressed in terms of the mass number A and atomic number Z of the target nucleus as

$$\sigma_0^{\rm SI} = \frac{4\mu_N^2}{\pi}[Zf_p + (A-Z)f_n]^2, \tag{1.7}$$

with f_p and f_n representing the WIMP coupling to protons and neutrons, respectively. It is normally assumed that there is minimal distinction between these couplings, such that $f_p \approx f_n$. Within this approximation, $\sigma_0^{\rm SI}$ is commonly translated into a WIMP-nucleon cross section $\sigma_n^{\rm SI}$ to maintain complementarity between experiments with different target materials:

$$\sigma_0^{\rm SI} = \frac{\mu_N^2}{\mu_n^2} A^2 \sigma_n^{\rm SI}, \tag{1.8}$$

where μ_n is the corresponding WIMP-nucleon reduced mass [122]. The A^2 term presents a coherent enhancement to the cross section, and therefore motivates the utilisation of heavy elements for the detector target. However, it is important to emphasise that this presents a trade-off with respect to the low-energy detection threshold—which scales with m_N—as well as suppression from the nuclear form factor. These effects are evident in Figure 1.5 for several typical target elements, as well as a range of WIMP masses scattering in xenon.

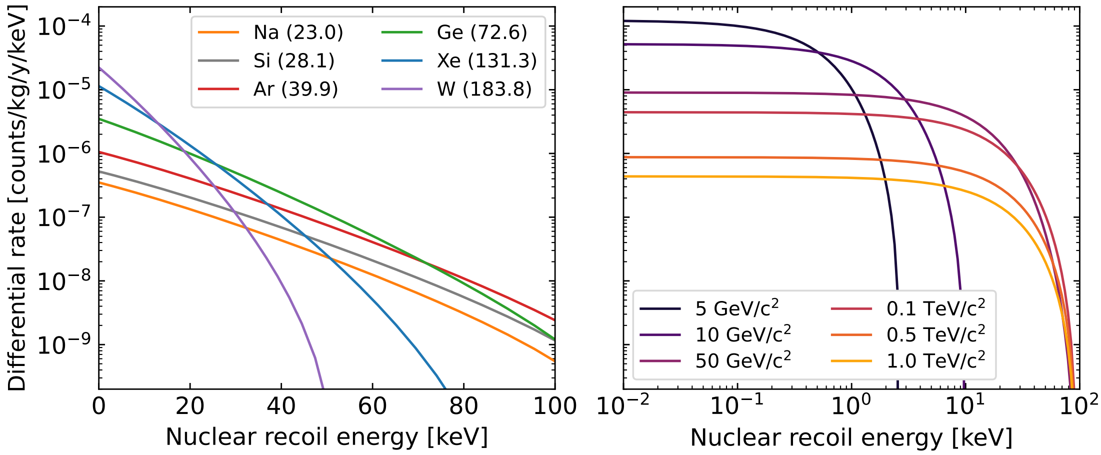

Figure 1.5: The differential rate of SI interactions as a function of the nuclear recoil energy, for a $\sim 40\,\mathrm{GeV/c^2}$ WIMP scattering in various materials (left), as well as for a set of WIMP masses scattering in xenon (right). Rates are conventionally measured in differential rate units (dru), normalised by the detector mass and exposure time. A value of $1\times10^{-46}\,\mathrm{cm}^2$ is assumed for σ_n^{SI} in both plots. Calculations for these curves were performed using the `wimprates` package [123].

For SD interactions, on the other hand, the cross section is given by

$$\sigma_0^{\mathrm{SD}} = \frac{32G_F^2\mu_N^2}{\pi}\frac{(J+1)}{J}[a_p\langle S_p\rangle + a_n\langle S_n\rangle]^2. \tag{1.9}$$

in which a_p and a_n represent coupling constants, $\langle S_p\rangle$ and $\langle S_n\rangle$ describe the spin content of the target nucleus, and J is the total nuclear spin [116]. In this case, the cross section depends on the spin structure of the nucleus rather than its mass number. Consequently, only odd-proton or odd-neutron isotopes provide sensitivity in the SD case due to the cancellation of spin contributions between nucleon pairs. Therefore, the key distinction is that WIMPs couple to the mass of the nucleus in SI interactions, whereas they couple to the net nuclear spin in SD interactions. Although both modes are considered, the SI component dominates for heavy target nuclei [120].

Detector designs

There exists a diverse range of direct detection experiments, typically constructed from radiopure materials to minimise backgrounds, and located deep underground to shield from cosmic rays. In addition to background mitigation, key design drivers to enhance sensitivity generally include maximising the detector mass, and pushing the detection threshold to very low energies [124]. The six main detector technologies, along with some relevant experiments, are summarised below:

- **Inorganic crystal detectors** – scatters in high-purity germanium (CDEX-10 [125]) or silicon (DAMIC-M [126], SENSEI [127]) semiconductor devices produce electron-hole pairs, which are subsequently drifted to electrodes under the influence of an electric field. These operate with an extremely low threshold, though they are limited to kg-scale masses due to quickly growing levels of electronic noise and signal readout times. Alternatively, larger arrays of thallium-doped NaI (ANAIS-112 [128], COSINE-100 [129], DAMA/LIBRA-II [130]) or CsI (KIMS [131]) crystals are used, with scintillation light measured by photomultiplier tubes (PMTs), as illustrated in Figure 1.6 (a). Despite the enhanced sensitivity to SI couplings provided by the elements with high mass numbers, intrinsically elevated background levels and a lack of background discrimination capabilities makes such crystals unsuitable for event-by-event dark matter detection. Instead, they are deployed in long-term searches for annual modulation; as it orbits the Sun, the Earth moves along and against an effective dark matter wind from the direction of the Cygnus constellation, which would manifest as periodic behaviour in the observed rate [132].

- **Cryogenic solid-state detectors** – heat is generated by interactions in dielectric crystals held at mK temperatures, and subsequently measured by a change in the resistivity of transition edge sensors. The temperature change is detected alongside an ionisation signal in high-purity germanium or silicon (CDMSLite [133], SuperCDMS [134], EDELWEISS [135]) as in Figure 1.6 (b), or a scintillation signal in $CaWO_4$ (CRESST [136, 137]). The simultaneous readout of generated heat and either an ionisation or scintillation channel enables background rejection and excellent energy resolution. Moreover, owing to their very low energy thresholds, these devices are mainly sensitive to lighter WIMPs. However, the target mass is restricted by a low specific heat capacity requirement, as well as the limited size of dilution refrigerators, which are necessary to deliver sufficient cooling power.

- **Noble liquid detectors** – scatters in the liquid target generate scintillation light from atomic de-excitation, which is detected by a PMT layout with 4π coverage as depicted in Figure 1.6 (c). The position of the interaction is inferred from the photon arrival times at each PMT, as well as the signal distribution. Single-phase noble element detectors rely heavily on pulse shape discrimination; the singlet and triplet states exhibit different lifetimes, and since their relative population depends on the interaction type and energy, this facilitates background rejection. Although these lifetimes are similar in xenon, as explained in Section 3.2, they advantageously differ by $\mathcal{O}(1)$ µs in the case of argon. Nevertheless, such detectors have utilised both argon (DEAP-3600 [138]) and xenon (XMASS [139]) in experiment.

- **Dual-phase time projection chambers** – in addition to the primary scintillation light collected in single-phase noble detectors, ionised electrons are also extracted into a gaseous phase under strong electric fields, producing a secondary scintillation signal via electroluminescence. As portrayed in Figure 1.6 (d), these detectors are usually cylindrical, with PMT arrays mounted at the top and bottom. Event positions are reconstructed from hit patterns on the top array, along with the time difference between the primary and secondary signals. Furthermore, the relative size of these signals varies with energy and interaction type, and hence provides a powerful means for background rejection. Both argon (DarkSide-50 [140]) and xenon (LUX [141], LUX-ZEPLIN [142], XENONnT [143], PandaX-4T [144]) have been successfully employed, with the latter explored in more detail in Chapter 3. In particular, dual-phase xenon detectors currently dominate in sensitivity to SI interactions for WIMP masses above $\sim 5\,\mathrm{GeV/c^2}$.

- **Bubble chambers** – energy depositions in a superheated liquid target—normally refrigerants such as CF_3I and C_3F_8—induce a local phase transition, resulting in the formation of a bubble as shown in Figure 1.6 (e) (PICASSO [145], PICO [146]). These effectively operate as threshold detectors, with the bubble nucleation energy threshold tuned by making adjustments to the pressure and temperature. Three-dimensional position reconstruction is achieved by means of cameras in a stereoscopic arrangement. One major advantage of bubble chambers is that they are versatile; the liquid target can be exchanged with other compositions often containing the isotope ^{19}F, which is highly sensitive to SD WIMP-proton couplings.

- **Wire chambers** – ionisation tracks are produced by particles traversing a low-pressure gaseous target. Charge is drifted under a static electric field and subsequently collected by multi-wire proportional chamber planes, as visualised in Figure 1.6 (f). Discrimination of signals from backgrounds is based on the ionisation density and length of the observed tracks. A CF_4 target is most commonly used, though it is also often mixed with other gases such as CS_2 (DRIFT-II [147]) to maintain sensitivity to both SD and SI interactions. As opposed to the point-like deposits in solid and liquid targets, the directional information from track reconstruction provides an additional layer of background rejection; analyses may assert that the directionality of a candidate event should be consistent with that of the dark matter wind at a given time. Such a feature is especially important for the reduction of backgrounds from nearly indistinguishable neutrino scatters [116, 148].

The above list is not fully comprehensive – more specialised detector technologies exist, including searches for axions using a resonant microwave cavity within a superconducting magnet (ADMX [149]), and a copper spherical proportional counter that can be filled with different gas compositions (NEWS-G [150]). Other promising technologies have also been proposed, such as using superfluid helium as a detector medium [151], as well as augmentations to existing experiments, namely H_2 doping [152] or crystallisation in dual phase xenon detectors [153].

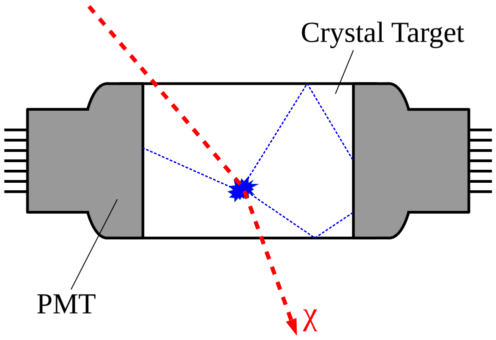

(a) Inorganic crystal detectors

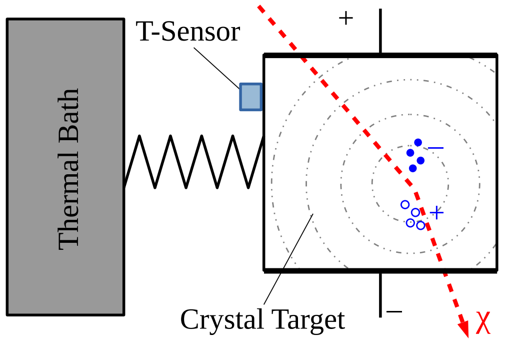

(b) Cryogenic solid-state detectors

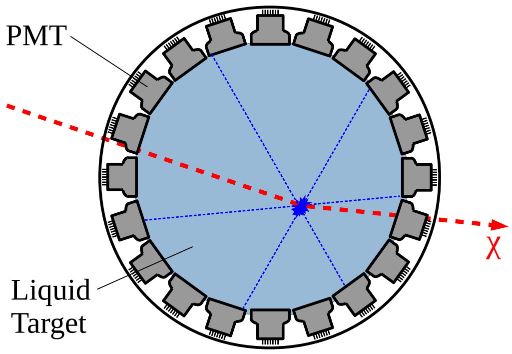

(c) Noble liquid detectors

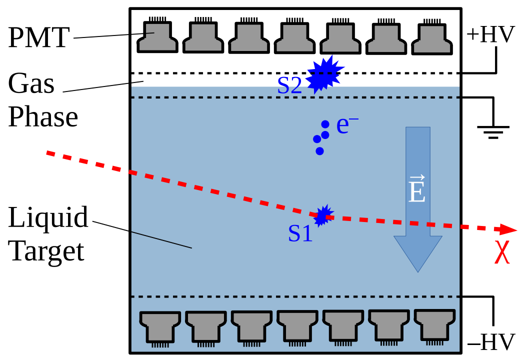

(d) Dual-phase time projection chambers

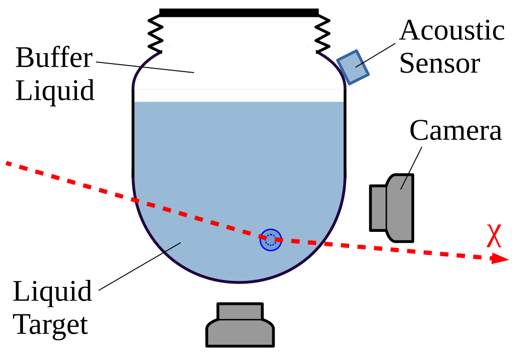

(e) Bubble chambers

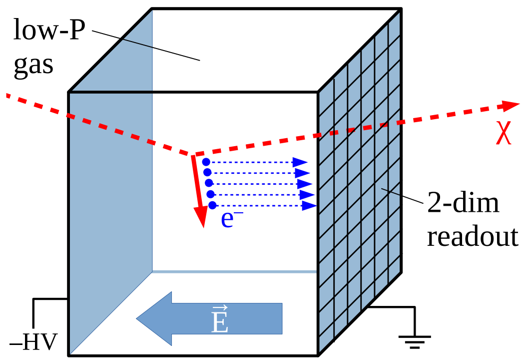

(f) Wire chambers

Figure 1.6: Diagrams of six different designs and technologies deployed in dark matter direct detection experiments. In each instance, the scatter of a dark matter particle χ is indicated by a dashed red arrow. All graphics obtained from [124].

Current status

The direct detection of dark matter is a relatively young field, and has undergone rapid development since first attempts began in the late 1980s [154]. At present, the LUX-ZEPLIN experiment has set the most stringent limits, excluding SI WIMP-nucleon cross sections above $9.2 \times 10^{-48}\,\mathrm{cm}^2$ for $36\,\mathrm{GeV/c}^2$ WIMPs at the 90% confidence level [142]. This is presented along with the other current exclusion limits in Figure 1.7.

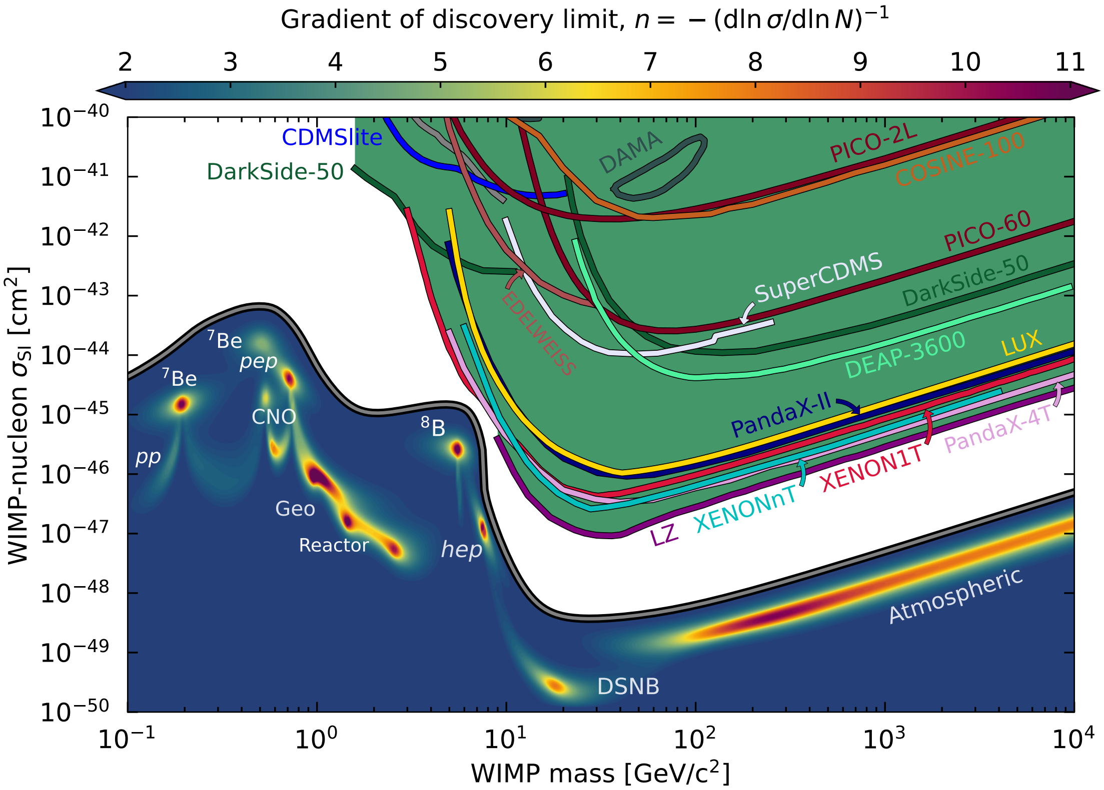

Figure 1.7: Current exclusion limits for the spin-independent WIMP-nucleon cross section as a function of WIMP mass, along with the neutrino fog for xenon targets. The difficulty of claiming an observation within the neutrino fog is quantified by the gradient of discovery limit, whereby $n = 2$ represents a resemblance to the original neutrino floor as a departure from Poissonian background subtraction. This plot was reproduced and updated from [155].

Ongoing experiments are on track to reach an irreducible background posed by coherent neutrino-nucleus scattering, which closely mimics expected WIMP signals. Traditionally, this stage is considered a hard boundary and referred to as the 'neutrino floor', defined by the interpolation of arbitrary choices of experimental exposures and thresholds [156]. More recently, the interpretation of this boundary has shifted towards a softer ‘neutrino fog’, in which such backgrounds become distinguishable in the limit of high statistics, owing to the inexact matching of WIMP and neutrino spectral features [155]. The extent of this statistics requirement is quantified by a more consistent definition for the neutrino fog, using the gradient of the discovery limit n as a metric analogous to the difficulty of claiming an observation; a higher n is associated with a greater requisite number of events N, and vice versa. The impact of the neutrino background may also be alleviated by improvements to neutrino flux uncertainties and directional detection techniques.

The search for dark matter remains one of the main science drivers on the cosmic frontier. A thorough strategy has been developed by the wider community as part of the 2021 Snowmass process, which outlines many promising prospects on the horizon [157]. In the context of xenon-based detectors, comprehensive research and development has already started for the planning and design of a much larger next-generation detector as part of the XLZD consortium between XENON, LUX-ZEPLIN, and DARWIN [158].

2 Rare nuclear decays

The field of neutrino physics has grown significantly over the past century, owing to a worldwide collaborative effort. Despite this, several important questions regarding the properties of neutrinos remain open, some of which have implications for dark matter searches. Proposed answers mainly hint towards new physics beyond the Standard Model, which can be probed through searches for extremely rare nuclear decays. This chapter covers the key concepts for such interactions and how they are tied to the fundamental nature of neutrinos, along with experimental approaches for their detection.

2.1 Massive neutrinos

The observed phenomenon of neutrino oscillations, whereby the lepton flavour of a propagating neutrino can transition over large distances, has established that neutrinos possess mass [159]. The underlying formalism assumes the decomposition of three neutrino flavour eigenstates $|\nu_\alpha\rangle$ into a linear superposition of three mass eigenstates $|\nu_k\rangle$ as

$$|\nu_\alpha\rangle = \sum_{k=1}^{3} U_{\alpha k}|\nu_k\rangle \tag{2.1}$$

where α denotes one of three lepton flavours (e, μ, τ), and U represents the Pontecorvo-Maki-Nakagawa-Sakata (PMNS) unitary transformation matrix, which is parametrised by three mixing angles (θ_{12}, θ_{13}, θ_{23}) and a single complex phase δ_{CP}. The mass eigenstates evolve with time t as plane waves of the form

$$|\nu_k(t)\rangle = e^{-i(E_k t - \mathbf{p}_k \cdot \mathbf{x})}|\nu_k\rangle, \tag{2.2}$$

for a given energy $E_k = \sqrt{m_k^2 + |\mathbf{p}_k|^2}$ and momentum $\mathbf{p}_k$, over a distance $\mathbf{x}$. The resulting flavour transition probability $P(\alpha \to \beta) = |\langle \nu_\beta | \nu_\alpha(t) \rangle|^2$ depends on the differences between the squared masses $\Delta m_{kj}^2 = \left(m_k^2 - m_j^2\right)$, and the occurrence of neutrino flavour oscillations therefore implies the existence of non-degenerate masses for the mass eigenstates.

This description successfully explains observations made in a variety of dedicated experiments, with which the neutrino oscillation parameters have been precisely measured and constrained [160]. Nonetheless, a number of questions pertaining to the neutrino mass are left unanswered. For one, the relative ordering of the neutrino masses is ambiguous, with two potential scenarios: a 'normal hierarchy' ($m_1 < m_2 < m_3$) in analogy with that of charged leptons, and an 'inverted hierarchy' ($m_3 < m_1 < m_2$). Moreover, flavour oscillation measurements are only sensitive to Δm_{kj}^2 and hence they do not provide constraints for the overall neutrino mass scale. As mentioned in Section 1.2.2, upper limits on the absolute neutrino mass are obtained through other means instead; at $m_\nu < 0.8\,\mathrm{eV/c^2}$ from studies of the endpoint of the tritium beta decay spectrum in the KATRIN experiment [70], and with $\sum m_\nu < 0.12\,\mathrm{eV/c^2}$ from cosmological measurements [35]. The absolute neutrino mass scale may also be directly accessible from searches for neutrinoless double beta decays, introduced in the following section.

Whilst the masses of neutrinos are not known, it is evident that they must be considerably smaller than those of other fermions – by at least a factor of 10^6 with respect to the electron mass, for instance. This poses a peculiar situation if the neutrino masses are associated with the Higgs mechanism, and hence suggests that a different mechanism could be at play. The most straightforward way to accommodate massive neutrinos within the Standard Model Lagrangian is through the addition of a Dirac mass term, which includes right-handed neutrinos and left-handed antineutrinos that do not participate in the weak interaction. It is also possible to introduce a Majorana mass term without breaking local gauge invariance, which takes advantage of the fact that neutral fermion fields are invariant under charge conjugation – this is known as the Majorana condition [161]. A striking consequence of this is that there is a direct coupling between particles and antiparticles, and that Majorana neutrinos would therefore be their own antiparticles. Furthermore, a general and renormalisable extension to the Lagrangian containing both Dirac and Majorana mass terms gives rise to a light neutrino state ν and a heavy neutrino state N, with masses

$$|m_\nu| \approx \frac{m_D^2}{m_M} \quad \text{and} \quad m_N \approx m_M, \tag{2.3}$$

where the Majorana mass m_M is assumed to be much greater than the Dirac mass m_D. This hypothesis for the manner in which neutrino masses are generated is referred to as the 'seesaw mechanism', due to the imbalance between m_ν and m_N. In particular, the seesaw mechanism predicts that there exists a very light neutrino as well as a very heavy neutrino for each of the three neutrino generations, with a very large Majorana mass of $m_M \gtrsim 10^{10}\,\mathrm{GeV/c^2}$ necessary to reproduce $m_\nu \lesssim 0.1\,\mathrm{eV/c^2}$, given a typical fermion mass of $\mathcal{O}(1)$ GeV for m_D [162, 163].

An additional feature of the seesaw mechanism is that it facilitates processes that would have contributed to the observed matter-antimatter asymmetry of the universe. In general, this asymmetry must arise from the fulfilment of Sakharov's conditions for baryogenesis: baryon number violation, C-symmetry and CP-symmetry violation, and interactions out of thermal equilibrium [164]. If neutrinos are Majorana particles, then interactions that violate lepton number conservation are possible. Moreover, it has been postulated that leptonic asymmetries originating from the decays of heavy Majorana neutrinos could produce baryogenesis through sphaleron processes – a mechanism known as leptogenesis [165].

2.2 Second-order weak decays

In 1935, it was proposed by Goeppert-Mayer that certain isotopes could undergo two beta decays simultaneously through the process of two-neutrino double beta ($2\nu\beta\beta$) decay, as per

$$(A, Z) \longrightarrow (A, Z+2) + 2e^- + 2\bar{\nu}_e \qquad (2\nu\beta\beta), \tag{2.4}$$

where the two antineutrinos escape and a detectable signal is formed by the two electrons [166]. Such a process can only occur for nuclei with both even A and even Z, in cases where a single beta decay is energetically forbidden or highly suppressed. As illustrated in Figure 2.1, even-even $(A, Z-2)$ nuclei exhibit a lower nuclear binding energy than neighbouring odd-odd nuclei along the $(A, Z-1)$ isobar, promoting $2\nu\beta\beta$ as the more viable decay route. This is a consequence of the positive pairing term in the liquid-drop model, in which nuclei with an even number of nucleons are more stable due to spin coupling [167].

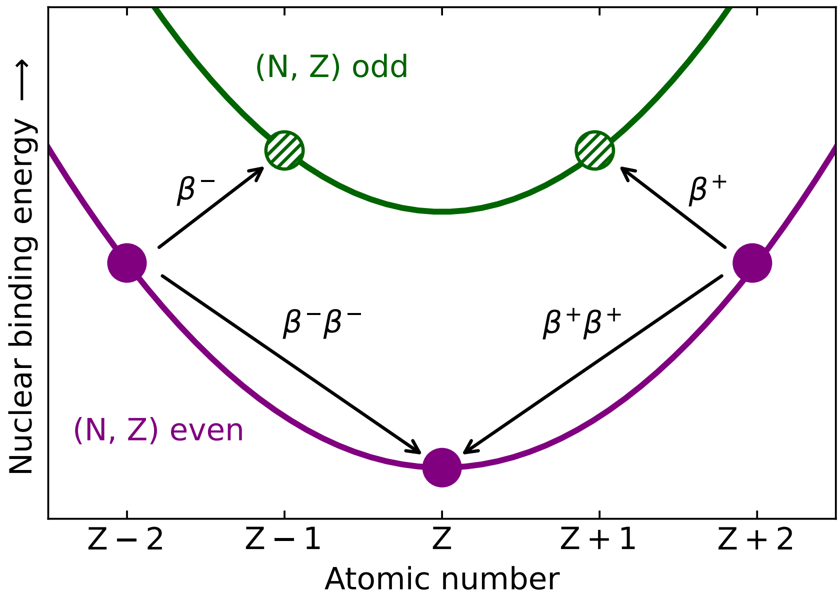

Figure 2.1: Diagram of nuclear binding energies and possible decay modes for even-A nuclei. The binding energy is defined as the deficit between the nuclear mass and the sum of the constituent nucleon masses. Forbidden transitions are represented by hatched markers, and the symbol N is used to denote the neutron number for a given isotope. For odd-even nuclei, ordinary beta decays are dominant and $2\nu\beta\beta$ is highly suppressed. This diagram is based on a figure from [168].

2.2.1 Two-neutrino double electron capture

Since $2\nu\beta\beta$ is a second-order weak decay, it is tremendously rare and has a typical half-life of $> 10^{18}$ years [169], hence it was only first observed directly within a laboratory setting in 1987, for ^{82}Se [170]. This is also the case for a similar set of second-order processes, namely two-neutrino double electron capture (2ν2EC), two-neutrino electron capture with coincident positron emission (2νECβ^+), and two-neutrino double positron emission ($2\nu\beta^+\beta^+$), given by the reactions

$$2e^- + (A,Z) \longrightarrow (A,Z-2) + 2\nu_e \qquad (2\nu2\text{EC}), \tag{2.5}$$

$$e^- + (A,Z) \longrightarrow (A,Z-2) + 2\nu_e + e^+ \qquad (2\nu\text{EC}\beta^+), \tag{2.6}$$

$$(A,Z) \longrightarrow (A,Z-2) + 2\nu_e + 2e^+ \qquad (2\nu\beta^+\beta^+), \tag{2.7}$$

where each of the above modes is progressively rarer due to decreases in the Q-value associated with the requirements for positron emission. The 2ν2EC decay mode is thus the most probable of the three; its half-life measurement for ^{124}Xe is the subject of Chapter 5. The other two modes may be discovered in the near future, as their experimental signature is enhanced by unique topologies produced by annihilation from the outgoing positrons.

For a given isotope, the 2ν2EC half-life is calculated as

$$\left(T_{1/2}^{2\nu2\text{EC}}\right)^{-1} = G_{2\nu}^{2\text{EC}} g_A^4 \left|m_e c^2 M^{(2\nu)}\right|^2, \tag{2.8}$$

where g_A is the weak axial-vector coupling strength, m_e is the electron mass, $M^{(2\nu)}$ is the nuclear matrix element (NME) common between the three modes, and the phase space factor $G_{2\nu}^{2\text{EC}}$ is proportional to the Q-value taken to the fifth power [171]. Comparisons between theoretical predictions of NMEs and those obtained from experimental measurements are used to validate nuclear models, which can subsequently contribute towards improved calculations for NMEs of undiscovered decays. Input from 2ν2EC is particularly valuable as it informs the proton-rich side of the binding energy parabola for even-even isobars.

2.2.2 Neutrinoless decays

Soon after the theory of Majorana fermions was first developed, it was proposed that double beta decays could occur without the emission of neutrinos if they are Majorana particles [172] – a process referred to as neutrinoless double beta ($0\nu\beta\beta$) decay. The simplest mechanism for this is through the exchange of a virtual light neutrino as visualised in Figure 2.2 (a), which requires that neutrinos are their own antiparticles [173]. In addition to confirming that the neutrino mass is generated by the seesaw mechanism, and hence that neutrinos are Majorana particles, the discovery of $0\nu\beta\beta$ decay would also provide evidence for lepton number violation ($\Delta L = 2$). Searches for neutrinoless decays are therefore strongly motivated as a potential source of new physics.

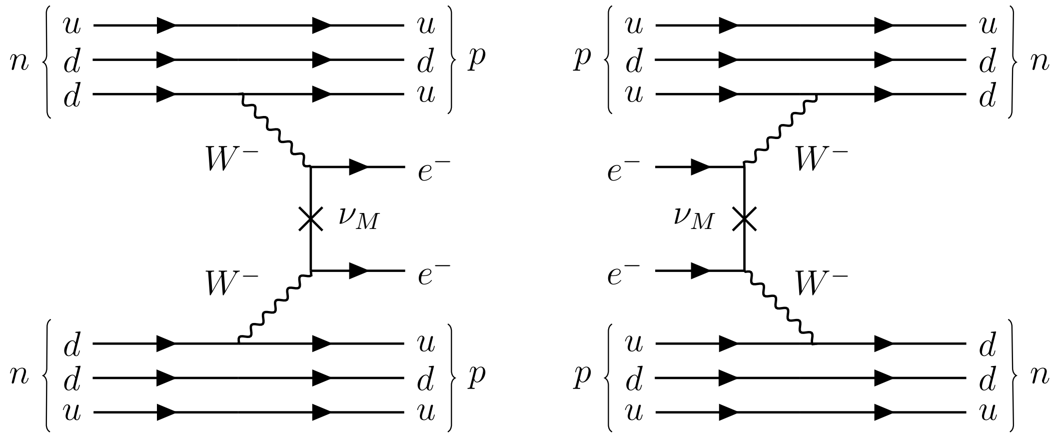

(a) $0\nu\beta\beta$ (b) $0\nu 2\mathrm{EC}$

Figure 2.2: First-order Feynman diagrams for neutrinoless double beta decay (a) and neutrinoless double electron capture (b), both mediated by the exchange of a virtual light Majorana neutrino ν_M. The cross indicates the equivalence of neutrinos and antineutrinos along with an inherent chirality flip.

The half-life of a $0\nu\beta\beta$ process is expressed as

$$\left(T_{1/2}^{0\nu\beta\beta}\right)^{-1} = G_{0\nu}^{\beta\beta} \left|M^{(0\nu)}\right|^2 \langle m_{\beta\beta}\rangle^2, \tag{2.9}$$

where $G_{0\nu}^{\beta\beta}$ and $M^{(0\nu)}$ respectively denote the phase space factor and NME, akin to Equation 2.8. More importantly, the half-life is sensitive to the neutrino mass scale, the mass hierarchy, and oscillation parameters, through the effective Majorana mass term $\langle m_{\beta\beta} \rangle$, given by

$$\langle m_{\beta\beta} \rangle = \sum_{k=1}^{3} |U_{ek}|^2 \, m_k, \tag{2.10}$$

with U_{ek} representing the first row of the PMNS matrix, where two additional complex Majorana phases are also involved [174]. The relationship between $\langle m_{\beta\beta} \rangle$ and the lightest neutrino mass m_ℓ is visualised in Figure 2.3 for the two possible hierarchies, along with some experimental limits. The dependence on the mass hierarchy is evident; an inverted mass hierarchy results in higher $0\nu\beta\beta$ rates than a normal hierarchy, which produces a relative difference of approximately one order of magnitude in $\langle m_{\beta\beta} \rangle$. Moreover, there is a 2–5 meV interval in m_ℓ where $\langle m_{\beta\beta} \rangle$ vanishes for the normal mass hierarchy. The overlap in the $m_\ell > 0.1\,\text{eV}$ region corresponds to the quasi-degenerate regime, in which the neutrino masses would be approximately equal [175].

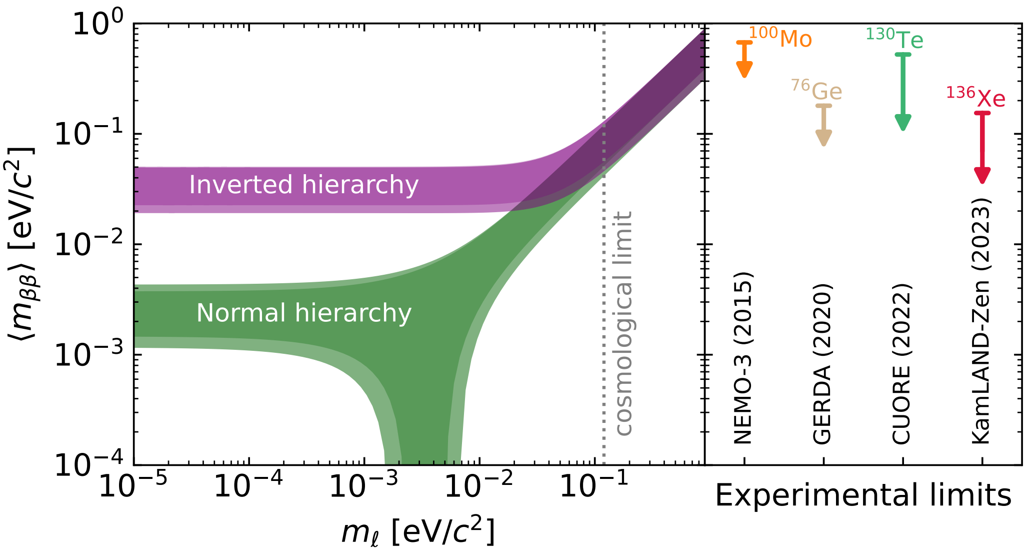

Figure 2.3: Distribution of the effective Majorana neutrino mass $\langle m_{\beta\beta} \rangle$ as a function of the lightest neutrino mass m_ℓ for both mass hierarchy scenarios. Neutrino oscillation parameters were referenced from a global fit [160], and uniformly-distributed Majorana phases were assumed. Shaded regions outline both the best-fit parameters as well as $\pm 3\sigma$ intervals for the mixing parameters. A dotted line is used to indicate the upper limit on the sum of the three neutrino masses obtained from cosmological constraints. Experimental limits for four different target materials are also included [176–179]. Code for creating this plot was based on [180].

It is worth emphasising that there exist other $0\nu\beta\beta$ mechanisms aside from light Majorana neutrino exchange, such as heavy neutrino exchange, or left-right symmetric theories that are independent of mixing parameters [181]. In order to translate $0\nu\beta\beta$ decay measurements into a neutrino mass, the underlying mechanism must also be understood. The wide range of compatible $\langle m_{\beta\beta} \rangle$ values for a given measurement are also an indication of the large theoretical uncertainties associated with the NME calculations.

Neutrinoless modes have also been hypothesised for the set of similar second-order processes described in Equations 2.5–2.7, with the Feynman diagram for neutrinoless double electron capture (0ν2EC) shown in Figure 2.2 (b), for example. As such decays pertain to proton-rich isotopes, they provide complementary information to $0\nu\beta\beta$ decay on the neutron-rich side of the binding energy parabola. This is especially valuable as it offers an alternative approach for probing the underlying mechanism responsible for the neutrino mass, as well as to verify methods for obtaining NMEs [182].

2.3 Experimental strategies

For $2\nu\beta\beta$ decay, the energy deposited by the outgoing electrons produces a continuous beta spectrum due to loss of momentum to the escaping neutrinos, with an endpoint at the Q-value ($Q_{\beta\beta}$). In contrast to this, the $0\nu\beta\beta$ experimental signature manifests as a monoenergetic peak at $Q_{\beta\beta}$, as all of the energy is transferred to the electrons.

Although $0\nu\beta\beta$ decay has yet to be discovered, stringent experimental limits have been set on the half-life for a range of isotopes. In general, for a target mass of M_T and an exposure time t, the observation of N_s candidate signal events within a background-free experiment corresponds to a half-life of

$$T_{1/2}^{0\nu\beta\beta} = \left(\frac{\eta N_A M_T}{M_A}\right) \frac{t\epsilon}{N_s} \ln 2, \tag{2.11}$$

where N_A is Avogadro's constant, η is the isotopic abundance of the parent isotope, M_A is the molar mass, and ϵ is the signal detection efficiency [181]. The term in the brackets encompasses the number of target atoms for the isotope of interest. In reality, the signal is often obscured by a Poissonian background of N_b events, such that $N_s \geq \sqrt{N_b}$ events would be required to overcome a 1σ upward fluctuation of the background [175]. For a background rate of R_b over an energy region of interest (ROI) ΔE, the estimated number of background events is approximately $N_b = R_b M_T \Delta E t$, where R_b is quantified in differential rate units. This results in a lower limit for the half-life given by

$$T_{1/2}^{0\nu\beta\beta} \geq \frac{\epsilon\eta N_A}{M_A}\sqrt{\frac{M_T t}{R_b \Delta E}} \ln 2. \tag{2.12}$$

The above expression highlights several key factors that influence detector design choices for $0\nu\beta\beta$-decay searches, most of which are also broadly applicable to other rare event searches. The most straightforward way to maximise sensitivity is to increase the exposure through a combination of longer run times and a larger target mass. The choice of isotope heavily influences this; from the small selection of isotopes to study, the ease of procurement highly impacts the scalability of M_T. Moreover, the sensitivity strongly depends on the isotopic abundance, which may be enhanced with enrichment. In addition, a high detection efficiency for the two-electron signal is crucial, which can be accomplished through sophisticated background rejection techniques, such as exploiting single-track information from precise position reconstruction. The sensitivity can also be improved through reductions to the background rate, which can be achieved by utilising radiopure materials for construction of the detector and shielding it from cosmic rays by operating underground. Furthermore, optimisation of the energy resolution allows for the definition of a narrower search window ΔE, as well as for better discrimination from gamma-ray peaks within proximity of the signal.

In practice, it is not possible to optimise all of these aspects, and experiments thus focus on a subset of parameters instead. As the ultimate goal is to detect rare events, there are many parallels between searches for $0\nu\beta\beta$ decay and the direct detection of dark matter. In particular, detector designs share several elements and fall under some of the categories described in Section 1.3.3. The status of relevant $0\nu\beta\beta$ decay searches is summarised by the list of past and present results in Table 2.1. An overview of the specific detector technologies, as well as projected sensitivities of upcoming experiments, can be found in recent reviews [181, 183].

Table 2.1: List of $0\nu\beta\beta$ decay experiments with reported 90% confidence level lower limits on the half-life, for a range of different isotopes. A variety of detector technologies are employed: organic scintillators (OSs), inorganic scintillators (ISs), semiconductor devices (SDs), cryogenic calorimeters (CCs), tracking calorimeters (TCs), and time projection chambers (TPCs). Q-values quoted from QCalc [184].

Isotope	$Q_{\beta\beta}$ [MeV]	Experiment	Detector	$T_{1/2}^{0\nu\beta\beta}$ [y]	Ref.
^{48}Ca	4.268	CANDLES-III	IS	$> 0.8 \times 10^{22}$	[185]
		ELEGANT-VI	IS	$> 5.8 \times 10^{22}$	[186]
		NEMO-3	TC	$> 2.0 \times 10^{22}$	[187]
^{76}Ge	2.039	GERDA	SD	$> 1.8 \times 10^{26}$	[177]
		Majorana D.	SD	$> 8.3 \times 10^{25}$	[188]
^{82}Se	2.998	CUPID-0	CC	$> 3.5 \times 10^{24}$	[189]
		NEMO-3	TC	$> 2.5 \times 10^{23}$	[190]
^{96}Zr	3.356	NEMO-3	TC	$> 9.2 \times 10^{21}$	[191]
^{100}Mo	3.034	CUPID-Mo	CC	$> 1.8 \times 10^{24}$	[192]
		NEMO-3	TC	$> 1.1 \times 10^{24}$	[176]
^{116}Cd	2.813	NEMO-3	TC	$> 1.0 \times 10^{23}$	[193]
^{130}Te	2.528	CUORE	CC	$> 2.2 \times 10^{25}$	[178]
^{136}Xe	2.458	EXO-200	TPC	$> 3.5 \times 10^{25}$	[194]
		KamLAND-Zen	OS	$> 2.3 \times 10^{26}$	[179]
		NEXT-White	TPC	$> 1.3 \times 10^{24}$	[195]
^{150}Nd	3.371	NEMO-3	TC	$> 2.0 \times 10^{22}$	[196]

With tonne-scale active masses, future experiments such as LEGEND-1000 [197] are expected to reach a sensitivity of $\gtrsim 10^{28}$ years, and to probe the mass hierarchy more effectively at $\langle m_{\beta\beta} \rangle \lesssim 10^{-2}\,\mathrm{eV/c^2}$. As explored in the following chapters, dark matter experiments are also equipped with sufficient sensitivity to make competitive measurements of the rare processes outlined here.

3 The LUX-ZEPLIN experiment

LUX-ZEPLIN (LZ) is a dark matter direct detection experiment, with a world-leading sensitivity to GeV/c^2-scale WIMPs and a broad physics reach ranging from light dark matter candidates to $0\nu\beta\beta$ decay. In this chapter, the ability of LZ to achieve a diverse science program is described with an overview of the operational principles and detector subsystems, along with a discussion of xenon as a detector medium, and a summary of the main backgrounds, calibration sources, and analysis techniques.

3.1 The LUX-ZEPLIN detector

The LZ detector is situated 1478.3 m (4850 ft) underground within the Davis Cavern, where its predecessor LUX was operated between 2012 and 2016, at the Sanford Underground Research Facility (SURF) in South Dakota, USA. As depicted by the cutaway drawing in Figure 3.1, the detector is shielded in 238 tonnes of ultra-pure water, and is comprised of several subsystems, each of which is detailed in the following sections.

3.1.1 The time projection chamber

At the core of the LZ detector is a dual-phase xenon time projection chamber (TPC), nested within two ultra-radiopure titanium cryostats [198]. The inner cryostat vessel (ICV) holds 10 tonnes of liquid xenon (LXe), and is vacuum insulated

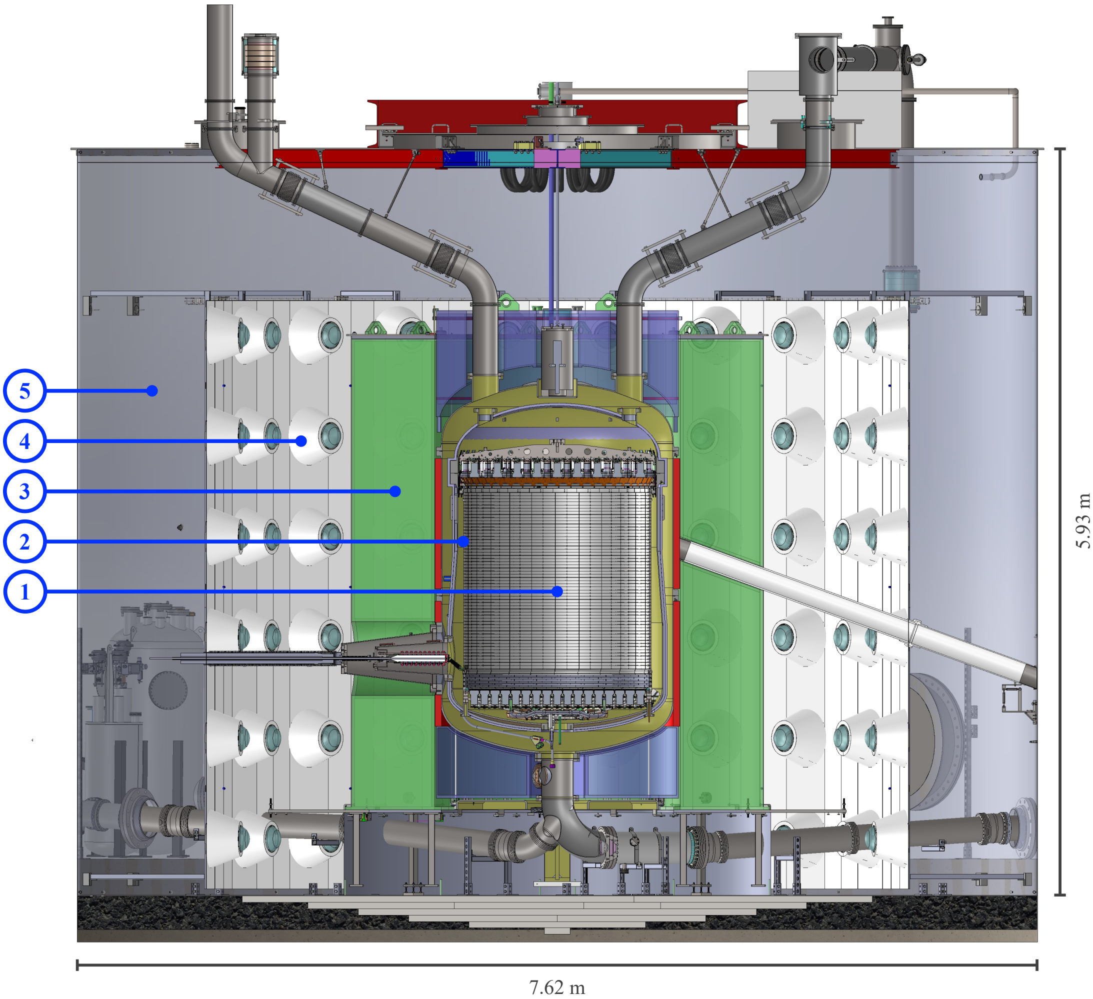

Figure 3.1: A cross-section view of the LZ detector. Working outwards from the centre, the diagram visualises the time projection chamber (1) and liquid xenon skin (2) enclosed within two titanium cryostat vessels, surrounded by the outer detector system acrylic tanks (3) and PMT ladders (4), all submerged in the water tank (5). Various cable feedthroughs and conduits are also rendered.

within the outer cryostat vessel (OCV). The TPC is a cylinder with a diameter of 145.6 cm, containing approximately 7.7 tonnes of LXe. A set of four electrode grids is used to establish vertical electric fields within the TPC, with each grid constructed as a fine mesh woven from stainless steel wires [199]. These divide the TPC into three field regions, as visualised in Figure 3.2: the extraction field region, drift field region, and reverse field region (RFR). The extraction field is generated between the anode grid, which is located in the thin gaseous xenon (GXe) phase at the top, and the gate grid, which sits 5 mm below the liquid level. The gate and cathode grids are set 145.6 cm apart, thus defining a 7-tonne equilateral cylinder as the active LXe volume. The TPC walls consist of polytetrafluoroethylene (PTFE) layers, which exhibit a reflectivity of $> 97\%$ for xenon scintillation light and hence maximise the light collection efficiency [200]. To maintain uniform electric fields towards the walls, the layers are embedded with titanium field-shaping rings connected by a ladder of resistors [201].

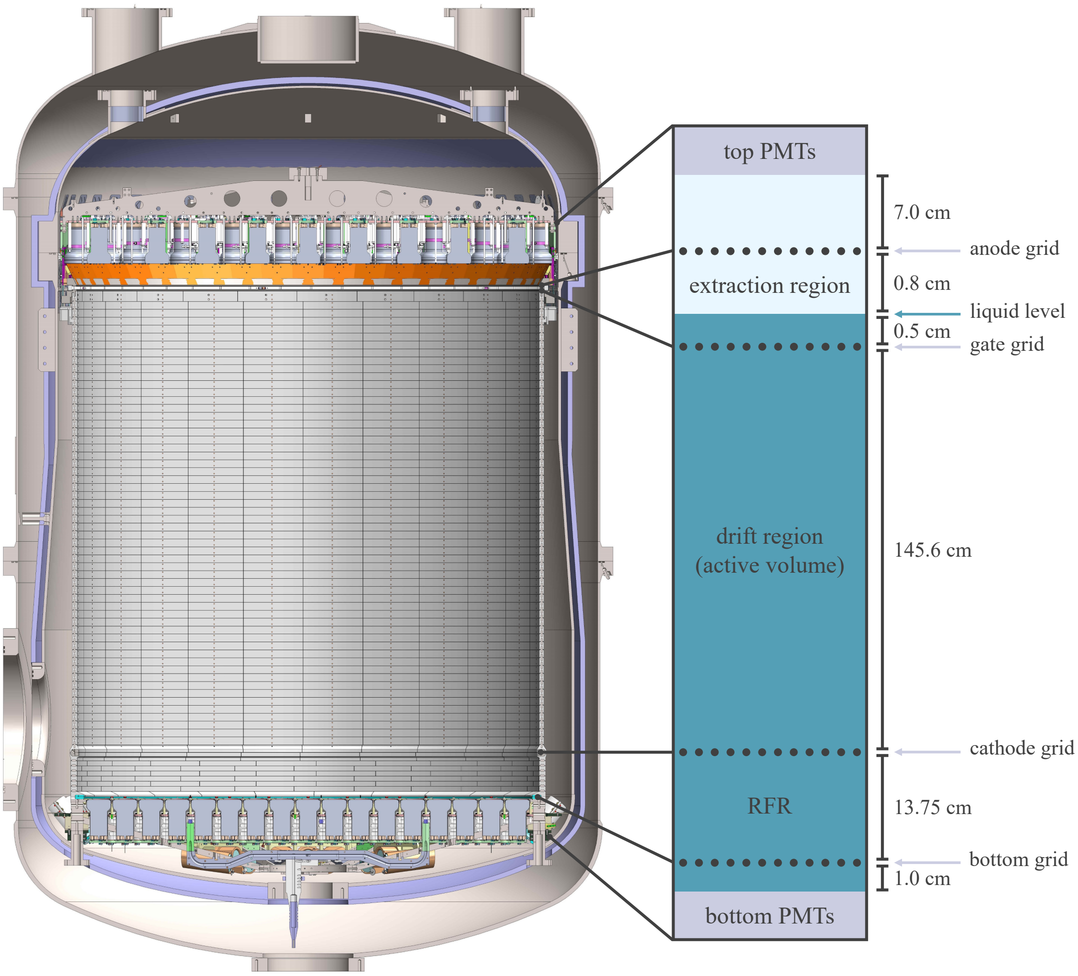

Figure 3.2: A schematic of the TPC nested inside the ICV and OCV, with a diagram of the relative heights between the grids and the liquid surface level. The bottom grid was implemented to protect the bottom array PMTs from the strong fields above, which results in the RFR below the cathode grid. This diagram is based on a figure from [199].

Interactions in the LXe generate a primary scintillation signal (S1) and ionisation electrons. The electrons travel upwards under the influence of the drift field, where they are pulled into the GXe by the stronger extraction field and produce a secondary scintillation signal (S2) via electroluminescence. The underlying mechanisms of these processes are discussed in Section 3.2. Light in the TPC is detected by two arrays of 3-inch Hamamatsu R11410-22 PMTs, with 253 at the top and 241 at the bottom [202, 203]. For position reconstruction, the (x, y) coordinates of an event are inferred from the S2 hit pattern on the top array, whereas the depth (z) is indicated by the time separation between the S1 and S2.

The TPC is also instrumented with various specialised sensors to enable continuous and precise monitoring of the detector during commissioning and operation. Position sensors mounted on and around the top array measure displacements from the thermal expansion or contraction of the TPC. Level sensors near the extraction region track the liquid surface level and assist with the alignment of the TPC. Numerous thermometers attached to the ICV and the PMT arrays are used to record their thermal properties. Loop antennae installed on the PMT trusses detect instabilities in the electrostatic environment such as sparking [204].

3.1.2 Veto detectors

To enhance background rejection, the experiment is equipped with two veto detectors. These serve as anti-coincidence systems that flag multi-site interactions beyond the TPC, which would be uncharacteristic of rare WIMP events.

The innermost veto consists of a thin, optically-isolated LXe skin between the TPC and ICV. The skin contains roughly 2 tonnes of LXe, with a thickness of 4 cm at the top that gradually widens to 8 cm at the bottom to provide a high voltage stand-off distance [201]. With only a liquid phase and a tight geometry, the skin veto is much less sensitive than the TPC as it can only detect primary scintillation and exhibits a reduced light collection efficiency. However, this information is sufficient to tag scatters from gamma rays, as well as deposits made by neutrons. Light in the side skin region is viewed by 93 1-inch Hamamatsu R8520-406 PMTs from above and by 20 2-inch Hamamatsu R8778 from below, spread around the circumference of the TPC. In addition, 18 2-inch R8778 PMTs are mounted in the dome region below the bottom TPC PMT array.

The outer detector (OD) is comprised of a near-hermetic enclosure of 10 acrylic tanks surrounding the OCV, which are filled with 17.3 tonnes of gadolinium-doped liquid scintillator. The primary role of the OD is to tag neutrons, which capture on gadolinium after thermalising, subsequently releasing a gamma-ray cascade with a total energy of 7.9–8.5 MeV. Alternatively, captures on hydrogen in the liquid scintillator and acrylic tank walls can occur 5–10% of the time, and generate a single 2.2 MeV gamma ray. The timing of these bursts is predominantly within a 500 µs window of the S1, enabling a neutron tagging efficiency of $> 95\%$ [205]. Scintillation light in the OD is observed by 120 8-inch Hamamatsu R5912 PMTs arranged on 20 ladders encircling the detector, submerged in the water tank. All exposed surfaces are covered with highly reflective sheets of Tyvek to improve the light collection efficiency.

3.1.3 Xenon circulation system

The outgassing of detector materials can introduce impurities into the xenon bulk. These include krypton and radon, which contribute backgrounds to LZ, as well as electronegative elements such as oxygen and nitrogen, which can subsequently impact the charge collection efficiency of the TPC. To maintain a high level of purity, the 10-tonne xenon inventory is continuously circulated through an online purification system using a pair of gas compressors, with an average timescale of approximately 3 days per cycle [201].

As illustrated in Figure 3.3, LXe first enters the TPC and skin from inlets at the bottom of the ICV. As it reaches the top of the active volume, contaminated xenon spills over three uniformly-spaced weirs, which set the liquid surface level in the TPC. This xenon flows into the weir reservoir – part of a collection of four vessels referred to as the LXe tower. Prior to passing through the hot zirconium getter, where electronegative impurities are removed [206], LXe is vaporised within a two-phase heat exchanger (HX) by transferring heat from purified GXe returning from the getter. The condensation of GXe is then controlled using a combination of liquid nitrogen thermosyphons and electric heaters at the subcooler stage, before being redelivered to the detector via vacuum-insulated transfer lines [204].

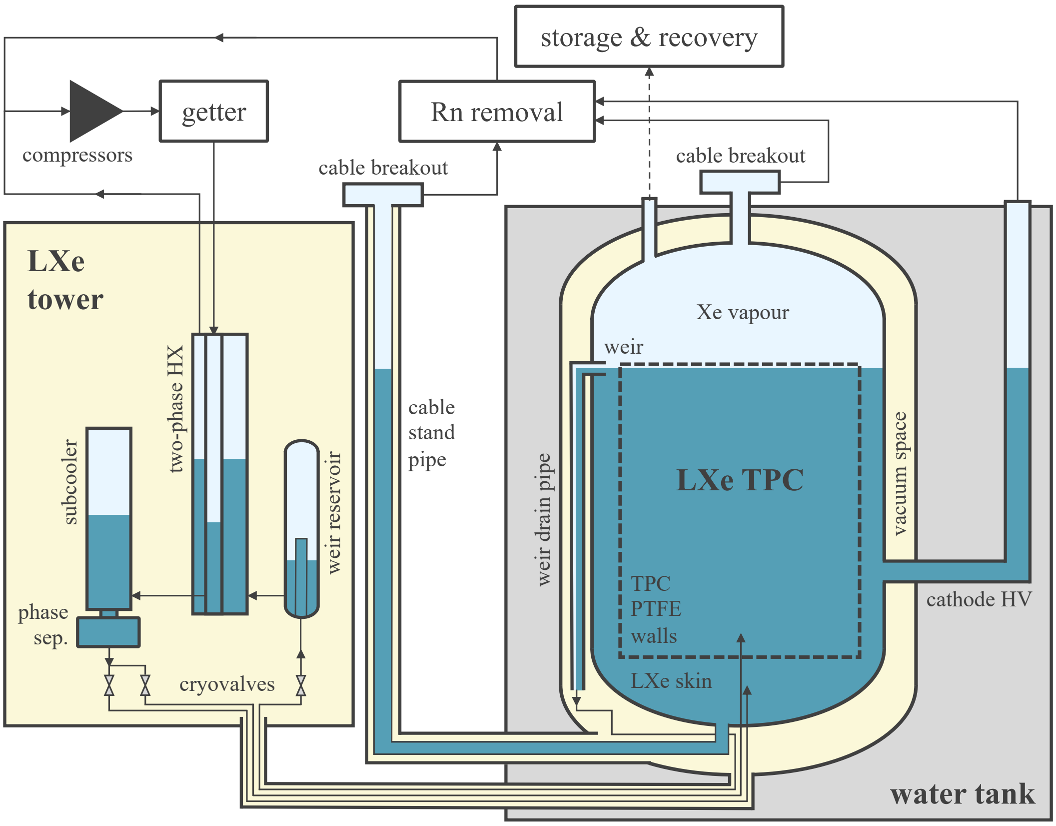

Figure 3.3: Simplified diagram of the LZ online xenon purification system. LXe from the detector flows along weir drain lines and into the LXe tower, where it is evaporated within a two-phase HX, purified in a hot zirconium getter, then subsequently condensed and returned to the cryostat. The OD acrylic tanks are omitted for clarity. This schematic is based on a similar figure from [201].

Since noble element impurities are not extracted by the getter, GXe present in the cable conduits is treated by an in-line radon reduction system (iRRS) as part of the circulation loop. This utilises a gas chromatography technique within a column of cold synthetic charcoal traps, whereby the slower propagation of radon with respect to xenon allows its sequestration for several half-lives [207, 208].

3.2 Particle interactions in xenon

A particle traversing through LXe can deposit energy by interacting with atomic electrons or elastically scattering off xenon nuclei – these processes are referred to as electronic recoils (ERs) and nuclear recoils (NRs), respectively. Since WIMPs exhibit a larger interaction cross section with xenon nuclei, NRs are typically considered signal-like, whereas ERs are background-like as they are primarily induced by betas or gammas from radioactive backgrounds. The energy E_0 deposited by a scatter is distributed across three channels: excitation, ionisation, and heat. This is summarised as

$$E_0 = N_{ex}E_{ex} + N_iE_i + \text{heat}, \tag{3.1}$$

where E_{ex} and E_i denote the average excitation and ionisation energies per atom, N_{ex} is the number of excited atoms, and N_i represents the number of electron-ion pairs [209]. Scintillation light produced by de-excitation is detected as the S1 signal, and extracted ionisation electrons form the S2 signal. However, since the TPC is not sensitive to heat, energy transferred to atomic motion or below the excitation or ionisation threshold of electrons is undetected and dissipates in the LXe.

A dependency on the interaction type is observed in the excitation to ionisation ratio N_{ex}/N_i – a value of ∼0.06–0.2 is observed for ERs [210], whereas this is ∼1 for NRs [211, 212]. The underlying physical mechanism responsible for this effect is not definitively known, though some hypotheses are discussed in [212, 213]. Nonetheless, this behaviour offers a powerful means to distinguish between NRs and ERs, and hence enables background discrimination.

3.2.1 Primary scintillation (S1)

Primary scintillation light is emitted by the relaxation of excited diatomic xenon molecules Xe_2^* (excimers), which are produced by two distinct mechanisms [214].

The first results directly from the impact of an incoming particle χ:

$$\chi + \text{Xe} \longrightarrow \chi + \text{Xe}^* \tag{3.2}$$

$$\text{Xe}^* + \text{Xe} \longrightarrow \text{Xe}_2^{*,v} \tag{3.3}$$

where the superscript labels indicate whether the nature of the excitation is electronic ($*$) or vibrational (v). Whereas vibrational de-excitation occurs via collisions with neighbouring atoms and is non-radiative, electronic relaxation involves the emission of a scintillation photon γ, followed by dissociation of the molecule due to a repulsive ground state potential:

$$\text{Xe}_2^{*,v} + \text{Xe} \longrightarrow \text{Xe}_2^* + \text{Xe} \tag{3.4}$$

$$\text{Xe}_2^* \longrightarrow 2\text{Xe} + \gamma. \tag{3.5}$$

On the other hand, excimers are also formed through the recombination of electrons with Xe^+ ions, as per

$$\chi + \text{Xe} \longrightarrow \chi + \text{Xe}^+ + e^- \tag{3.6}$$

$$\text{Xe}^+ + 2\text{Xe} \longrightarrow \text{Xe}_2^+ + \text{Xe} \tag{3.7}$$

$$\text{Xe}_2^+ + e^- \longrightarrow +\text{Xe}^{**} + \text{Xe} \tag{3.8}$$

$$\text{Xe}^{**} + \text{Xe} \longrightarrow \text{Xe}^* + \text{Xe} + \text{heat} \tag{3.9}$$

$$\text{Xe}^* + 2\text{Xe} \longrightarrow \text{Xe}_2^* + \text{Xe} + \text{heat} \tag{3.10}$$

$$\text{Xe}_2^* \longrightarrow 2\text{Xe} + \gamma \tag{3.11}$$

where the amount of recombination is strongly dependent on the applied external field and the surrounding ionisation density. In general, the presence of an electric field reduces the probability of recombination and thus increases the charge yield, whereas charged species such as alpha particles raise the local ionisation density and hence induce more recombination [214]. Moreover, recombination can also be affected by the energy scales involved. For instance, MeV-scale interactions can introduce additional processes such as bi-excitonic quenching, which lead to a decreased light yield [215].

In both mechanisms, the scintillation photons are emitted with a mean vacuum ultraviolet (VUV) wavelength of 175 nm in transitions to the molecular ground state ${}^1\Sigma_g^+$, from either the singlet state ${}^1\Sigma_u^+$ or triplet state ${}^3\Sigma_g^+$ with respective lifetimes of (3.1 ± 0.7) ns and (24 ± 1) ns [202, 216]. The process of recombination is slower than direct excitation, as it depends on the thermalisation time of the ionised electrons, which introduces a third component with a lifetime of (33 ± 1) ns [217].

3.2.2 Secondary scintillation (S2)

Ionised electrons that avoid recombination are drifted towards the liquid surface, where they must overcome a potential barrier to enter the GXe phase. This is enabled by the extraction field, with which the electrons are then accelerated and undergo electroluminescence: secondary scintillation light emitted according to the same mechanism as primary scintillation, with the excimers formed by collisions with the electrons. The electroluminescence yield N_{EL}, defined as the number of scintillation photons emitted per electron propagating through a path length x in GXe, is parametrised as

$$\frac{dN_{\mathrm{EL}}}{dx} = \alpha E_g - \beta P - \gamma, \tag{3.12}$$

where E_g is the electric field strength in GXe held at a pressure of P, and the empirically determined constants are $\alpha = 0.137/\mathrm{V}$, $\beta = 177/\mathrm{bar/cm}$, and $\gamma = 45.7/\mathrm{cm}$ [214]. The S2 signal is orders of magnitude larger than the S1; for nominal values of $E_g = 10.2\,\mathrm{kV/cm}$ and $P = 1.8\,\mathrm{bar}$, a single extracted electron would generate $\mathcal{O}(10^3)$ VUV photons over the 0.8 cm liquid surface-anode distance. This level of amplification provides sensitivity to interactions at very low energies.

3.2.3 Signal yields

The measured number of photons, n_γ, and number of electrons, n_e, are related to N_{ex} and N_i from Equation 3.1 by the recombination probability r:

$$n_\gamma = N_{ex} + rN_i, \tag{3.13}$$

$$n_e = N_i(1 - r), \tag{3.14}$$

and it is worth emphasising that recombination does not affect the total number of quanta – only the relative proportions between the light and charge yields, such that

$$n_\gamma + n_e = N_{ex} + N_i. \tag{3.15}$$

The efficiency of producing scintillation light can be quantified with the factor $W_\gamma = E_0/n_\gamma$. The maximum number of primary scintillation photons would be generated for an electric field strength of zero, in which case $r \approx 1$ and essentially all electron-ion pairs recombine, such that $n_\gamma = N_{ex} + N_i$ and

$$W_\gamma^{\min} = \frac{E_0}{N_{ex} + N_i}, \tag{3.16}$$

where $W_\gamma^{\min} \equiv W$ corresponds to the minimum energy required to generate a single scintillation photon. This factor is a constant under the assumption that the ratio N_{ex}/N_i is independent of energy. In general, the measured (13.7 ± 0.2) eV W-value is commonly adopted [212], though a conflicting value of (11.5 ± 0.6) eV has emerged in recent years [218, 219]. By re-arranging the expression above and invoking Equation 3.15, a combined energy formula is obtained:

$$E_0 = W\left(n_\gamma + n_e\right), \tag{3.17}$$

which leverages the anti-correlation between light and charge quanta to reduce the impact of statistical fluctuations from recombination, hence leading to an improved energy resolution in comparison with considering each signal individually [220].

The observed S1 and S2 pulse areas are measured in units of photons detected (phd), for which the single photoelectron response of each PMT is uniquely calibrated. In order to maintain spatial uniformity in the detector response, the signals are adjusted for position-dependent effects according to

$$\mathrm{S1c} = \mathcal{C}_1(x, y, z)\,\mathrm{S1}, \tag{3.18}$$

$$\mathrm{S2c} = e^{t_d/\tau_e}\,\mathcal{C}_2(x, y)\,\mathrm{S2}, \tag{3.19}$$

where S1c and S2c represent the corrected signals. The three-dimensional S1 correction map $\mathcal{C}_1$ normalises the light collection efficiency to the centre of the detector, whereas the two-dimensional S2 correction map $\mathcal{C}_2$ accounts for radial variations such as those in the extraction field as a result of deflection in the gate and anode grids. The exponential factor in the S2 correction compensates for the loss of drifting charge to impurities in the LXe, with a finite electron lifetime of τ_e and a drift time t_d. The correction maps and τ_e are obtained using mono-energetic calibration sources that are dispersed throughout the TPC.

The numbers of emitted quanta n_γ and n_e are related to the corrected S1c and S2c signals by

$$\mathrm{S1c} = g_1 n_\gamma, \tag{3.20}$$

$$\mathrm{S2c} = \left(\epsilon_e N_{\mathrm{EL}} g_1^{\mathrm{gas}}\right) n_e = g_2 n_e, \tag{3.21}$$

where g_1 is the photon detection efficiency and g_2 is the effective charge gain. These are position-independent and intrinsic detector parameters, calibrated using a set of mono-energetic sources as demonstrated in Section 4.2. The parameter g_2 is composed as a product of three quantities: the electron extraction efficiency ϵ_e, the electroluminescence yield N_{EL}, and the photon detection efficiency in the GXe phase g_1^{gas}. With these definitions, the reconstructed energy may be calculated as

$$E_0 = W\left(\frac{\mathrm{S1c}}{g_1} + \frac{\mathrm{S2c}}{g_2}\right). \tag{3.22}$$

Although this formulation is effective for ERs, it does not account for energy transfer to heat and is hence not applicable to NRs. This can be rectified through the inclusion of a nuclear quenching factor L:

$$E_0^{\mathrm{NR}} = \frac{W}{L}\left(\frac{\mathrm{S1c}}{g_1} + \frac{\mathrm{S2c}}{g_2}\right), \tag{3.23}$$

with L modelled using the Lindhard theory for nuclear recoils [221], which predicts that $\leq 25\%$ of the energy is transferred to excitation and ionisation for NRs of $\leq 3\,\mathrm{MeV}$, and the rest is dissipated as heat.

3.2.4 Xenon as a detector medium

Xenon possesses several attributes that make it a favourable detector medium for rare event searches. It is inert, virtually absent of natural long-lived radioisotopes, and readily purifiable, all three of which necessary qualities for stable long-term operation. Moreover, the presence of the odd-neutron isotopes ^{129}Xe and ^{131}Xe facilitates searches for spin-dependent dark matter interactions [204].

In addition to a large atomic mass, which benefits from a coherent enhancement to the WIMP-nucleus interaction cross section as discussed in Section 1.3.3, LXe exhibits a high density of $\sim$3.0 g/cm^3, which leads to strong attenuation of radiation. As shown in Figure 3.4, photons with energies of $\mathcal{O}(100)$ keV and below are likely to undergo photoelectric absorption within 1 mm, whereas Compton scattering occurs within a few cm for higher energies. Attenuation is even greater for electrons, which typically travel < 1 cm as they lose energy rapidly through collisions and bremsstrahlung. This self-shielding trait—whereby external radiation is unlikely to penetrate LXe beyond a short distance—results in an extremely low background region towards the centre of a given LXe volume, and ultimately contributes towards the scalability of xenon-based detector technologies. However, one of the major limiting factors in constructing larger detectors is the high cost of xenon, especially in comparison with argon.

The high light and charge yields of xenon, as displayed in Figure 3.4, provide sensitivity to interactions at energies ranging from $\mathcal{O}(1)$ keV up to several MeV. The dependency of N_{ex}/N_i on interaction type enables discrimination between NRs and ERs, and hence facilitates efficient background rejection. Furthermore, the ratio between singlet and triplet state populations also varies with particle type and energy, thus presenting an additional method for particle identification using pulse shape discrimination [222]. This characteristic is particularly pronounced in the case of argon, where a difference of $\sim$1.5 µs has been measured between the singlet and triplet state lifetimes [223].

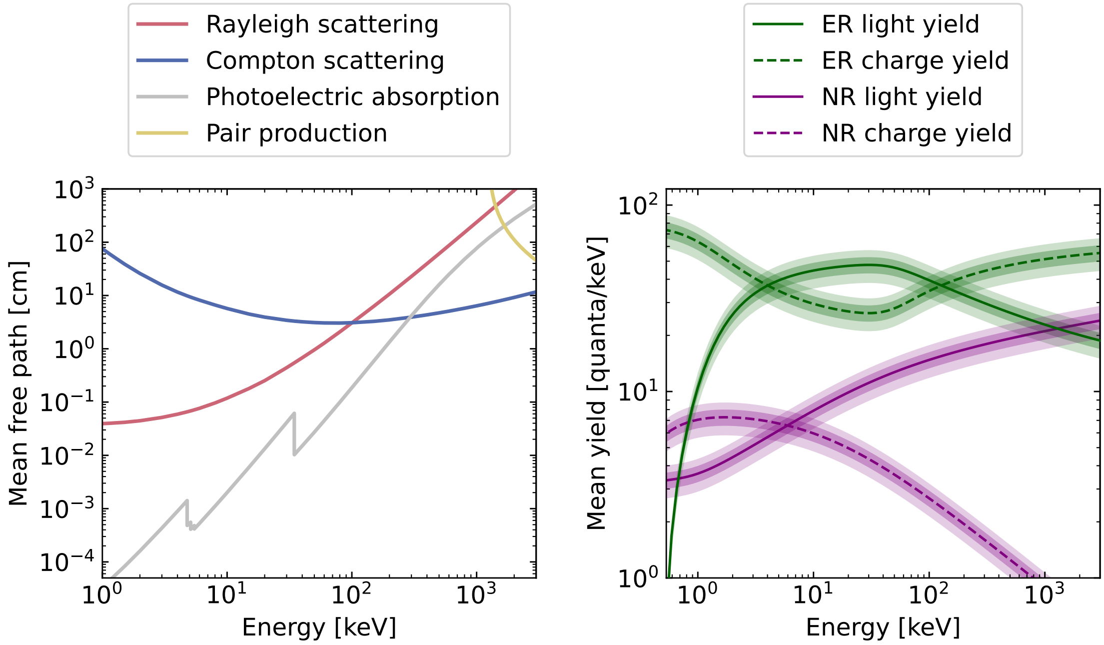

Figure 3.4: The mean free path of photons traversing LXe as a function of energy, broken down into different electromagetic processes, with data referenced from [224] (left); the light and charge yields of ERs and NRs in LXe for a nominal drift field of 310 V/cm, as modelled semi-empirically by NEST [225, 226] (right). The error bands indicate $\pm 1\sigma$ and $\pm 2\sigma$ systematic uncertainties.

3.3 Backgrounds

In order to attain unambiguous detection of new physics, it is imperative to understand and minimise sources of background; the design choices and construction process of the detector were heavily influenced by this fact. The main expected backgrounds in LZ are highlighted in the following sections.

3.3.1 Trace radioactivity

The presence of naturally-occurring radioisotopes embedded within the detector components introduces a gamma-ray background. These primarily consist of the isotopes ^{60}Co and ^{40}K, along with ^{238}U, ^{232}Th, and their progeny. In the case of the ^{238}U and ^{232}Th chains, neutrons are also generated by (α, n) reactions and spontaneous fission. The impact of these sources is well-defined and minimised by a comprehensive radioassay and material selection programme, as well as the self-shielding property of LXe [227]. Although gamma rays from detector materials only form a small contribution to the WIMP signal region, they are a dominant background in higher energy searches at >100 keV; producing a detailed model of this background is the focus of Chapter 4.

3.3.2 Surface and dispersed contaminants

In the construction of LZ, one major concern was the accumulation of dust on detector surfaces and exposure to air, which lead to the plate-out of ^{222}Rn and its progeny. These radioisotopes can subsequently emanate from detector surfaces and disperse throughout the LXe. Daughters that undergo alpha decay, such as ^{218}Po and ^{214}Po, can result in the emission of neutrons through (α, n) reactions, predominantly in the PTFE [228]. Although neutrons typically scatter several times, a single NR induced by a neutron is indistinguishable from that of a WIMP, which poses an important background when combined with the imperfect OD tagging efficiency. On the other hand, a problematic background also originates from naked beta decays of ^{214}Pb daughters, whereby beta emission is unaccompanied by a gamma ray and is hence difficult to tag [229]. Similar situations that arise from the escape of an accompanying gamma are referred to as semi-naked beta decays. To restrict the amount of ^{222}Rn, the component transport and assembly of the LZ detector also adhered to strict quality assurance and cleanliness protocols [227].

Trace levels of ^{85}Kr and ^{39}Ar present in natural xenon mixtures can also contribute a flat ER background to the WIMP signal region. Since noble elements are not removed by the getter, the concentration of these isotopes was reduced by purifying the xenon inventory using a charcoal chromatography technique in the early development phase [204].

3.3.3 Cosmogenic and laboratory backgrounds

Within the Davis Cavern, the exposure to cosmic rays is significantly reduced by the rock overburden. The underground muon flux is lower by a factor of $\sim 10^6$ with respect to the surface, and remaining muons are readily detected by the OD.

Muon-induced showers in the surrounding rock can produce neutrons, though these are moderately attenuated by the water tank [204, 230]. In addition, decays of radioisotopes in the cavern walls also contribute to the gamma-ray background; these have been thoroughly characterised by *in situ* measurements with a sodium iodide detector [231].

During storage and transport, background sources such as ^{127}Xe and ^{37}Ar were produced by the cosmogenic activation of xenon through spallation. After the inventory was moved underground, these gradually diminished over the course of detector commissioning and early runs. This was accounted for with a detailed model of the expected activation product concentrations over time [232].

3.3.4 Physics backgrounds

Due to the unprecedented sensitivity of LZ, signals from rare Standard Model processes can form backgrounds to searches for new physics. With a half-life of $(2.17 \pm 0.08) \times 10^{21}$ y, the $2\nu\beta\beta$ decay of ^{136}Xe pervades energies up until the 2457.8 keV endpoint [233]. Furthermore, low-energy signatures from the two-neutrino double electron capture of ^{124}Xe can form a background to searches for low mass dark matter candidates in addition to WIMPs. The decay of ^{124}Xe is studied in Chapter 5.

A variety of neutrino sources present an irreducible background to LZ. ERs from solar neutrinos mainly consist of *pp* neutrinos, with smaller proportions from the ^{7}Be and CNO chains. Neutrinos can also induce NRs through coherent elastic scattering with xenon nuclei; low-energy NRs are produced by ^{8}B and *hep* neutrinos, whereas atmospheric and diffuse supernova neutrinos induce higher energy NRs [229].

3.3.5 Non-standard backgrounds

A subset of backgrounds originates from irregular event topologies and features of the detector. For instance, gamma rays with multiple interaction sites in the TPC can display an artificially lowered S2 size as a result of charge loss to the RFR for vertices below the cathode. The outcomes closely resemble NRs, and are termed multiple scatter single ionisation (MSSI) events. In addition, accidental coincidence backgrounds can occur from false pairings of uncorrelated S1s and S2s. Such backgrounds are addressed by sophisticated data quality cuts and fiducialisation.

3.4 Calibrations

A comprehensive calibration strategy was designed in order to develop a thorough understanding of the LZ detector, ranging from tuning event reconstruction algorithms and detector parameters, to quantifying the detector response to ERs and NRs as demonstrated in Figure 3.5. This information is also critically used to produce accurate simulations, which are an integral part of statistical analyses in searches for new physics. A summary of the calibration sources employed by LZ is given in Table 3.1, with a description of each category below.

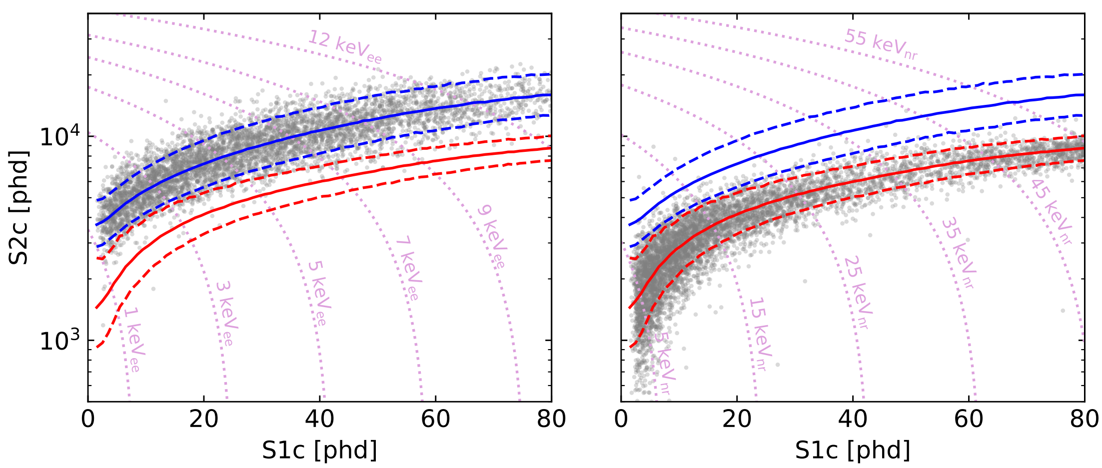

Figure 3.5: Calibration of the LZ detector response for ERs with tritium data (left) and for NRs with DD data (right). Solid lines represent the band medians and dashed lines indicate the 10th and 90th percentiles. Dotted lines trace contours of constant electron-equivalent energy (keV_{ee}) and nuclear recoil energy (keV_{nr}). These plots were reproduced with data presented in [142].

Table 3.1: List of calibration sources utilised in LZ and their corresponding purpose, categorised by method of deployment. Internal sources are injected into the LXe, external sources are set outside the OCV, and CSD sources are lowered into the vacuum space between the ICV and OCV. Primary source features are presented, though in some cases additional gamma lines or subsequent decay chains are also involved. Based on information from [201, 204].

Category	Source	Interacting particle	Half-life	Purpose
Internal	Tritium (^{3}H)	β ($Q = 18.6$ keV)	12.3 y	ER band
	$^{83\text{m}}$Kr	32.1 keV γ + 9.4 keV γ	1.8 h	TPC (x, y, z)
	$^{131\text{m}}$Xe	163.9 keV cascade	11.8 d	TPC (x, y, z)
	^{220}Rn	various α, β, γ	10.6 h	ER band
External	^{88}YBe	152 keV n	107 d	low-energy NRs
	^{124}SbBe	22.5 keV n	60.2 d	low-energy NRs
	DD (direct)	2450 keV n	-	NR yields
	DD (D-ref.)	272–400 keV n	-	NR yields
	DD (H-ref.)	$\leq$100 keV n	-	NR yields
CSD	^{241}AmLi	$\leq$1.5 MeV n	432 y	NR band
	^{241}AmBe	$\leq$11 MeV n	432 y	NR band
	^{252}Cf	spontaneous fission n	2.65 y	NR efficiency
	^{57}Co	122 keV γ	0.74 y	skin threshold
	^{22}Na	2×511 keV γ	2.61 y	detector sync
	^{228}Th	2615 keV γ, etc.	1.91 y	energy scales

3.4.1 Internal sources

Internal calibrations refer to instances where a given source is injected into the LXe using a xenon carrier gas, subsequently dispersing uniformly throughout the TPC. This form of deployment is used to overcome the self-shielding property of xenon in the case of low-energy ER calibrations, where external sources would be impractical. The metastable mono-energetic sources $^{83\text{m}}$Kr and $^{131\text{m}}$Xe are utilised to calibrate for spatially-varying detector efficiencies, such as the light collection efficiency and the electron extraction efficiency. As opposed to ^{222}Rn, ^{220}Rn has no long-lived daughters and hence it offers a convenient source of large S1s due to the high light yield associated with NRs induced by alpha decays. This is predominantly applicable to calibrations of the LXe skin, as well as for studies involving tagging of time-coincident parent-daughter pairs [234]. Tritium, introduced in the form of tritiated methane, generates a beta spectrum with an 18.6 keV endpoint energy and is thus ideal for characterising the detector response to ERs down to threshold. Although it has a considerably long half-life, tritium is effectively removed by the getter with a time constant that is shorter than the circulation timescale, as demonstrated in LUX [235].

3.4.2 External sources

Photoneutron (γ, n) sources such as ^{88}YBe are useful for probing the low-energy NR response for the $\leq 4.6\,\mathrm{keV_{nr}}$ region, where depositions from ^{8}B coherent neutrino scattering are expected. Such sources are deployed in a tungsten vessel, which is lowered onto the top of the OCV. On the other hand, a deuterium-deuterium (DD) fusion source facilitates *in situ* calibrations of the NR response over a broad energy range, as was originally developed for LUX [236]. This source delivers mono-energetic neutrons at a high rate, along conduits penetrating the water tank and OD. Along with a direct mode, two additional modes are available in which the incident neutron energies are attenuated by scattering off a deuterium-based (D-reflector) or hydrogen-based (H-reflector) target prior to entering the conduit.

3.4.3 Calibration source deployment

Various sources are delivered into the vacuum space between the ICV and OCV by a calibration source deployment (CSD) system, through one of three vertical stainless steel tubes with precise positioning along the height of the TPC. With this system, broad-spectrum (α, n) neutron sources such as ^{241}AmLi are used to obtain the NR band, whereas neutrons from the spontaneous fission of ^{252}Cf can enable measurements of the NR signal efficiency as well as the OD detection threshold. Gamma-ray sources are also deployed to calibrate of the veto systems, match inter-detector and intra-detector timings, and characterise the high energy response of the TPC.

3.4.4 PMT calibrations

In addition to characterising the detector response with radioactive sources, the response and performance of PMTs is monitored with intermittent LED calibrations. The top and bottom TPC PMT arrays are each instrumented with 24 470 nm LEDs, which can pulse at low voltage to track the single photoelectron gains over time, or produce flashes with $\mathcal{O}(100)$ photons to check for afterpulsing, which is caused by residual gases in the PMTs and hence serves as a measure of their vacuum integrity. Similarly, 12 and 18 LEDs are installed at the top and bottom of the side LXe skin, respectively. For the OD, a dedicated optical calibration system was implemented, with which photons are injected through duplex optical fibres from 30 positions on the PMT ladders and 5 points below the acrylic vessels [237].

3.5 Analysis

Workflows within LZ are heavily underpinned by an assortment of modular software packages, with applications ranging from detector modelling and event reconstruction to standardised cut implementation and statistical inference. A brief overview of the core frameworks utilised by LZ is given below, leading from simulations through to exclusion limit setting.

3.5.1 Simulation and reconstruction

Monte Carlo simulations in LZ are performed with BACCARAT, which propagates and tracks particles through a detailed model of the detector geometry using Geant4 [238, 239]. The outputs of BACCARAT can be processed with two different simulation chains:

- **Full chain** – energy deposits in each event are clustered, then translated into scintillation photons and ionisation electrons with the Noble Element Simulation Technique (NEST), which simulates signal production mechanisms in noble element detectors using semi-empirical models [225, 226]. Recorded photon hits on PMTs are then passed to a detector electronics response (DER) package, which simulates the PMT response and electronics chain to generate digitised waveforms, organised in the same structure as raw files from the data acquisition (DAQ) system. The result is realistic and can be treated like real data, enabling early development and refinement of the reconstruction framework and event-by-event analyses, as well as assessments of detector design features. However, this chain is computationally intensive due to the high level of detail associated with optical tracking and PMT signal generation.

- **Fast chain** – rather than tracking individual VUV photons, clustered energy deposits are directly converted into estimates of the S1 and S2 signals using NEST. Detector effects are implemented in the form of averaged quantities and parametrised models; this approach readily delivers sizeable datasets, which is ideal for background rate measurements and sensitivity studies, but comes at the expense of reduced accuracy.

Raw waveforms—from either the DAQ or the full simulation chain—are processed into analysis-ready quantities by LZap, the event reconstruction package. A multitude of operations are conducted at this stage, such as pulse finding, pulse classification with machine learning [240], and pulse area corrections. Position reconstruction is performed using the Mercury algorithm, a maximum-likelihood approach utilising light response functions that predict the response of each PMT to emission of light from arbitrary distances [241, 242]. Moreover, an interaction finder categorises events by their topology: a single S1-S2 pair is labelled as a single scatter (SS); an S1 followed by multiple S2s as a multiple scatter (MS); multiple S1s and S2s in an ambiguous order as pile-up; and isolated S1s, S2s, or noise as 'other'. These algorithms are mainly tuned with calibration data, as well as full chain simulations and hand-labelled data inspected with an offline event viewer. The reconstruction quality is generally limited by detector effects – for example, the longitudinal diffusion of drifting electrons from a MS event can affect the separability of S2s, and hence the distinguishability between SS and MS interactions.

3.5.2 WIMP sensitivity

The sensitivity of LZ is estimated with a frequentist hypothesis-testing framework using the two-sided profile likelihood ratio (PLR) test statistic, as is commonly employed for rare event searches [243, 244]. The PLR is evaluated in (S1c, S2c) space to exploit the ER-NR discrimination property of xenon, with signal and background model probability distribution functions (PDFs) generated using simulations, and associated normalisations set by expected rates following the application of analysis cuts. A scan over cross section values—and hence the number of signal events—is conducted for a range of WIMP masses, and repeated hypothesis tests are performed to obtain a 90% confidence level median and upper limit for each mass. The projected sensitivity curve for an exposure of 1000 live days and a fiducial mass of 5.6 tonnes is illustrated in Figure 3.6, along with recently published upper limits. A peak sensitivity of $1.6 \times 10^{-48}\,\mathrm{cm}^2$ is predicted for a WIMP mass of $40\,\mathrm{GeV/c}^2$ [229]. At lower masses, the sensitivity is limited by the detection threshold, set in part by an imposed three-fold PMT coincidence cut to negate dark count coincidences, whereas at higher masses this is due to an inversely proportional relationship with the signal rate, given a constant local density.

3.5.3 Science Run 1

The first official run of LZ—referred to as Science Run 1 (SR1)—spanned a total of 139 calendar days, between the 23rd of December 2021 and the 11th of May 2022. With the removal of calibration runs and anomalous high-rate periods, as well as a 3% loss to DAQ dead time, the SR1 dataset consisted of 89.6 live days. This was accompanied by a comprehensive set of dedicated data quality cuts, comprised of: fiducialisation and vetos to reject MS events; S1 and S2 pulse shape-based cuts to suppress accidental backgrounds and misreconstructed events; hold-offs and exclusion cuts to eliminate periods of elevated detector activity, primarily induced by large S2s and muons. The final class of cuts further reduced the live time to a total of 60 days, which contained a clean sample of 335 SS events after all analysis cuts [142].

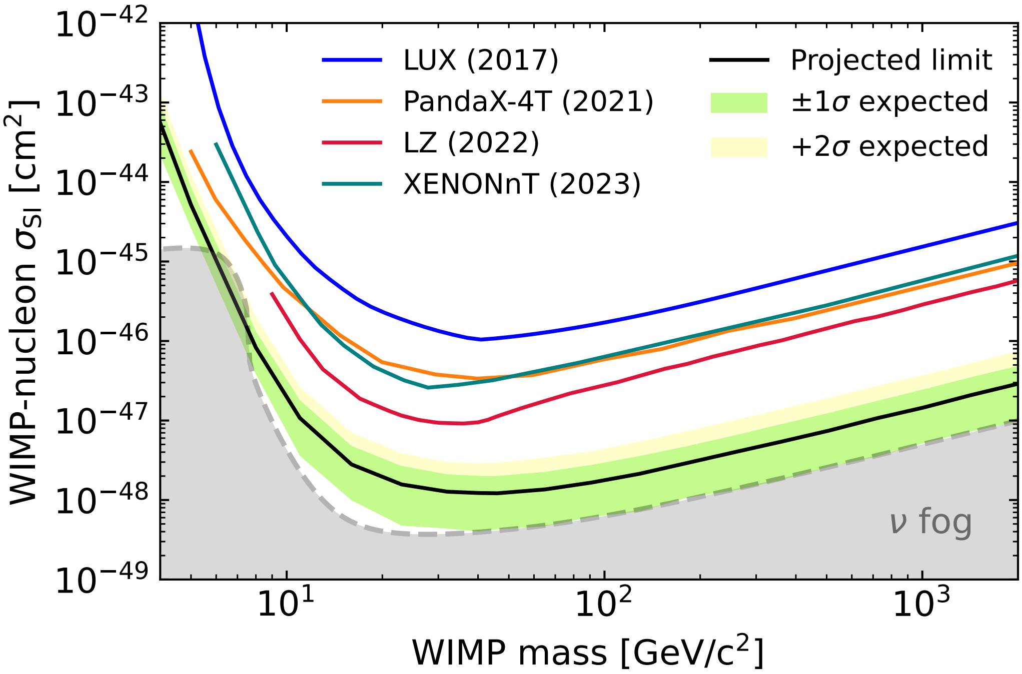

Figure 3.6: Projected LZ sensitivity to spin-independent WIMP-nucleon elastic scattering for an exposure of 1000 live days and a fiducial mass of 5.6 tonnes, with an assumed 99.5% discrimination and a 50% NR acceptance; curve reproduced and updated from [229]. Recent limits from other xenon-based experiments are also shown [141, 143, 144], along with the power-constrained limit obtained from the first LZ WIMP search result [142]. The grey shaded region marks the onset of backgrounds from coherent neutrino-nucleus scattering, using the definition of the neutrino fog discussed in Section 1.3.3.

To maintain stable electric fields and tackle increased light emission in the form of hotspots, the operating grid voltages were reduced in SR1 with respect to the nominal settings. Moreover, a selection of 12 TPC PMTs and 2 skin PMTs were disabled due to excessive noise. Comparisons between the predicted and measured SR1 values are summarised for a set of key detector parameters in Table 3.2. The main difference is the decreased charge yield as a consequence of the lower extraction field. Nonetheless, a world-leading limit was achieved with the SR1 exposure, as demonstrated in Figure 3.6 [142]. A power constraint was applied to the 19-26 GeV/c^2 mass range for this result to treat under-fluctuations in the background rate [244]. As of writing, LZ is collecting data for a longer exposure, which will facilitate more stringent limits and open avenues for other interesting searches, such as the potential first detection of ^{8}B neutrinos.

Table 3.2: Comparison of key detector parameters between nominal values assumed in sensitivity predictions [229], and values measured for SR1 [142].

Detector parameter	Nominal value	SR1 value
g_1 [phd/photon]	0.119	(0.114 ± 0.002)
g_2 [phd/electron]	79	(47.1 ± 1.1)
Electron lifetime [μs]	850	>5000
Anode grid voltage [kV]	+5.75	+4.00
Gate grid voltage [kV]	−5.75	−4.00
Cathode grid voltage [kV]	−50.0	−32.0
Bottom grid voltage [kV]	−1.50	−1.25
Drift field [V/cm]	310	193
Extraction field (GXe) [kV/cm]	10.2	7.3
Electron extraction efficiency [%]	95.0	80.5
Fiducial mass [tonnes]	5.6	(5.5 ± 0.2)
LXe temperature [K]	175.0	174.1
LXe pressure [bar]	1.80	1.79

3.5.4 $0\nu\beta\beta$ decay sensitivity

The LZ detector possesses several favourable features for conducting $0\nu\beta\beta$-decay searches: an ultra-low background environment, owing to meticulous selection of radiopure materials, underground operation, and the self-shielding property of xenon; excellent energy resolution, accomplished through the combination of both scintillation and ionisation channels; and a large quantity of xenon, which contains a pair of candidate isotopes to study – ^{134}Xe and ^{136}Xe. For the former, there is the added potential for a first observation of $2\nu\beta\beta$ decays as well, with a predicted half-life of $\sim 10^{24}$ years [245]. At natural isotopic abundances of (10.436 ± 0.002)% and (8.857 ± 0.004)%, the 7-tonne active LXe volume contains approximately $\sim$731 kg and $\sim$620 kg of ^{134}Xe and ^{136}Xe, respectively [246]. This is comparable to the amounts deployed in dedicated experiments with isotopic enrichment, such as KamLAND-Zen 800, which contains $\sim$677 kg of ^{136}Xe [179].

With a Q-value of 824.2 keV [184], the signal for ^{134}Xe $0\nu\beta\beta$ decay is located in an energy region with a relatively flat background. However, the comparatively lower

Q-value with respect to that of ^{136}Xe at 2457.8 keV translates into a half-life that is $\sim 10^3$ times longer, and hence the focus is predominantly on ^{136}Xe $0\nu\beta\beta$ decay. In particular, the sensitivity of this search is most heavily impacted by the rate of a 2447.7 keV ^{214}Bi gamma-ray line within close proximity to the signal peak. Since this originates from the decay chain of ^{238}U, a naturally occurring radioisotope that is embedded within the detector materials, selecting an inner detector volume attenuates the background rate drastically, as demonstrated in Figure 3.7. Otherwise, this background can be rejected by tagging a coincident gamma, or alternatively the short-lived ^{214}Po daughter in the case of naked decays without an associated gamma. The distinguishability of the two peaks also critically depends on the energy resolution at $Q_{\beta\beta}$. Furthermore, given that $0\nu\beta\beta$ signals should produce SS events, the discrimination power for MS backgrounds is tied to the depth-dependent separability of S2s, which is limited by the vertical position resolution.

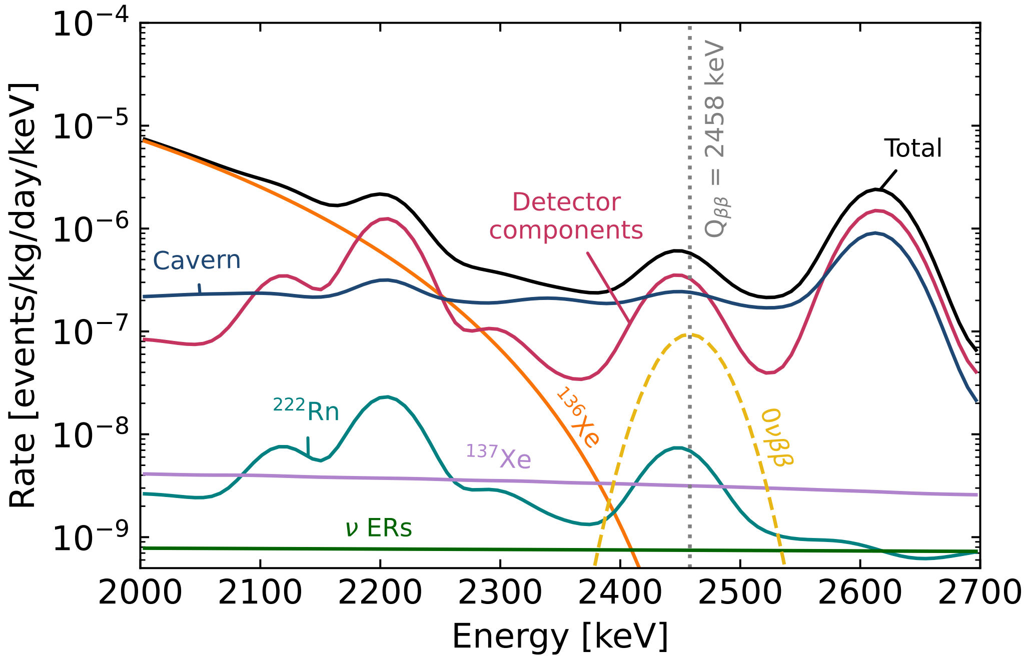

Figure 3.7: Simulated energy spectra for backgrounds around the ROI of ^{136}Xe $0\nu\beta\beta$ decay, within a central 967 kg volume, and following skin and OD coincidence vetos. The background rates were modelled using assays and projections reported in the WIMP sensitivity paper [229]. The signal spectrum is indicated by a dashed peak, for an assumed 1% energy resolution at $Q_{\beta\beta}$. This plot was reproduced from the corresponding LZ sensitivity paper [247].

For the sensitivity projection, the PLR method was applied for three observables – energy, radial position, and depth (E, R^2, z). This was evaluated for an extended 5.6 tonne volume, with a conservative 1% energy resolution and a signal detection efficiency of 80% assumed. The median sensitivity profile at 90% confidence level as a function of live time is shown in Figure 3.8. At the nominal exposure of 1000 live days, the expected exclusion sensitivity to the half-life reaches 1.06×10^{26} years, which could be upgraded to 1.06×10^{27} years with a 90% ^{136}Xe enrichment campaign after the WIMP search programme [247]. For the SR1 exposure, the exclusion limit would reach approximately 2.4×10^{25} years. With longer runs underway, LZ is on track to achieve a result that is competitive with dedicated $0\nu\beta\beta$ experiments.

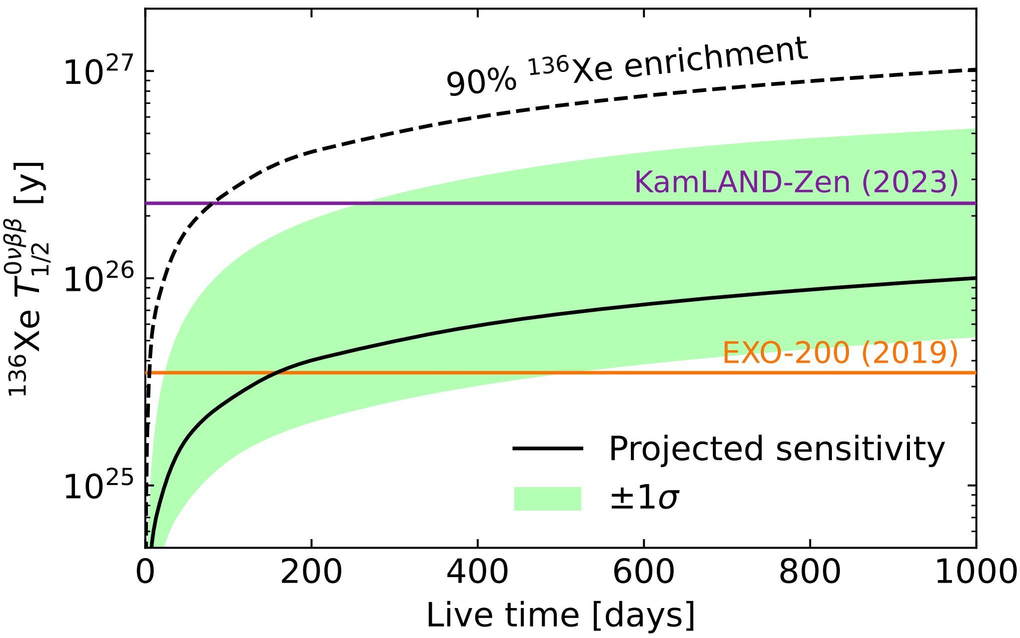

Figure 3.8: Projected median sensitivity at 90% confidence level for the half-life of ^{136}Xe $0\nu\beta\beta$ decay as a function of live time. The predicted sensitivity is highly competitive with the latest results of dedicated experiments, and this is bound to improve with refinements to the energy resolution and background rejection techniques. This plot was reproduced and updated from the official sensitivity paper [247].

4 Detector background model fitting

This chapter outlines the development of a framework for measuring the contribution of detector materials to the SR1 background model of LZ, by means of fitting simulated energy spectra to data. To reduce the level of complexity posed by considering numerous components, a novel approach involving a series of fits within different spatial partitions of the detector was employed. Moreover, a dedicated energy calibration was performed, along with corrections for subtle energy reconstruction effects to improve fit robustness. The results of this work have contributed towards the background model of the first WIMP search results of LZ [142, 248], and set the foundations for background models in upcoming high energy searches.

4.1 Context and motivation

The two main sources of background in the LZ detector are expected to arise from ^{222}Rn and its progeny, along with the fixed inherent radioactivity of the detector materials [201]. Contributions from the former were minimised through rigorous cleanliness and quality assurance protocols; the detector was assembled in a dedicated cleanroom to ensure that accumulated surface contamination did not exceed stringent requirements. The latter was handled with careful selection and manufacture of each component prior to construction, under an extensive radioassay campaign. The results from these measurements formed a comprehensive database that informs background models in LZ [227].

Contaminants embedded in the detector components and surrounding cavern rock consist of naturally occurring radioactive materials, as well as anthropogenic isotopes. The most prevalent of these are:

- **^{238}U & ^{232}Th** – these chains radiate particles at various energies in their decays, eventually down to stable isotopes of lead. Both chains, depicted in Figures 4.1 and 4.2, are split by their very long-lived radium isotopes into 'early' and 'late' segments. This helps to account for breaks in secular equilibrium induced by chemical processes at the manufacturing stage, as observed from differing concentrations of isotopes in the early and late chains.

- **^{60}Co** – undergoes beta decay to ^{60}Ni with a half-life of 5.27 years, with two prominent gamma-ray energies of 1173.2 keV and 1332.5 keV. It is possible for these to be occasionally detected in coincidence as an SS event, in which case a summed 2505.7 keV peak is formed.

- **^{40}K** – undergoes either beta decay to ^{40}Ca or electron capture to ^{40}Ar, with branching ratios of 89.28% and 10.72% respectively, and has a half-life of 1.2×10^9 years. The decay to ^{40}Ar has an associated 1460.8 keV gamma ray from the de-excitation of the daughter nucleus.

With the detector assembled and operational, it becomes possible to validate expectations from radioassay measurements with fits to data. This has significant implications for setting material assay and screening requirements in the context of larger next-generation dark matter detectors, such as the recent XLZD consortium [158]. Although gamma rays from detector materials present a small contribution to the WIMP ROI, characterising these backgrounds towards higher energies is also particularly important for understanding the sensitivity of LZ to other new physics. For instance, as part of the ^{238}U chain, beta decays of ^{214}Bi can produce a 2447.7 keV gamma, which introduces a problematic background to the 2457.8 keV signal of ^{136}Xe $0\nu\beta\beta$ decay searches due to the limited energy resolution [247]. In addition, by leveraging simulations with fits to data, building a detailed model

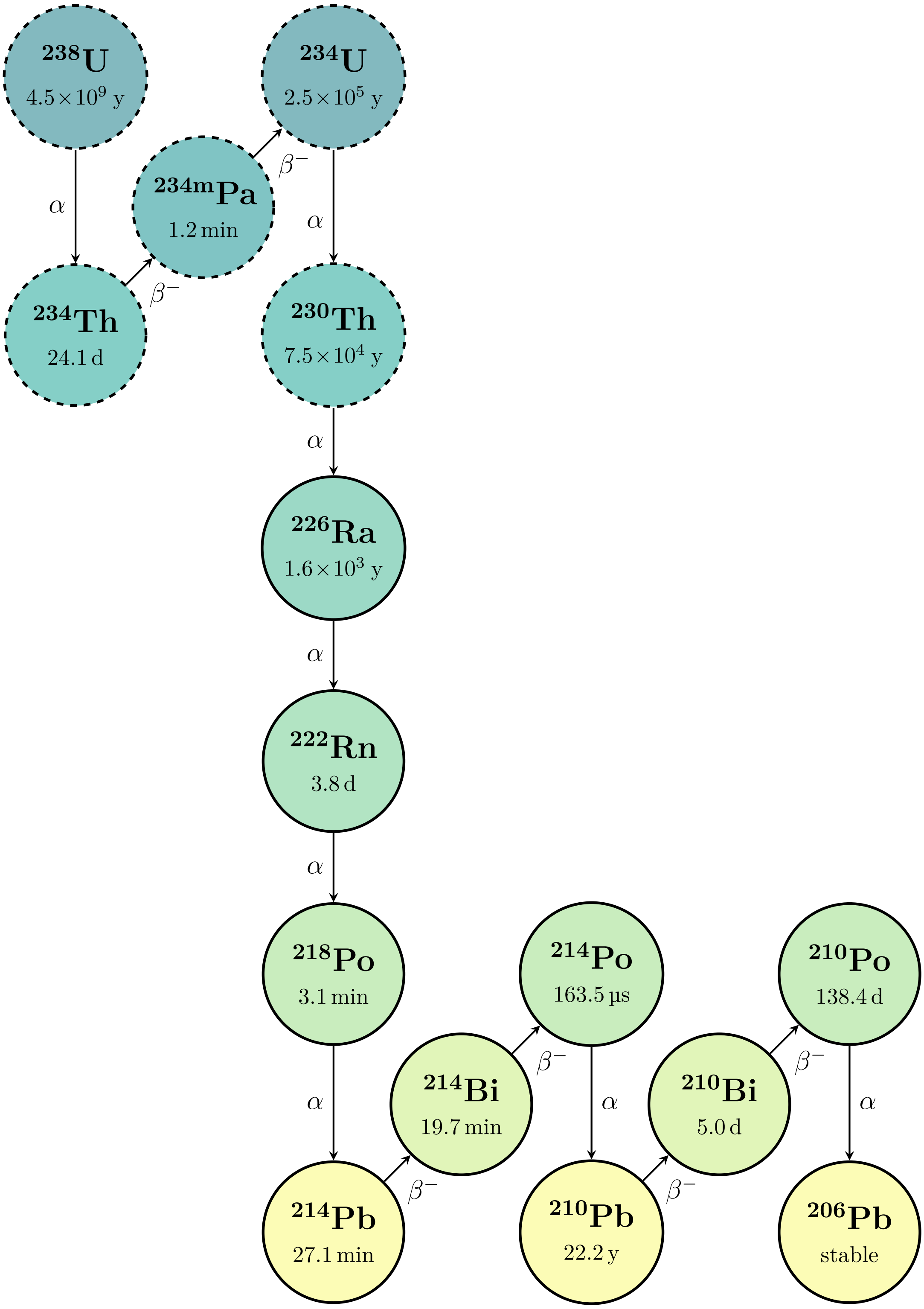

Figure 4.1: Diagram of the ^{238}U decay chain. Dashed and solid borders indicate early and late chain segments, respectively. For brevity, stages with a $< 99\%$ branching ratio are omitted. The data was sourced from the IAEA nuclides database [249].

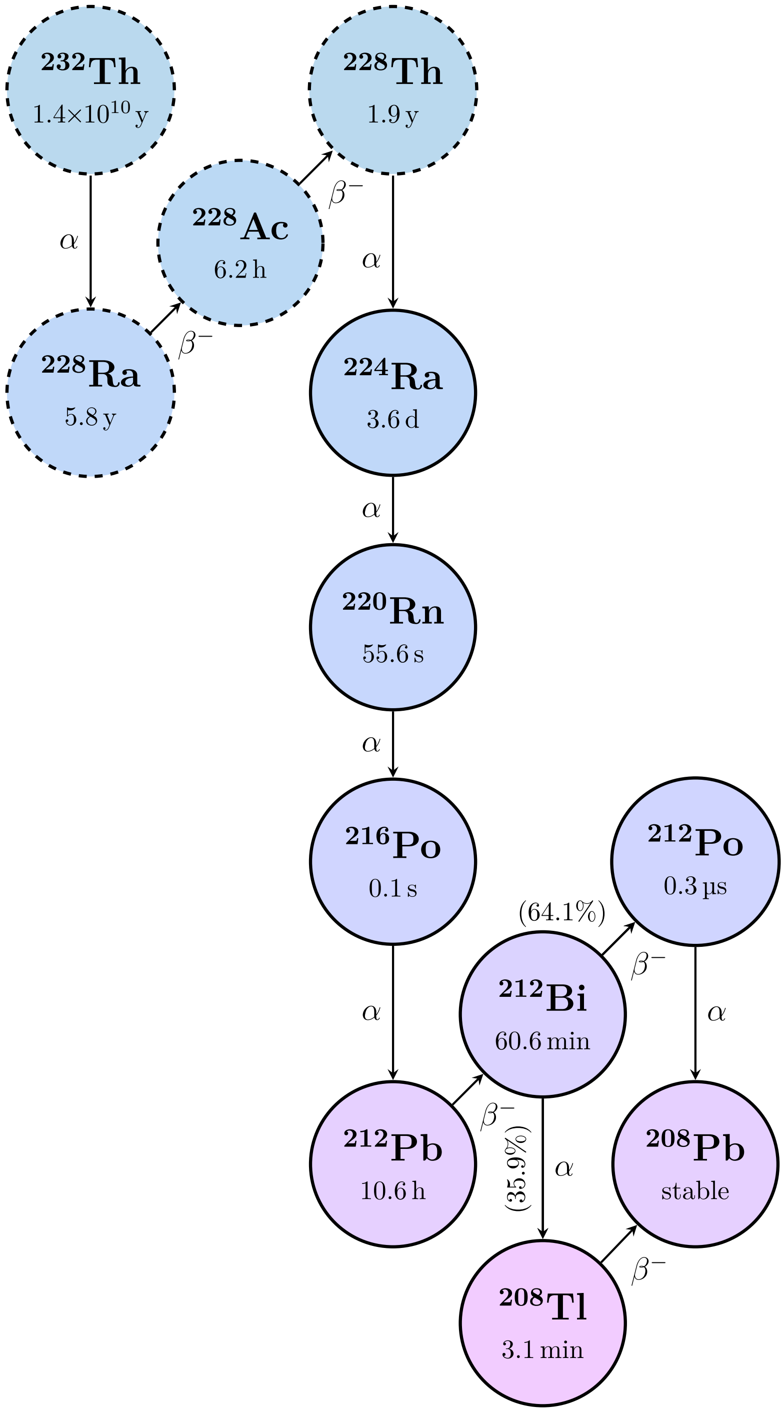

Figure 4.2: Diagram of the ^{232}Th decay chain. Dashed and solid borders indicate early and late chain segments, respectively. The data was sourced from the IAEA nuclides database [249].

of material backgrounds can highlight discrepancies in the detector model, hence enabling refinements to the overall simulations chain.

4.2 Energy calibration

Energy spectra provide a simple space for characterising backgrounds. Paired with positional information, it becomes possible to constrain various sources throughout different regions of the TPC. However, this critically hinges on the quality of the energy reconstruction, especially when the energy range spans several MeV.

As the LZ detector is designed for WIMP nuclear recoils with energies of $\mathcal{O}(10)$ keV, the selected dynamic range for digitisation is more suited for lower energies, despite the TPC utilising PMTs equipped with dual-gain amplifiers to read out signals in high-gain (HG) and low-gain (LG) channels [250]. This makes S2 pulses collected by the top array susceptible to saturation in both gain channels for a cluster of PMTs when exceeding energies of $\mathcal{O}(100)$ keV. One method to mitigate for this attenuation is to measure S2 pulse areas exclusively with the bottom array, which does not experience saturation in LG below 3 MeV. As such, reconstructing the energies of events using the bottom S2 signals ($\mathrm{S2c_{bot}}$) requires calibrating for a corresponding effective charge gain g_2^{bot}. The value of g_2^{bot} is inherently lower than that of g_2—by roughly a factor of 3—since S2 light is produced above the liquid surface and is hence observed mainly by the top array.

In order to measure the energy reconstruction parameters g_1 and g_2^{bot}, the light and charge yields of various mono-energetic sources were compared in a similar manner to calibrations for the LUX experiment, according to a technique first reported by Doke *et al.* [251, 252]. By re-arranging Equation 3.22, a linear relationship is formed between the light yield L_y and the charge yield Q_y:

$$L_y = -\frac{g_1}{g_2^{\mathrm{bot}}} Q_y + \frac{g_1}{W}, \tag{4.1}$$

where $L_y = \langle \mathrm{S1c} \rangle / E$ and $Q_y = \langle \mathrm{S2c_{bot}} \rangle / E$. Thus, by obtaining the mean S1c and $\mathrm{S2c_{bot}}$ for a set of sources with known energies, the energy reconstruction parameters may be extracted from the gradient and intercept of a linear fit.

Conventionally, energy calibrations are performed using dispersed internal sources such as injected $^{83\mathrm{m}}$Kr, along with several lines from various xenon isotopes that were cosmogenically activated during processing and transport. However, in order to support energy reconstruction up to several MeV, a few prominent gamma-ray peaks originating from the detector materials were also utilised – these were specifically selected as sources with minimal contamination from other decays within their proximity in energy. The set of considered peaks is summarised in Table 4.1.

Table 4.1: Mono-energetic peaks used to measure energy reconstruction parameters. Note that there is a complete overlap between two peaks at 236 keV. EC denotes electron capture. Values quoted from the IAEA nuclides database [249].

Source	Energy [keV]	Type
$^{83\mathrm{m}}$Kr	41.5	Internal conversion (32.1 keV + 9.4 keV)
$^{131\mathrm{m}}$Xe	163.9	Internal conversion
^{127}Xe	208.1	L-shell EC (5.2 keV) + γ (202.9 keV)
^{127}Xe	236.1	K-shell EC (33.2 keV) + γ (202.9 keV)
$^{129\mathrm{m}}$Xe	236.2	Internal conversion (39.6 keV + 196.6 keV)
^{127}Xe	380.2	L-shell EC (5.2 keV)+ γ (375.0 keV)
^{127}Xe	408.2	K-shell EC (33.2 keV) + γ (375.0 keV)
^{60}Co	1173.2	γ
^{60}Co	1332.2	γ
^{40}K	1460.8	γ
^{214}Bi	2204.1	γ
^{208}Tl	2614.5	γ

As illustrated in Figure 4.3, the populations associated with each source line in (S1c, S2c$_{\mathrm{bot}}$) space were fitted with two-dimensional Gaussian functions to obtain the mean S1c and S2c$_{\mathrm{bot}}$ yields, with the standard errors taken as the uncertainties. This calibration utilised the full duration of SR1, as well as $^{83\mathrm{m}}$Kr data from an injection in the fourth week of SR1. For simplicity, only SS events were considered; there was a sufficiently high level of statistics and the inclusion of MS events offered no extra information. In addition, the area threshold cuts (S1c $>$ 100 phd) and ($\log_{10}$ S2c $>$ 2.5 phd) were applied to target accidental coincidences—false pairings of uncorrelated S1s and S2s—which typically straddle the axes. In accordance

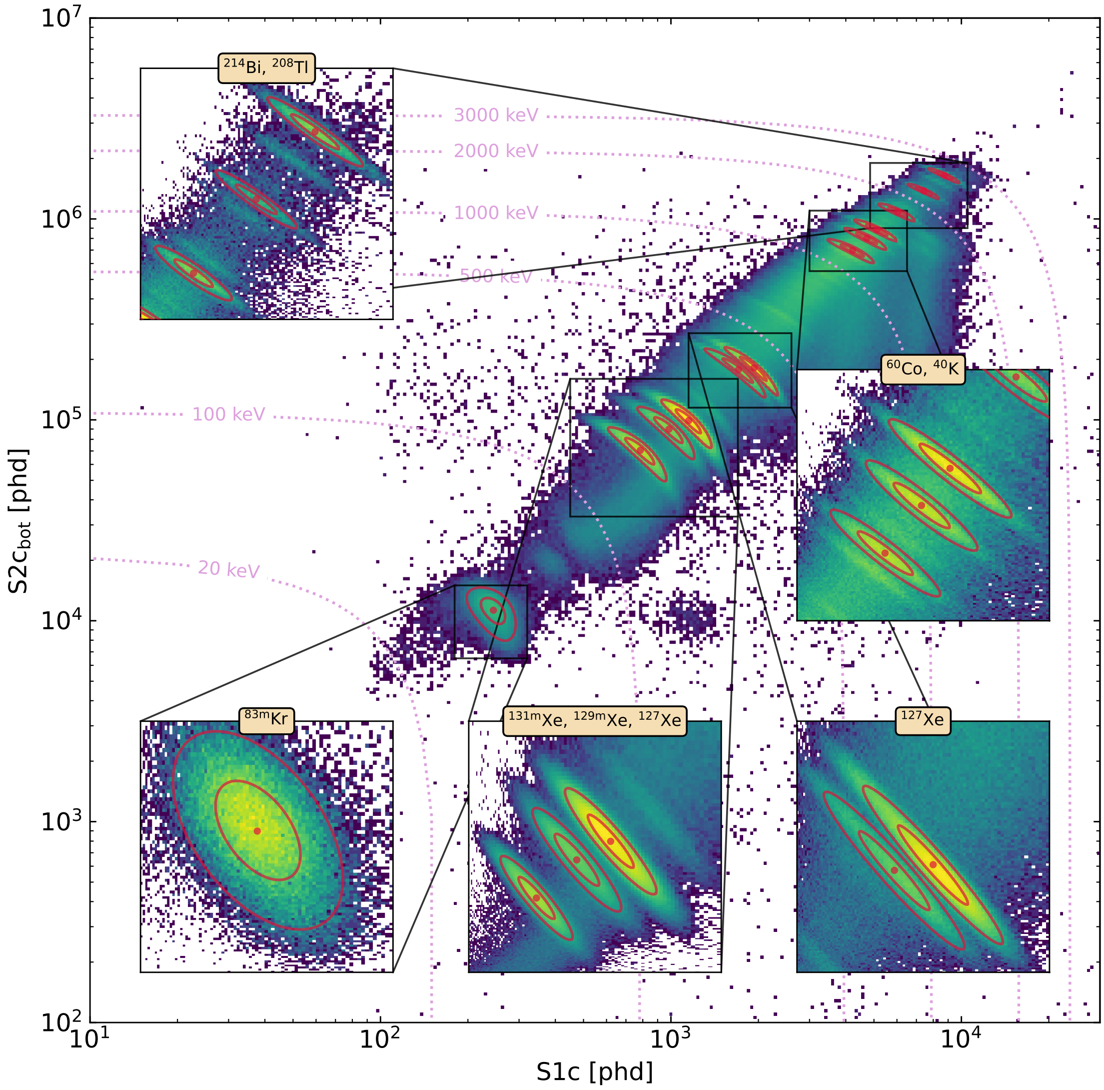

Figure 4.3: An overview of the main observable space in LZ, for SS events in SR1 data with S1c and S2c thresholds as well as drift time and radial cuts applied. Two-dimensional Gaussian fits are overlaid, with solid points marking the means along with elliptical contours for one and two standard deviations. Anti-correlation between S1c and S2c$_{\text{bot}}$ areas due to recombination fluctuations is evident by the negative slope of each population.

with the SR1 fiducial volume (FV) definition, events were restricted to drift times between 86 µs and 936.5 µs, corresponding to depths of 13.2 cm below the gate grid and 2.2 cm above the cathode grid, respectively [142]. This removes events emanating from the cathode or liquid surface, but more importantly misreconstructed scatters in the gaseous phase above the anode, which would exhibit larger S2s in the presence of a stronger field, thereby smearing populations towards the above-diagonal region in Figure 4.3. Analogously, a cut discarding events within 4 cm of the TPC edge addressed cases of charge loss to drift field non-uniformities, where the resulting reduction in S2 sizes produces events below the diagonal.

The mean light and charge yields extracted using the Doke method are plotted in Figure 4.4, with a linear fit used to obtain the following energy reconstruction parameters as per Equation 4.1:

$$g_1 = (0.106 \pm 0.001_{\text{stat}} \pm 0.001_{\text{sys}}) \text{ phd/photon},$$
$$g_2^{\text{bot}} = (14.76 \pm 0.08_{\text{stat}} \pm 0.19_{\text{sys}}) \text{ phd/electron},$$

where the systematic uncertainties were estimated by considering all permutations of point pairs to produce a range of g_1 and g_2^{bot} values, and then taking the standard errors of their distributions. In general, the line encapsulates the efficiencies in detecting light and charge quanta, whereas the position of peaks along it is set by recombination effects. Hence, the line itself is field-independent – alterations to the drift field would shift the position of each point along the line, with lower fields moving them upwards due to more frequent recombination and vice versa.

4.3 The sub-volume approach

The SR1 background simulations production consisted of 1144 components, each representing a radioisotope and detector volume pairing, ranging from bolts to cryostat vessels. However, not all assayed materials were represented in the BACCARAT detector geometry; the contributions of components that were smaller in size and mass were absorbed into nearby larger components. Nevertheless, as enabled by the extensive radioassay efforts, such a high level of granularity raises the level of complexity considerably. To complicate things further, simulated spectra for a given decay chain varied with the geometric locations of the emitting components, due to the differing trajectories prior to scattering in the xenon target. This position dependence was treated in the LUX radiogenic background measurements

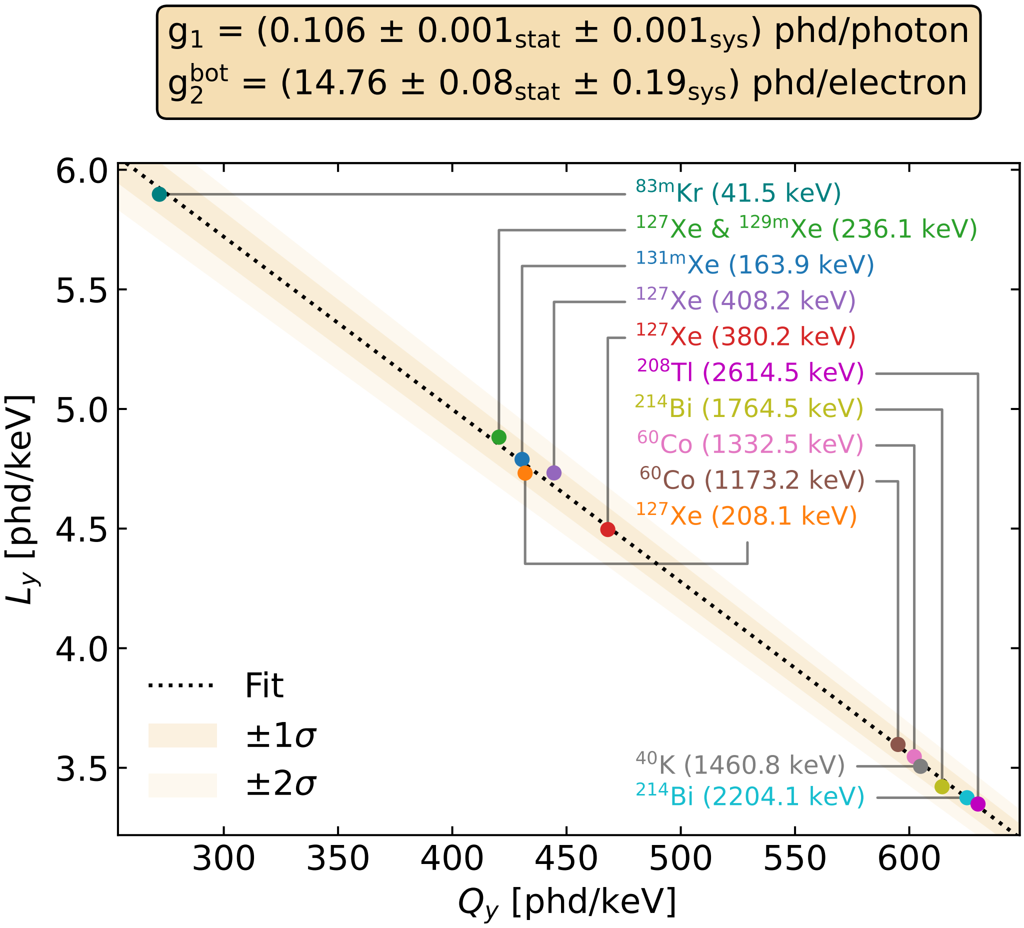

Figure 4.4: Measurement of energy reconstruction parameters with the Doke method. Error bands incorporate both statistical and systematic uncertainties.

by fitting to data after grouping components according to three regions of the detector: top, bottom, and side [253]. Rather than settle for a single global fit with coarse groups, a series of local fits within specific partitions of the active xenon volume would exploit the information provided by radioassay measurements more thoroughly.

At a minimum, four sub-volumes are necessary to appropriately capture the behaviour of backgrounds throughout the TPC:

- **central** – to characterise internal components, such as xenon activation products and beta sources, with negligible contamination from material backgrounds below 500 keV owing to plenty of self-shielding on all sides.

- lateral – to constrain contributions from radially layered components, such as the TPC and cryostat walls, field cage resistors, foam for insulation and water displacement, and OD scintillator side tanks.
- **upper** – to mainly capture backgrounds from the top array, namely the top TPC PMTs and top truss, as well as gamma rays from the surrounding cavern rock.
- **lower** – similar to the upper sub-volume; constrains contributions from the bottom TPC PMTs along with other components within their vicinity.

There are a few nuances involved with regards to the interactions between these sub-volumes. In principle, by fitting the central sub-volume first, the measured rates of internal sources can be subsequently extended to the rest of the TPC. However, this does not apply to ^{214}Pb and ^{212}Pb, which are inhomogeneously distributed, and the activation product ^{125}Xe, which does not fully mix with the bulk xenon due to its short half-life. On the other hand, there are degeneracies between the lateral and upper sub-volumes; components such as the cryostat walls and cavern gammas feature in both regions, owing in part to the reduced self-shielding provided by the gaseous phase at the top. These sub-volumes should thus be defined such that they maximise statistics and sensitivity to certain components, whilst minimising degeneracies and contributions from other regions.

The exact definitions of each sub-volume are listed in Table 4.2. These were motivated by manually inspecting the unique positional distributions of simulated components; some examples of this are shown in Figure 4.5. For instance, the lateral sub-volume was set as an annular cylinder with a radial thickness that encompasses a factor of ∼10 reduction in rate, whilst maintaining a 4 cm stand-off distance from the TPC wall to minimise the effects of charge loss on energy reconstruction and resolution. Similarly, to reduce effects resulting from non-uniformities in the fields around grid wires, the upper and lower volumes were positioned with moderate separation from the grids. In the case of the former, however, there was also a trade-off between retaining sufficient statistics whilst limiting the number of gas phase and liquid surface events. In addition, to attempt enhancing the sensitivity towards backgrounds around the rims of the TPC, such as the stainless steel grid holders, the inclusion of 'corner' volumes was also considered. These were eventually deemed unnecessary as such backgrounds were subdominant in the SR1 FV due to the introduction of corner cut-outs. The finalised sub-volumes are all visualised in Figure 4.6, superimposed on a collection of all simulated components at their nominal rates.

Table 4.2: Definitions for detector sub-volumes. The masses were estimated geometrically, given that the active liquid xenon volume between the cathode and gate grids is 7 tonnes.

Sub-volume	R limits [cm]	z limits [cm]	Mass [kg]
central	0.0–45.0	45.5–100.1	1003.0
lateral	61.8–68.8	50.0–90.0	331.7
upper	0.0–30.0	128.6–141.6	106.1
lower	0.0–30.0	2.0–15.0	106.1

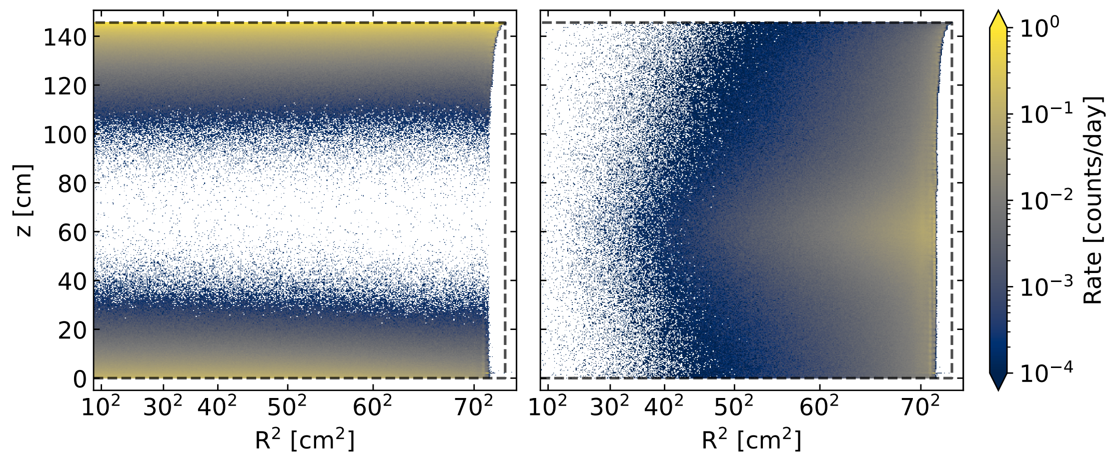

Figure 4.5: Example position distributions for simulated components, including both top and bottom array TPC PMTs on the left, and a combination of bottom OCV flange bolts and forward field cage resistors on the right. The dashed lines indicate the boundaries of the active xenon volume.

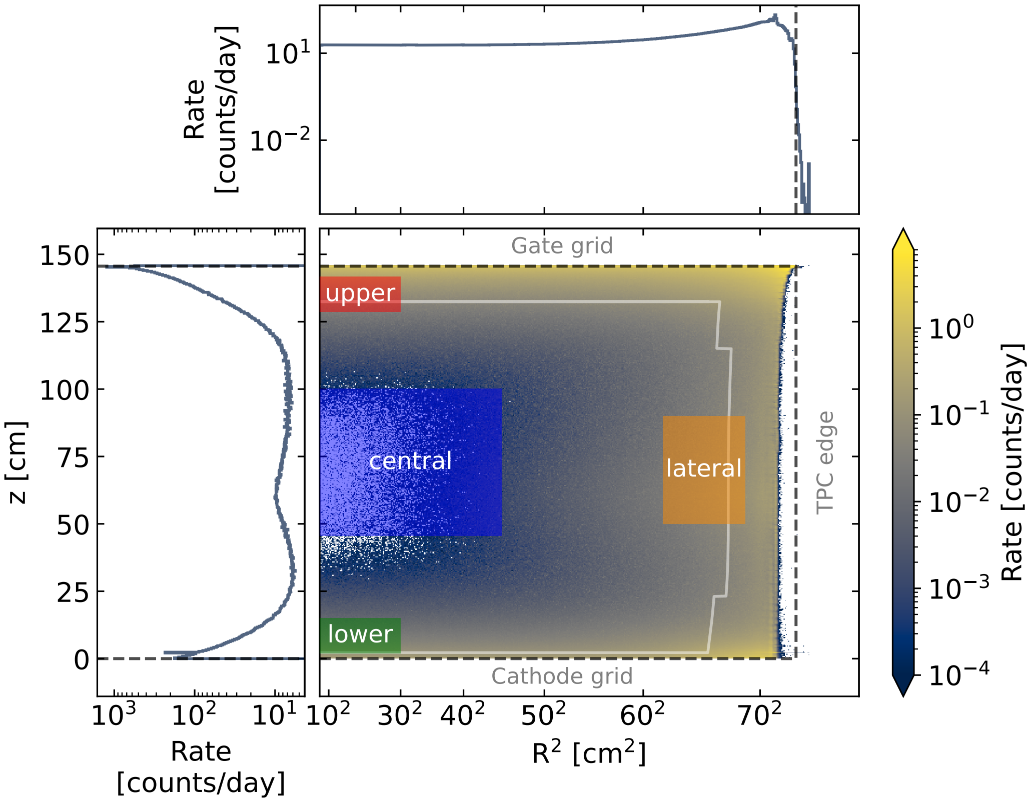

Figure 4.6: SS event positions for simulated detector components between 1–3 MeV, with nominal activity normalisations. The defined sub-volumes are overlaid as colour-coded boxes, each representing a cylinder with the exception of the annular lateral sub-volume. The SR1 FV is outlined in grey, and the boundaries of the active volume are demarked with dashed black lines. Projected histograms of R^2 and z are included for clarity.

Folding event positions into R^2 implicitly assumes azimuthal symmetry in the spatial distribution of background sources. To verify that this was the case in SR1 data, the TPC was divided into four quadrants in (x, y) space, with the z and R^2 limits set to match the sub-volume edges. As outlined in Figure 4.7, this approximation is reasonable for the most part. The main deviation was observed at the 889.3 keV gamma peak associated with ^{46}Sc, a product of the activation of titanium in the cryostats with a half-life of 83.8 days. The discrepancy is consistent with additional activation from neutron calibrations; the neutron source tube is located at 9 o'clock in (x, y), hence the elevated ^{46}Sc rates in quadrants 1 and 3. This is most straightforwardly overcome by setting a lower energy limit of 1 MeV in the fitting process.

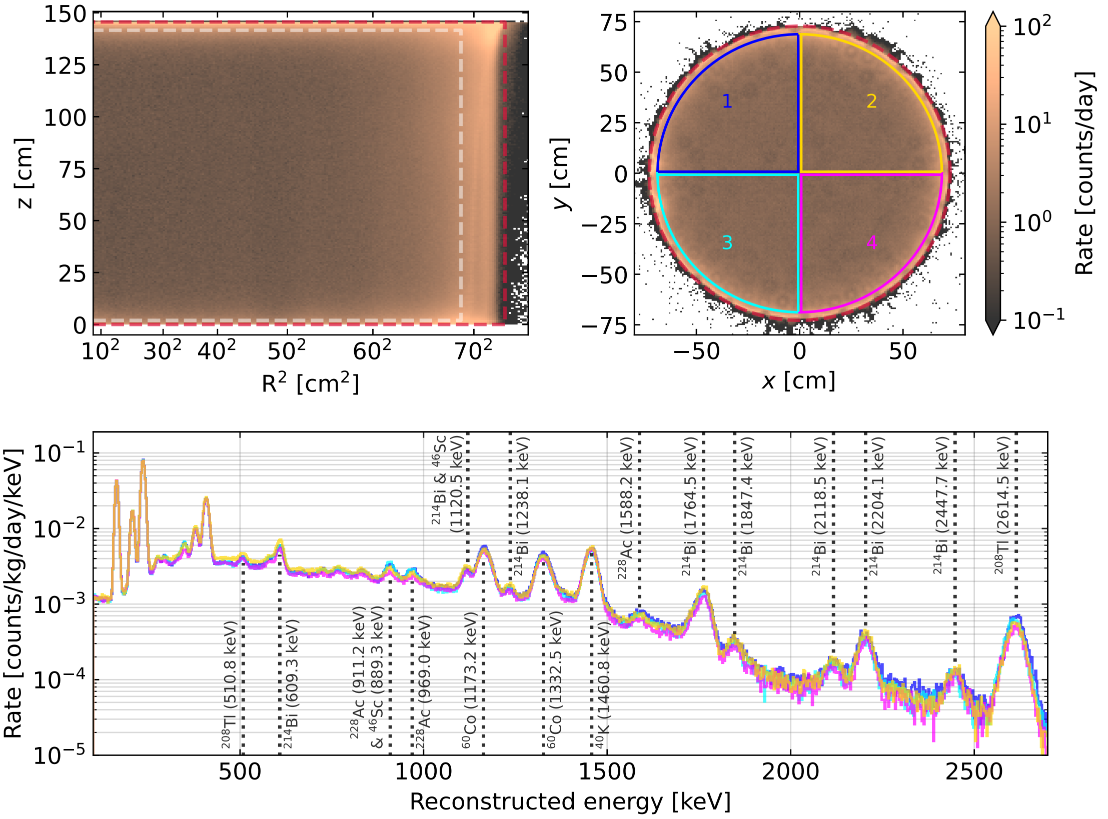

Figure 4.7: Inspection of the azimuthal symmetry of background rates in the TPC. The positions of SS events are shown in (R^2, z) space on the top left, with a grey dashed border to indicate the boundaries corresponding to the quadrants in the (x, y) plot on the top right. The active volume edges are marked in both of the top plots by dashed red lines. The energy spectra for each quadrant are presented in the bottom histogram, with prominent gamma-ray lines above 500 keV labelled using values quoted from the IAEA nuclides database [249]. Energies are restricted to the 0.1–2.7 MeV range for all plots.

4.4 Spectral corrections

In fits to data, energy spectra of simulated components are essentially treated as templates for determining the substructure of the observed spectrum. The fitting process is thus inherently sensitive to minor mismodelling and misreconstruction effects, which influence the shapes and features of the spectra. The following sections address some of these effects with the goal of optimising the compatibility between simulations and data, which ultimately improves the overall quality and robustness of the fitting process.

4.4.1 Peak mean corrections

With the calibrated values of g_1 and g_2^{bot}, the positions of reconstructed peaks agree with their expected values to within ±0.8%. However, this residual offset presents as a systematic shift, which becomes visibly apparent for high-energy peaks. Moreover, the extent of the shift appears to be position dependent, hinting towards subtle biases in the pulse area corrections.

To quantify this, the peak means were estimated for both simulations and data by fitting each prominent peak with a Gaussian plus a linear background. Inspecting the ratios of these means as a function of energy revealed a linear relationship, as demonstrated for each of the four sub-volumes in Figure 4.8. The correct energy E' can then be inferred by applying a linear fit and utilising the coefficients as per

$$E' = \frac{cE}{1 - mE}, \tag{4.2}$$

which improves the level of agreement to within ±0.2%. In the case of the SR1 FV, a discontinuity in the 0.5–1.0 MeV range meant that a linear fit was insufficient. To adequately cover the full energy range, a smoothed linear spline fit was used to inform the offset correction, as displayed on the left of Figure 4.9.

There are a few plausible explanations as to the origin of this systematic effect. It is possible that the Doke method is only effective as a first-order calibration, and that attempting to reconcile low and high energy regimes whilst maintaining reliable energy reconstruction is not straightforward. More specifically, the systematic uncertainty ranges for g_1 and g_2^{bot} allow for a ±1.1% shift in the peak means, which could account for the offsets entirely. On the other hand, this could be partly attributed to the inhomogenous flow conditions observed during SR1, depicted on the right of Figure 4.9. The lower half of the TPC experienced reduced rates of events from radon daughters, since the liquid xenon mixing timescale was longer than their half-lives. This may introduce a slight bias to finite electron lifetime corrections for S2 areas when using a position-averaged value; higher purity towards the bottom translates into an overcompensation to the energy, and vice versa.

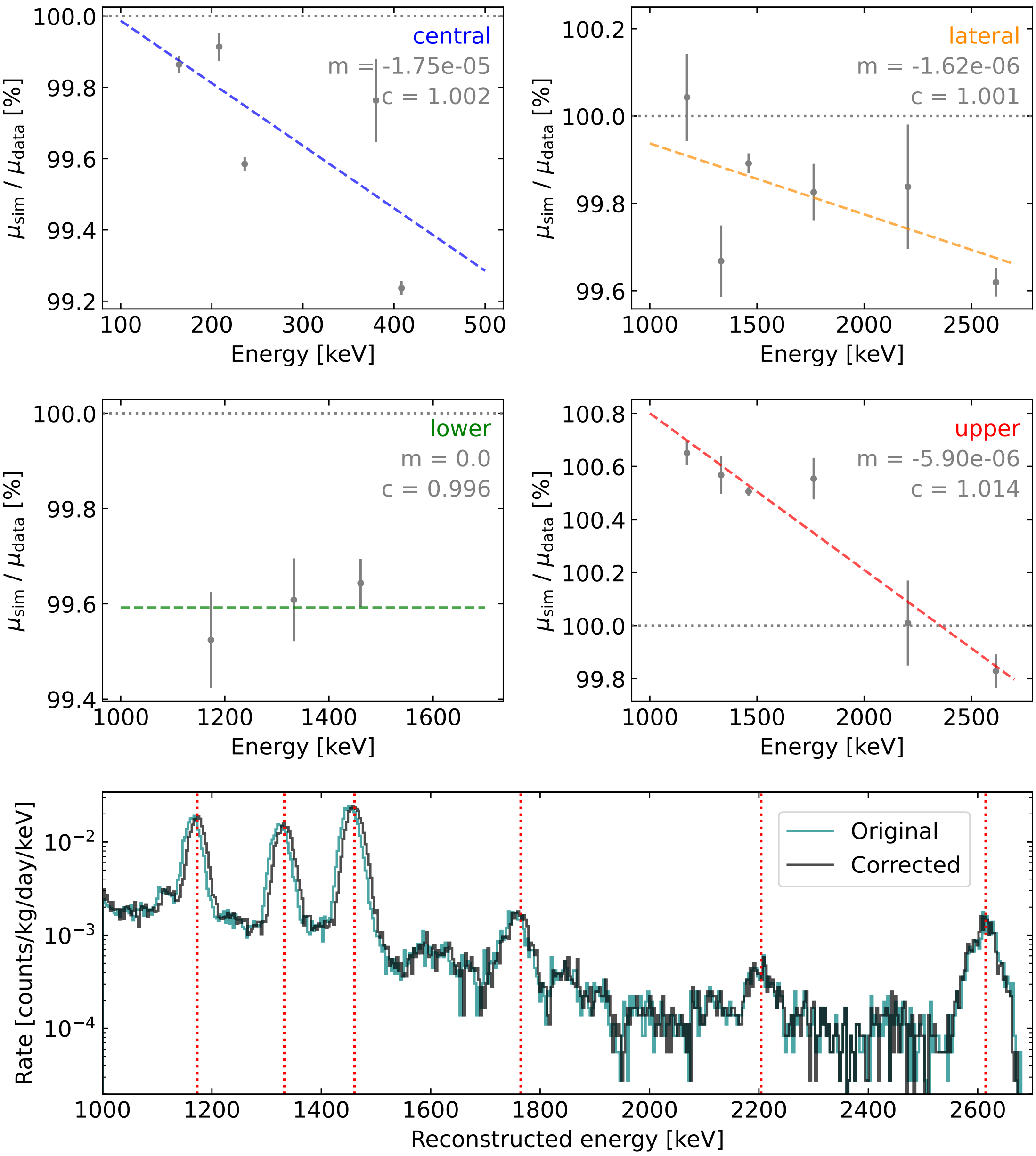

Figure 4.8: Fitted energy deviation lines for all four sub-volumes, each within their locally considered energy range. The bottom panel showcases the effect of the correction in the case of the upper sub-volume as an example, with expected peak positions indicated by vertical dotted lines. Due to a low number of events above 1.7 MeV in the lower sub-volume, the correction was approximated by a flat average of the ^{60}Co and ^{40}K points.

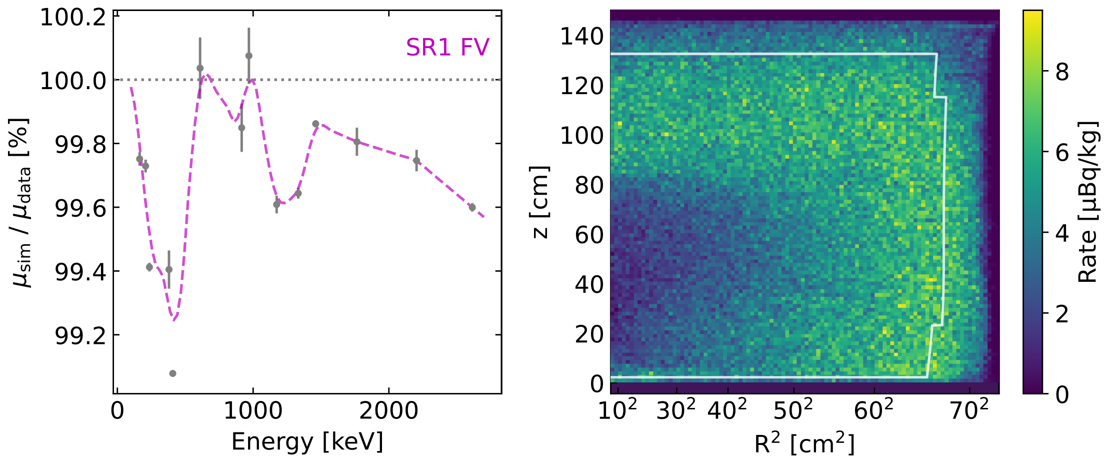

Figure 4.9: Peak energy deviations for the SR1 FV, fitted with a smoothed linear spline in the 0.1–2.7 MeV range (left); positional distribution of ^{218}Po events as reported in [248], illustrating non-uniform mixing in the lower half of the TPC, with the SR1 FV contour in white (right).

4.4.2 Peak resolution matching

In order to fulfil the high statistics requirements, the SR1 background simulations were generated using the fast parametric chain. This delivers large-scale datasets with greater computational efficiency by compromising on the level of detail; optical tracking is replaced with implementations using detector-averaged quantities to compute signal sizes and event positions. Consequently, some detector effects and intricacies are left unaccounted for. This can manifest in energy space as a divergence between the simulated and observed energy resolution, which is dictated by various effects such as recombination fluctuations and detector purity. Whereas the previous section focused on optimising the alignment of measured peak means with their expected positions, this section is concerned with ensuring that the simulated peak widths are comparable to those in data.

The energy resolution, defined as the ratio of a peak's width σ to its mean, is commonly parametrised in terms of a phenomenological function:

$$\left(\frac{\sigma}{E}\right) = \frac{a}{\sqrt{E}} + b, \tag{4.3}$$

where a and b are empirically determined using the means and widths from Gaussian fits to a set of mono-energetic peaks. The peak width as a function of energy can therefore be explicitly modelled as

$$\sigma = a\sqrt{E} + bE. \tag{4.4}$$

The relationship between σ and $\sqrt{E}$ for both data and simulations is shown in Figure 4.10 (a), where the width information was taken from the same Gaussian fits as in Section 4.4.1. As illustrated by fits in the form of the width relation in Equation 4.4, peaks in simulated spectra are generally narrower and hence better resolved than in data. In the absence of a tuned smearing model at the simulation stage, this can affect the quality of spectral fits.

To compensate for this, the energy in every simulated event was re-scaled according to a random factor, sampled from a Gaussian distribution with a mean of 1 and an energy-dependent smearing width $\sigma_s(E)$. To derive the form of $\sigma_s(E)$, each simulated peak was smeared using trial values of σ_s, with the subsequent increases in width $\Delta\sigma$ producing a profile as demonstrated in Figure 4.10 (b). Given this is a stochastic process, each trial value was repeated a number of times, and the overall profile was approximated by a quadratic polynomial fit. The ideal value of σ_s for each peak was then inferred from the profile, such that the resulting $\Delta\sigma$ matches the difference between the two width relations at the corresponding energy of the peak. This ultimately produces the form of $\sigma_s(E)$ in Figure 4.10 (c), which is well described by an exponential curve. In this case, only peaks with pronounced differences in width were selected to remain consistent with the width relations in Figure 4.10 (a).

The energy resolution curves in the form of Equation 4.3 are shown in Figure 4.10 (d), for both data and simulations. The application of smearing to simulated spectra, according to the method outlined above, leads to a close match in peak widths with respect to data.

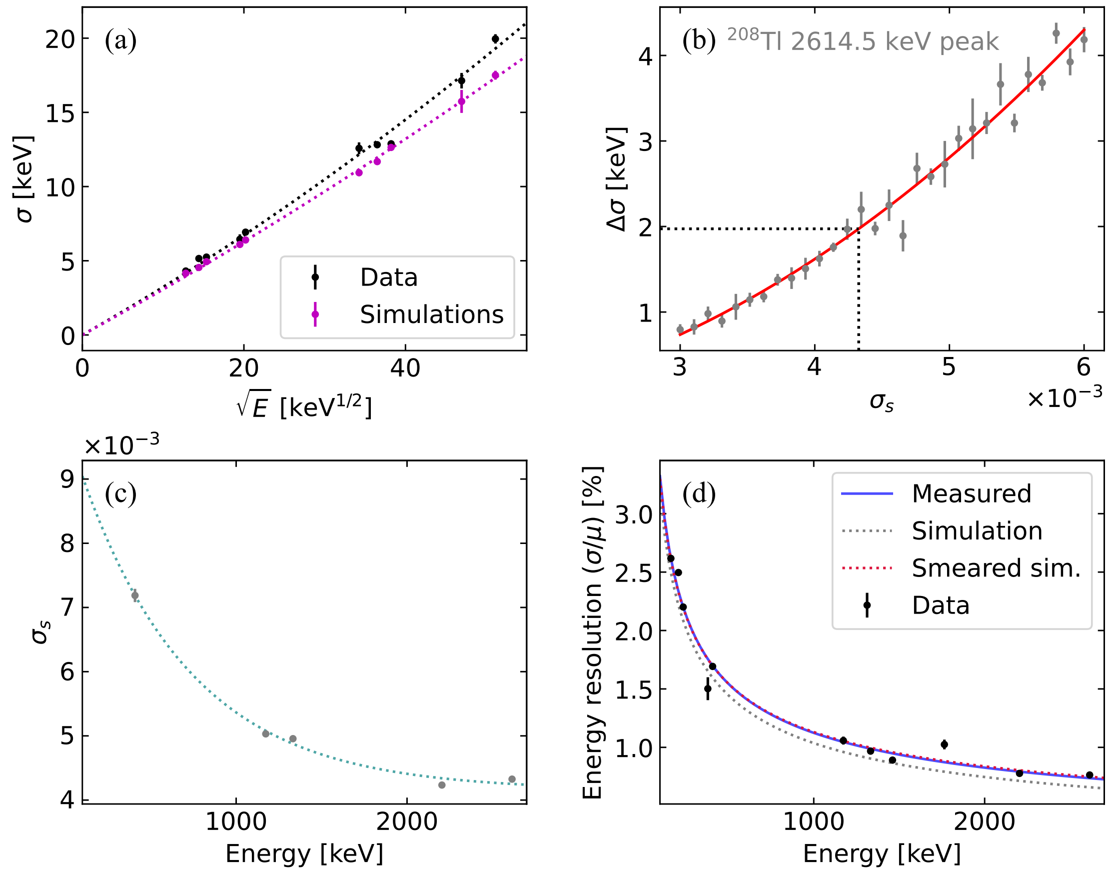

Figure 4.10: An overview of the smearing procedure implemented for simulated energy spectra. (a) Peak width relations with energy for simulations and data. (b) An example profile of changes in peak width with different trial values of the Gaussian smearing width σ_s, for the 2614.5 keV ^{208}Tl peak. Each data point is an average of 5 repeated tests, with the standard errors taken as the uncertainties. The dotted line marks the optimal value of σ_s to reproduce the width observed in data. (c) The energy dependence of σ_s modelled by an exponential decay, where each point is provided by a profile for the corresponding peak, as in (b). (d) Energy resolution curves showcasing a close overlap between smeared simulations and data. Coefficients a and b are measured in data as 0.321 keV$^{1/2}$ and 0.001, respectively.

4.5 Component grouping

Utilising the sub-volume approach was the first step towards simplifying the model fitting process down from over a thousand components. Apart from the central sub-volume, where the components considered were manually selected internal backgrounds, each component of a given source was assigned to a sub-volume based on where it contributed the highest mass-normalised rate. As illustrated by the breakdown of component fractions for each non-central sub-volume in Figure 4.11, this already downsizes the number of parameters in a given fit by roughly a factor of 3.

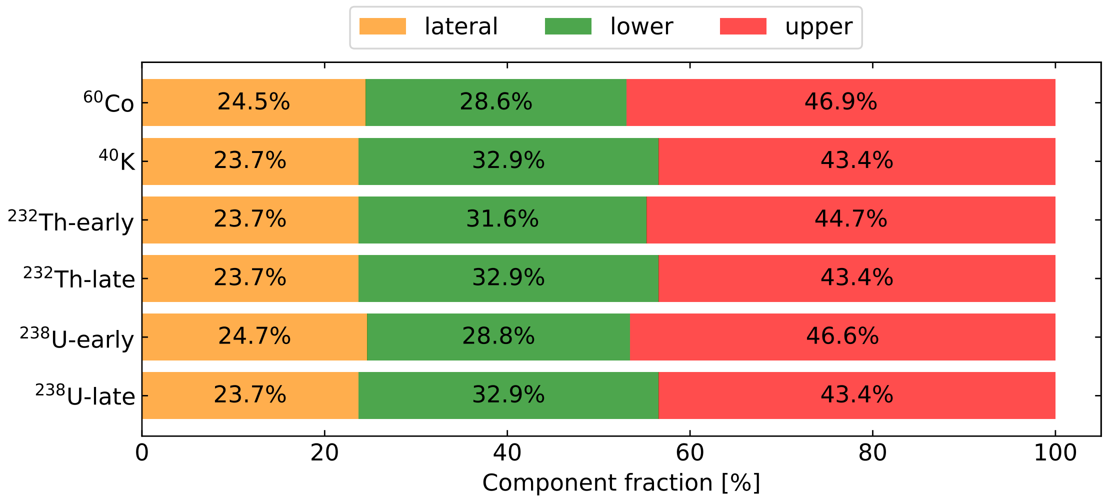

Figure 4.11: Percentage of components assigned to each sub-volume, for each source. Internal backgrounds are omitted as they are all floated in the central sub-volume. Cavern wall contributions are also excluded as they are allowed to vary in both the lateral and upper sub-volumes.

As mentioned in Section 4.3, the vast range of gamma-ray trajectories within the detector geometry produced variations in spectra for any given source. To tackle the complexities posed by this, components were grouped together and associated with a single common parameter at the fitting stage if their spectra were judged to be sufficiently similar in shape. The level of similarity between each pair of spectra was quantified with a two-sample Kolmogorov-Smirnov (KS) test [254, 255]. This test compares two empirical cumulative distribution functions (eCDFs), and defines the test statistic $D_{n,m}$ as a measure of the maximum distance between them:

$$D_{n,m} = \sup_x |F_n(x) - F_m(x)| \,, \tag{4.5}$$

where each sample eCDF $F(x)$ was obtained by approximating a normalised spectrum as a PDF, and sup denotes the supremum function. The value of $D_{n,m}$ therefore represents the degree of incompatibility between two spectral shapes, and takes on values in the interval $[0, 1]$ by definition. As showcased by an example map of $D_{n,m}$ values in Figure 4.12, this metric successfully recreates intuitive groupings.

For instance, ^{40}K sources from the bottom TPC array PMTs, nearby sensors, and the titanium plate they are mounted to, were all consolidated.

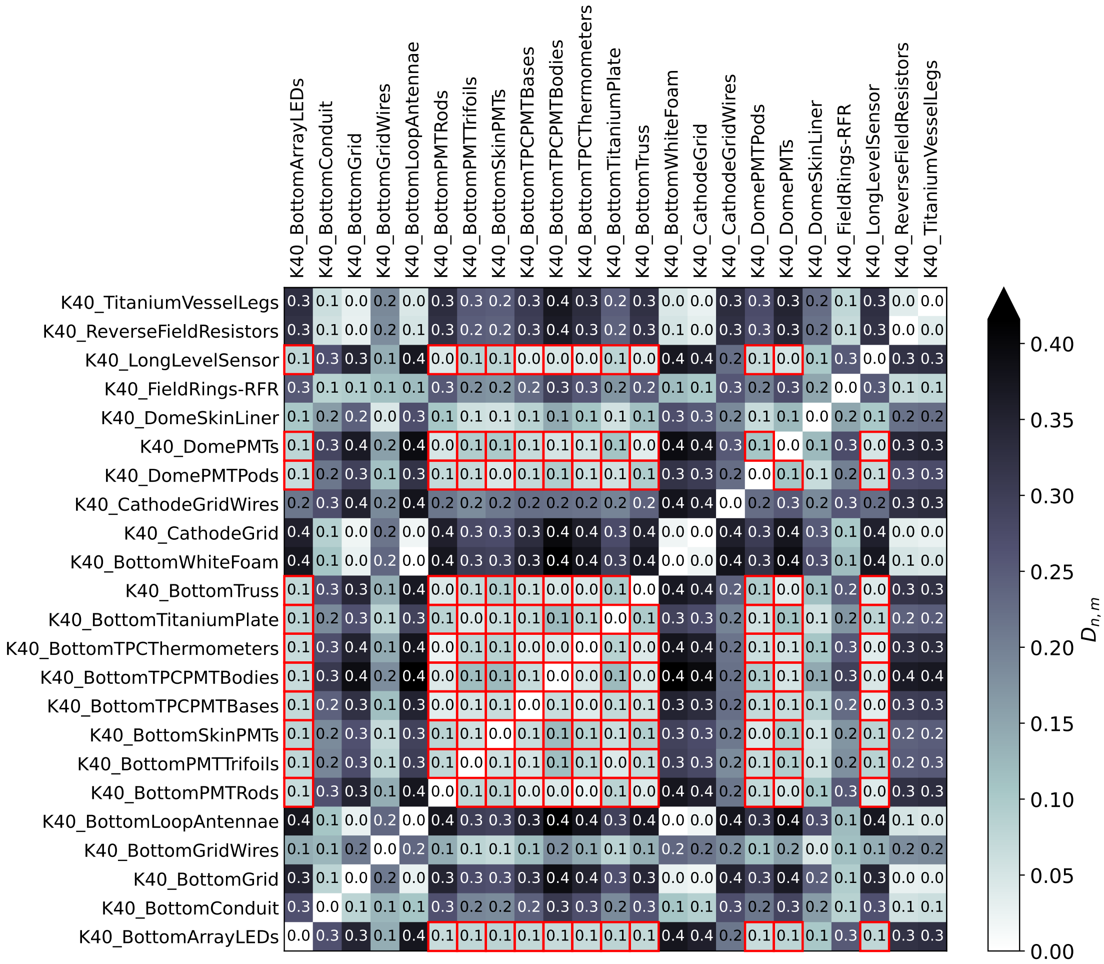

Figure 4.12: Example map of KS test statistics $D_{n,m}$ for all combinations of ^{40}K components assigned to the lower sub-volume. The tile brightness corresponds to the level of compatibility between two spectra, and red outlines indicate cases where components pass the grouping criteria.

Another aspect to note is that, for a given source and sub-volume, a significant portion of the rate is typically dominated by a handful of components. For example, 83.4% of ^{40}K events in the lower sub-volume originate from the bottom TPC PMT bodies, whereas this is 91.1% in an equivalent case for ^{60}Co. This motivates the application of a proportion threshold, such that components are only considered if they contribute a non-negligible amount towards the rates of a source in a certain sub-volume. Such a threshold was set based on the corresponding number of groups, which translates directly into the number of fit parameters. As informed by the behaviour displayed in Figure 4.13, a threshold of 10% was selected as the point at which the number of groups drops by approximately one order of magnitude. In the same vein, a strict threshold of 0.1 was set for $D_{n,m}$ to retain some flexibility in the available range of spectral shapes.

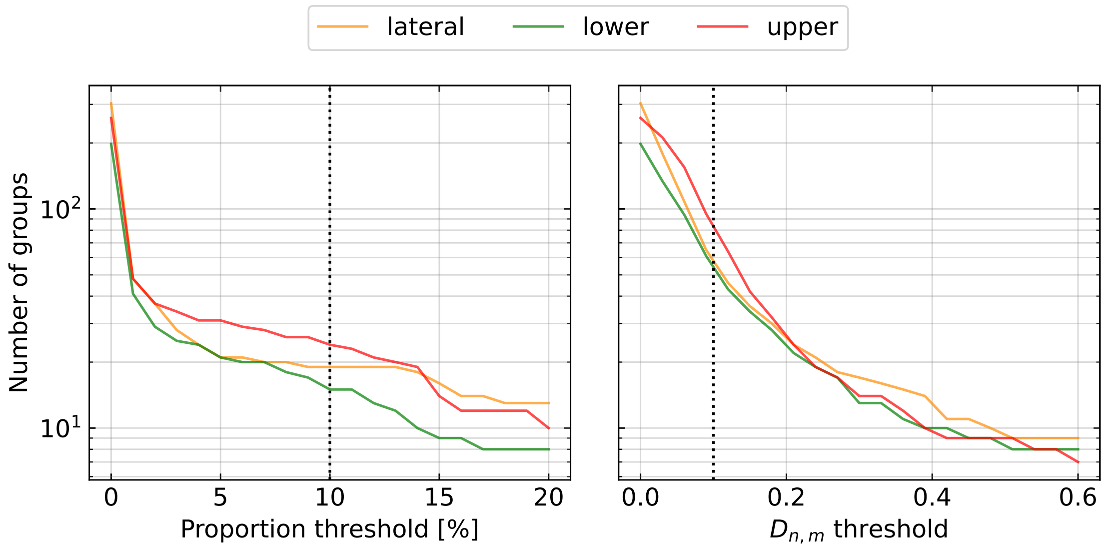

Figure 4.13: Number of groups as a function of component proportion threshold (left) and KS test statistic threshold (right). The dotted black vertical lines indicate where each threshold was set. To avoid bias, the other threshold was set to zero for each plot.

For subdominant components that fail to pass the proportion threshold, there are three main options for how to proceed: they could be *appended* to the least conflicting group (with lowest $D_{n,m}$), summed together and *floated* as a unique group, or *fixed* altogether. Since such components are under-represented, it is inherently because there is a lack of sensitivity towards them in any of the defined sub-volumes. Continuing with the lower sub-volume example, this applies to PMTs in the skin and the stainless steel grid holders near the rims of the TPC. Therefore, it was deemed best to fix subdominant components at their initial estimates from assay measurements.

Within each non-central sub-volume, components of a given source were sorted by rate in descending order and grouped according to the algorithm outlined in Figure

4.14. For each component in a set, $D_{n,m}$ is evaluated with respect to the summed spectrum of every pre-existing group. The component is added to the group with which it achieves the lowest $D_{n,m}$, if its value lies below the 0.1 threshold. A new group is created if a component is not compatible with any existing groups but passes the event proportion threshold. Otherwise, the component is fixed if none of these conditions are satisfied. In this process, the spectral shape takes precedence over the event proportion; a subdominant component was still considered if its shape was indistinguishable from others in a group.

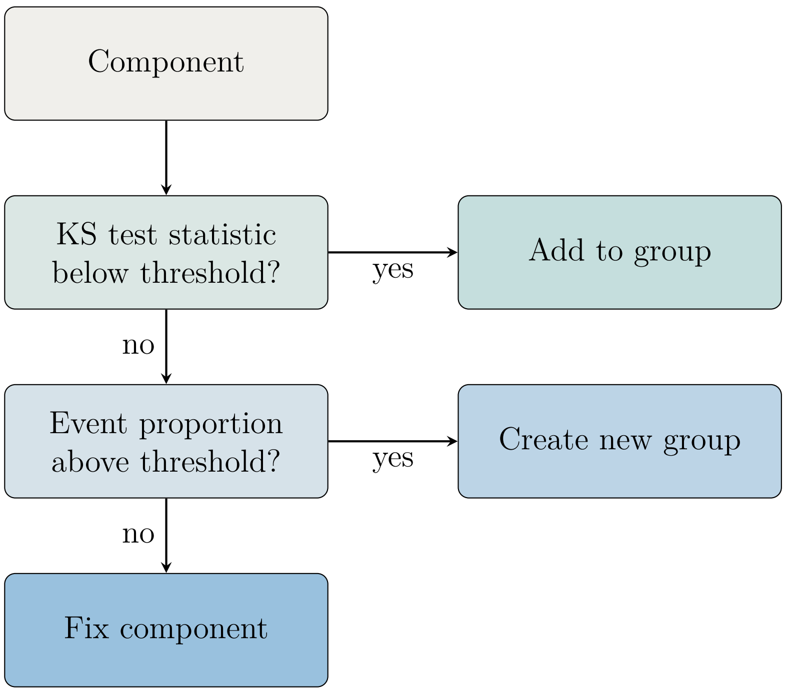

Figure 4.14: Diagram of the logic used to group to components of a given source, for an assigned sub-volume. This is applied to a series of components sorted by their relative event proportions in descending order.

Out of 1144 simulated components, 644 (56.3%) consisted of neutron sources, namely (α, n) reactions of thorium and uranium, whereby alpha particles generate neutrons by interacting with the surrounding detector materials, as well as spontaneous fission of uranium. These were excluded from the fits altogether since their contribution as a fraction of the total expected background in the 0.1–2.7 MeV range is $\mathcal{O}(10^{-7})$. Discounting internal backgrounds and sources with zero deposits in the TPC, this leaves a total of 426 detector ER components under consideration.

Applying the grouping algorithm in tandem with the sub-volume approach reduces this down to 32 components; a detailed breakdown of this is listed in Table 4.3.

Table 4.3: Summary of the number of groups N_g as a fraction of the number of initial components N_c, for each detector ER source and non-central sub-volume.

Source	Lateral N_g/N_c	Lower N_g/N_c	Upper N_g/N_c	Total N_g/N_c
^{60}Co	2/12 (16.7%)	1/14 (7.1%)	2/23 (8.7%)	5/49 (10.2%)
^{40}K	1/18 (5.6%)	1/25 (4.0%)	2/33 (6.1%)	4/76 (5.3%)
^{232}Th-early	2/18 (11.1%)	1/24 (4.2%)	2/34 (5.9%)	5/76 (6.6%)
^{232}Th-late	3/18 (16.7%)	2/25 (8.0%)	3/33 (9.1%)	8/76 (10.5%)
^{238}U-early	2/18 (11.1%)	2/21 (9.5%)	1/34 (2.9%)	5/73 (6.8%)
^{238}U-late	3/18 (16.7%)	1/25 (4.0%)	1/33 (3.0%)	5/76 (6.6%)
All sources	13/102 (12.7%)	8/134 (6.0%)	11/190 (5.8%)	32/426 (7.7%)

To highlight the differences in spectral shapes captured by the KS tests, the set of ^{60}Co group spectra are illustrated in Figure 4.15 as an example. The most apparent variation of spectra within a region of the detector is in the relative heights between the photopeaks and the Compton continuum, which are related by the mean free path of the gamma rays. Moreover, the effects of MSSI events become evident for spectra in the lower sub-volume. These are cases where MS events occurring within the vicinity of the cathode produce only one detectable S2, due to loss of ionisation signals to the RFR, hence appearing as SS events. In the case of ^{60}Co, the spectrum extends beyond the second photopeak as one of the two characteristic gamma rays deposits energy in the RFR, producing a broad two-peak structure near the tail.

4.6 Fit procedure

As discussed in Section 4.3, the options for constraining the rates of numerous detector components typically entail a complicated fit involving many parameters, or coarse manual grouping as was done for the LUX experiment. In order to effectively leverage both the highly granular simulations production and extensive assay measurements, whilst limiting the level of complexity, a new procedure was designed

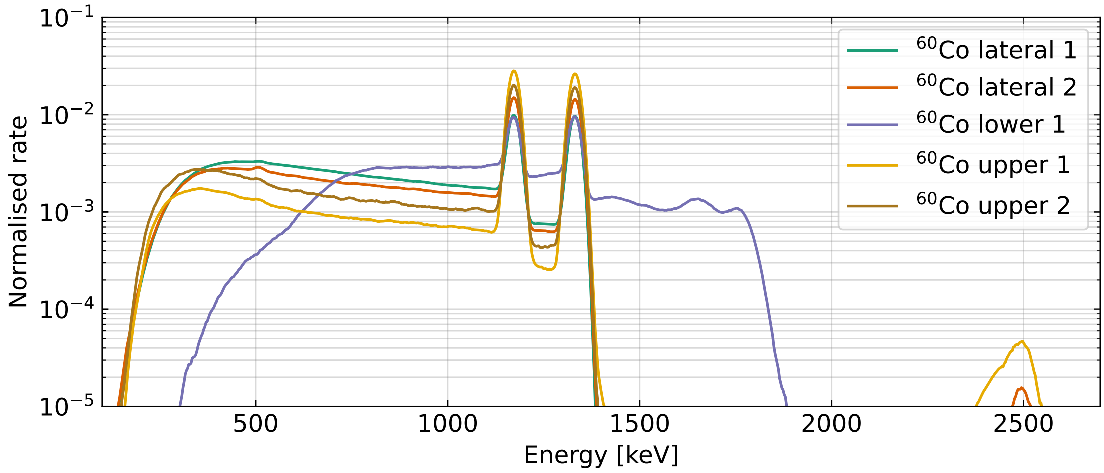

Figure 4.15: Normalised ^{60}Co group spectra for all non-central sub-volumes. The numbering scheme included in the legend is used to distinguish between different groups within the same sub-volume.

for the SR1 detector background model. In essence, this consisted of constraining a region-specific subset of components at a time by fitting simulated energy spectra to data within a sequence of detector sub-volumes. The consolidated fit parameters and errors ultimately formed the initial values and constraints for a final fit in the SR1 FV.

4.6.1 The likelihood function

Due to the large sample sizes involved, a binned maximum likelihood approach was adopted; executed with the `iminuit` package, a Python implementation of Minuit [256, 257]. For a measured energy spectrum with N_b bins, the number of entries in each bin is treated as an independent Poisson random variable, with the probability of observing d_i counts in the ith bin expressed as

$$P(d_i|\boldsymbol{\theta}) = \frac{f_i(\boldsymbol{\theta})^{d_i}}{d_i!}e^{-f_i(\boldsymbol{\theta})}, \tag{4.6}$$

where $f_i(\boldsymbol{\theta})$ represents the expected number of counts in the ith bin as a function of the model parameters $\boldsymbol{\theta}$, and is obtained by summing over N_c component or group spectra:

$$f_i(\boldsymbol{\theta}) = \sum_{j=1}^{N_c} \theta_j p_{ji}, \tag{4.7}$$

with the ith bin of the jth component PDF in energy denoted by p_{ji}, and scaled to a specific number of counts by the corresponding θ_j. The joint PDF for all observed counts, which forms the core term of the likelihood function, is hence the product of independent $P(d_i|\boldsymbol{\theta})$ over N_b bins.

The initial counts $\boldsymbol{\mu}$ and their uncertainties $\boldsymbol{\sigma}$ for each component in a given fit were informed by *in situ* sideband analyses and radioassay measurements, with a conservative $\pm 50\%$ initial uncertainty assumed for the detector components. In principle, the fitted model parameters $\hat{\boldsymbol{\theta}}$ should not deviate significantly from $\boldsymbol{\mu}$. To account for this, a Gaussian constraint term $\mathcal{N}(\theta_k|\mu_k, \sigma_k)$ was assigned to each component to regulate their range of variability. The likelihood function was thus constructed with the form

$$\mathcal{L}(\boldsymbol{d}|\boldsymbol{\theta}, \boldsymbol{\mu}, \boldsymbol{\sigma}) = \prod_{i=1}^{N_b} P(d_i|\boldsymbol{\theta}) \times \prod_{k=1}^{N_c} \mathcal{N}(\theta_k|\mu_k, \sigma_k). \tag{4.8}$$

Taking the logarithm and dropping terms that do not depend on $\boldsymbol{\theta}$ therefore produces the expression below:

$$\begin{aligned} \ln \mathcal{L}(\boldsymbol{d}|\boldsymbol{\theta}, \boldsymbol{\mu}, \boldsymbol{\sigma}) = & \sum_{i=1}^{N_b} d_i \ln \left(\sum_{j=1}^{N_c} \theta_j p_{ji} \right) && \text{(model term)} \\ & - \nu(\boldsymbol{\theta}) && \text{(extended term)} \\ & - \sum_{k=1}^{N_c} \frac{1}{2} \left(\frac{\theta_k - \mu_k}{\sigma_k} \right)^2 && \text{(Gaussian constraint term)} \end{aligned} \tag{4.9}$$

where the extended Poisson term $\nu(\boldsymbol{\theta}) = \sum_{i=1}^{N_b} f_i(\boldsymbol{\theta})$ effectively incorporates the observed sample size $n = \sum_{i=1}^{N_b} d_i$ as part of the measurement. This has the effect of reducing the variances of the maximum likelihood estimators $\hat{\boldsymbol{\theta}}$ by exploiting information from n [258, 259]. To evaluate the goodness-of-fit, the χ^2_λ statistic was used:

$$\chi^2_\lambda = 2 \sum_{i=1}^{N_b} \left(d_i \ln \frac{d_i}{f_i(\hat{\boldsymbol{\theta}})} + f_i(\hat{\boldsymbol{\theta}}) - d_i \right), \tag{4.10}$$

which follows a χ^2 distribution with $N_b - N_c$ degrees of freedom for Poisson-distributed histograms. This form originates from the definition of a likelihood ratio $\lambda = \mathcal{L}_\mathrm{p}(\boldsymbol{d}|\boldsymbol{y})/\mathcal{L}_\mathrm{p}(\boldsymbol{d}|\boldsymbol{d})$ and taking $\chi^2_\lambda = -2 \ln \lambda$ for a Poissonian likelihood function $\mathcal{L}_\mathrm{p}$ [259, 260].

4.6.2 Fit sequence

The sub-volume fits were conducted in the following order:

$$\textbf{central} \longrightarrow \textbf{lateral} \longrightarrow \textbf{lower} \longrightarrow \textbf{upper},$$

with components and groups fixed at their best-fit values before proceeding to the next step. The sequence was initiated with the central sub-volume fit since internal backgrounds pervade the whole TPC and hence contribute to the other volumes. To eliminate contributions from internals aside from ^{136}Xe $2\nu\beta\beta$ decay, whilst capturing the 2614.5 keV ^{208}Tl gamma-ray photopeak, the energy range for non-central sub-volume fits spanned 1–2.7 MeV. In general, the activity of most components was confined to the vicinity of their assigned sub-volume, which implies that the series of fits beyond the first step is agnostic to the sub-volume ordering. The main exceptions to this were sources from the cryostat and cavern gamma rays, which irradiate a broad region of the TPC and hence form a degeneracy between the lateral and upper sub-volumes. In these cases, normalisations were constrained using the initial fit result and allowed to re-float in a subsequent fit.

Following the series of fits, all detector components for a given source were consolidated within their respective sub-volumes to form side, bottom, and top groups to be fitted in the SR1 FV, with internal backgrounds characterised in the central sub-volume remaining fixed. These groups include both floated components, which have been re-scaled according to the sub-volume fit results, and previously fixed components at their nominal values. In addition, the combined parameter errors, which `iminuit` returns within a covariance matrix determined from a numerically estimated inverse Hessian, were used to set $\boldsymbol{\sigma}$ in the Gaussian constraint terms for the SR1 FV fit [261]. The lower energy bound of the SR1 FV fit was relaxed to 80 keV to capture the rising edges of several components, without impinging on the energy range of other ongoing searches. For reference, the number of parameters and energy range for each fit are summarised in Table 4.4.

Table 4.4: Summary of fit information, in chronological order. The SR1 FV fit involved the most parameters as it featured three groups for each non-internal source (top, bottom, side), plus two cavern gamma ray components and ^{136}Xe.

Fit volume	Fit range [MeV]	Number of parameters
central	0.1–0.5	9
lateral	1.0–2.7	15
lower	1.0–2.7	8
upper	1.0–2.7	12
SR1 FV	0.08–2.7	21

4.6.3 Single-scatter cut efficiencies

For simplicity, all fits were performed for SS events. This implicitly assumes that the ratio of SS to MS events is accurately modelled in simulations. In particular, this ratio depends on the mean free path of photons and hence the energy, as well as the separability of S2 pulses in z, which varies as longer drift times translate into wider S2s with more overlap. The number of SS events as a fraction of SS+MS with energy is compared between simulations and data in Figure 4.16, over the SR1 FV fit energy range. As the two are in agreement to within ±8.5% on average, this demonstrates that mismatches in the SS ratio are unlikely to be a significant source of discrepancy.

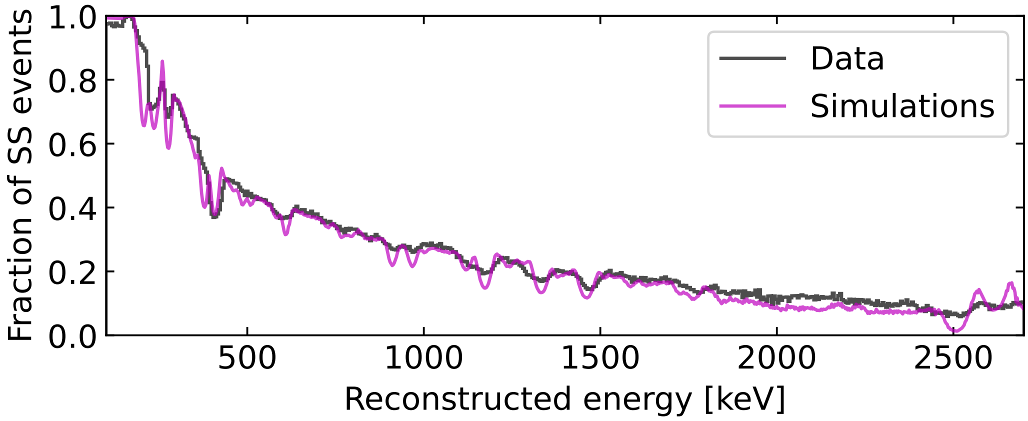

Figure 4.16: SS cut efficiencies SS/(SS+MS) for simulations and data. Improvements to the position resolution are expected to shift the curve downwards, as neighbouring vertices in MS events consequently become more separable.

4.7 Results and discussion

All four sub-volume fits are presented in Figure 4.17, with groups combined by source for clarity. In general, it is visually evident that the priors informed by radioassay measurements are a reasonable first estimate, with most discrepancies attributed to a couple of groups or components. Moreover, the reduced χ^2_λ values for the non-central sub-volumes are indicative of high-quality fits. In the case of the central sub-volume, the slightly elevated χ^2_λ is attributed to slight mismodelling of the ^{127}Xe peaks, where mismatches in relative peak heights are apparent in the residuals plot.

For interpretability, an effective scaling factor was calculated for each group as the ratio of the fitted counts to the initial estimate; these are visualised for the sub-volume fit results in Figure 4.18. Overall, the majority of scaling factors are consistent with a value of 1, which supports the reliability of radioassay measurements. In other cases, such as between the two ^{232}Th-early upper groups, there are opposing scalings that average to approximately 1. A number of interesting observations can be drawn from Figure 4.18:

- **Increased ^{60}Co in the bottom array** – when assayed between August 2016 and February 2017, the mass-weighted activity of a TPC PMT was at (1.90 ± 0.19) mBq on average. However, a subset of PMTs were unintentionally exposed to DD and ^{252}Cf neutron sources during storage, and consequently exhibited elevated ^{60}Co rates. To minimise their impact, these activated PMTs were strategically placed around the outer edge of the bottom array to exploit the additional self-shielding from the RFR. Factoring for the 5.27 year half-life of ^{60}Co, the total expected activity of the bottom array PMTs is (237.23 ± 23.72) mBq without activation, and (739.10 ± 73.90) mBq with activation. This produces an expected scaling of (3.12 ± 0.44), which manifests in the lower sub-volume fit as an increase in the bottom TPC PMT components by a factor of (2.70 ± 0.36).

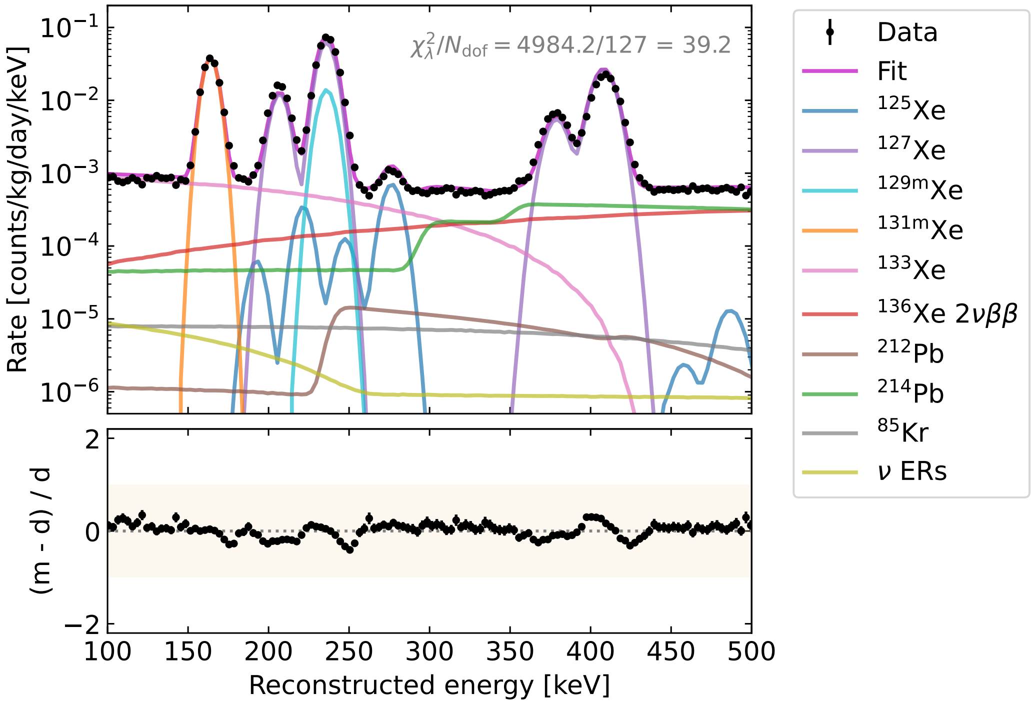

(a) central sub-volume fit

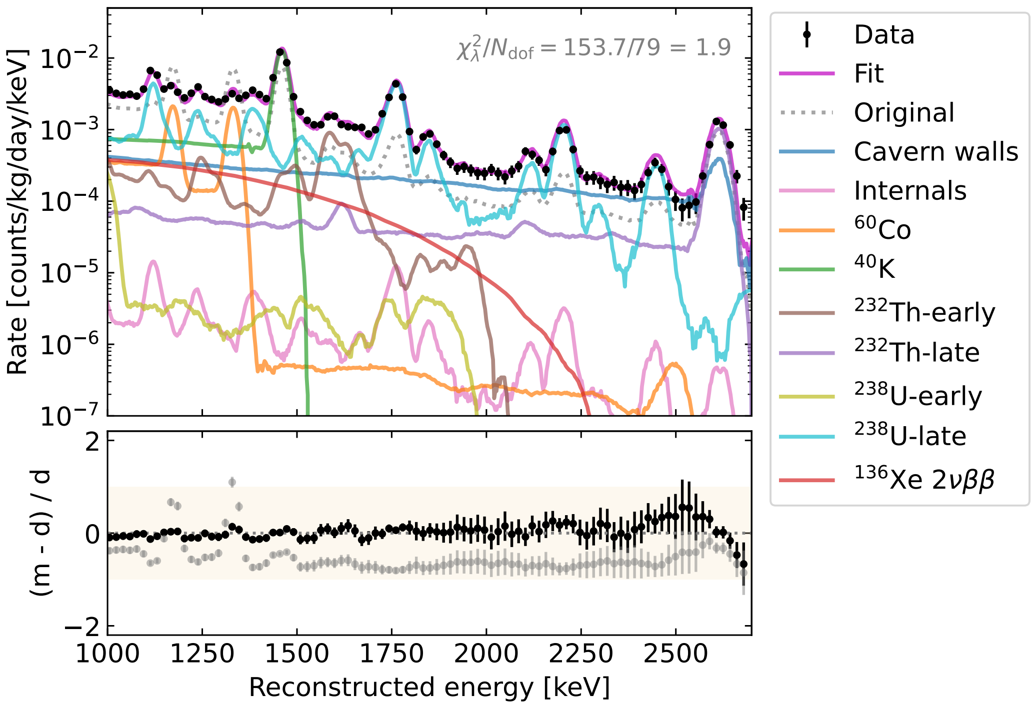

(b) lateral sub-volume fit

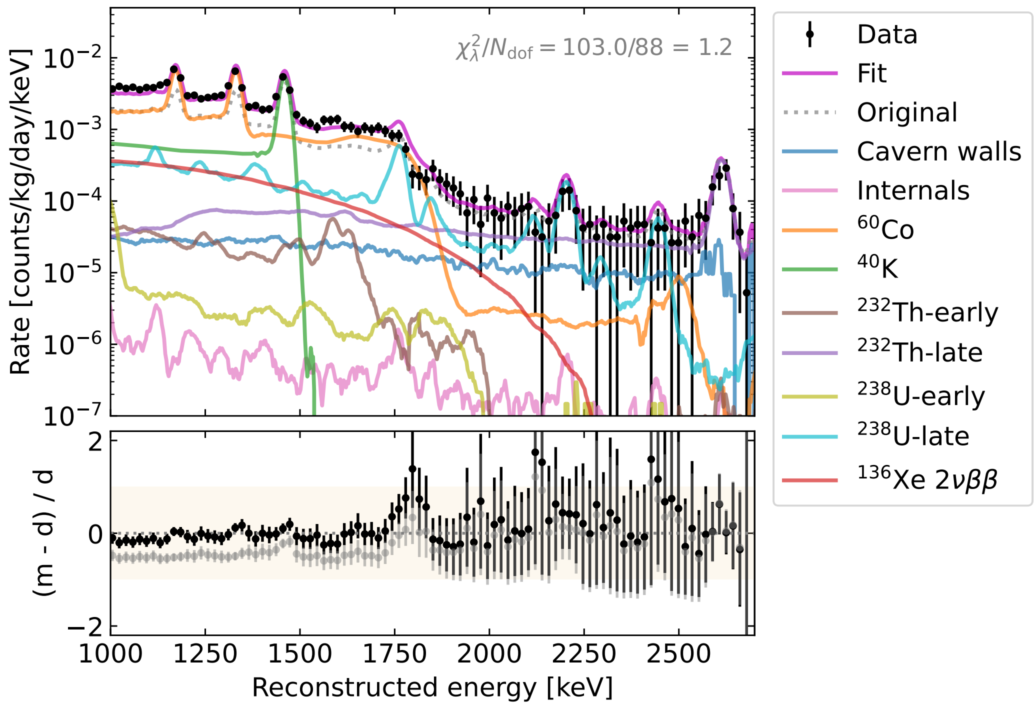

(c) lower sub-volume fit

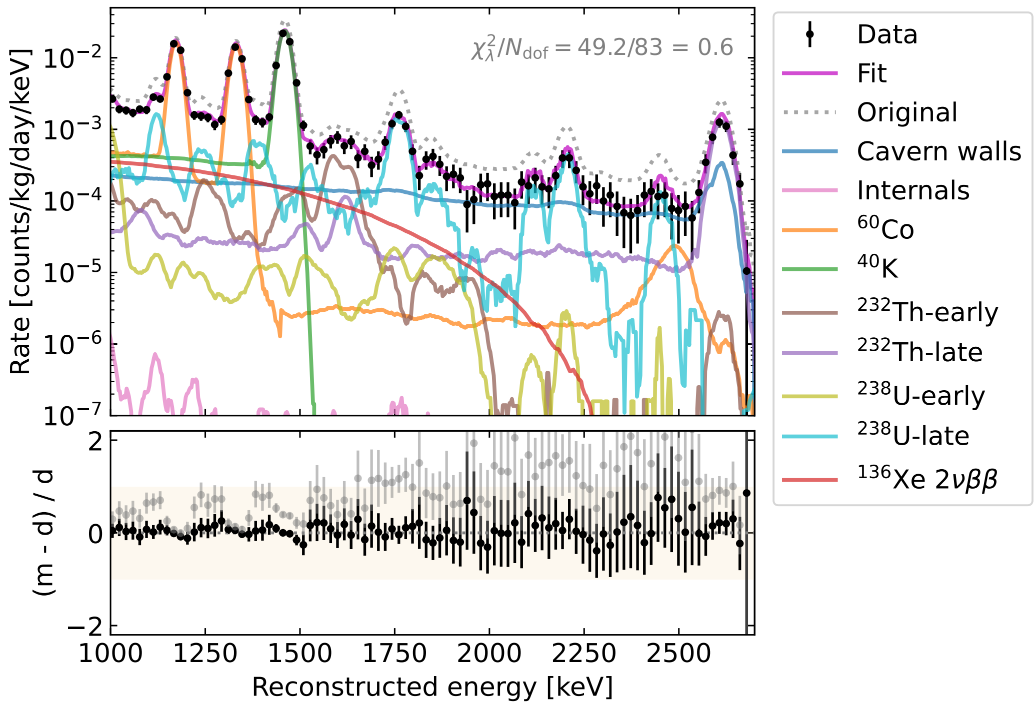

(d) upper sub-volume fit

Figure 4.17: Sub-volume fits, with the initial estimates in grey for all cases except the central sub-volume, where the adjustment is minimal. To visualise the quality of each fit, the fractional differences between the fitted models $\boldsymbol{m}$ and the data $\boldsymbol{d}$ are displayed in the residual plots. Groups have been combined by source in (b)–(d) for comprehensibility.

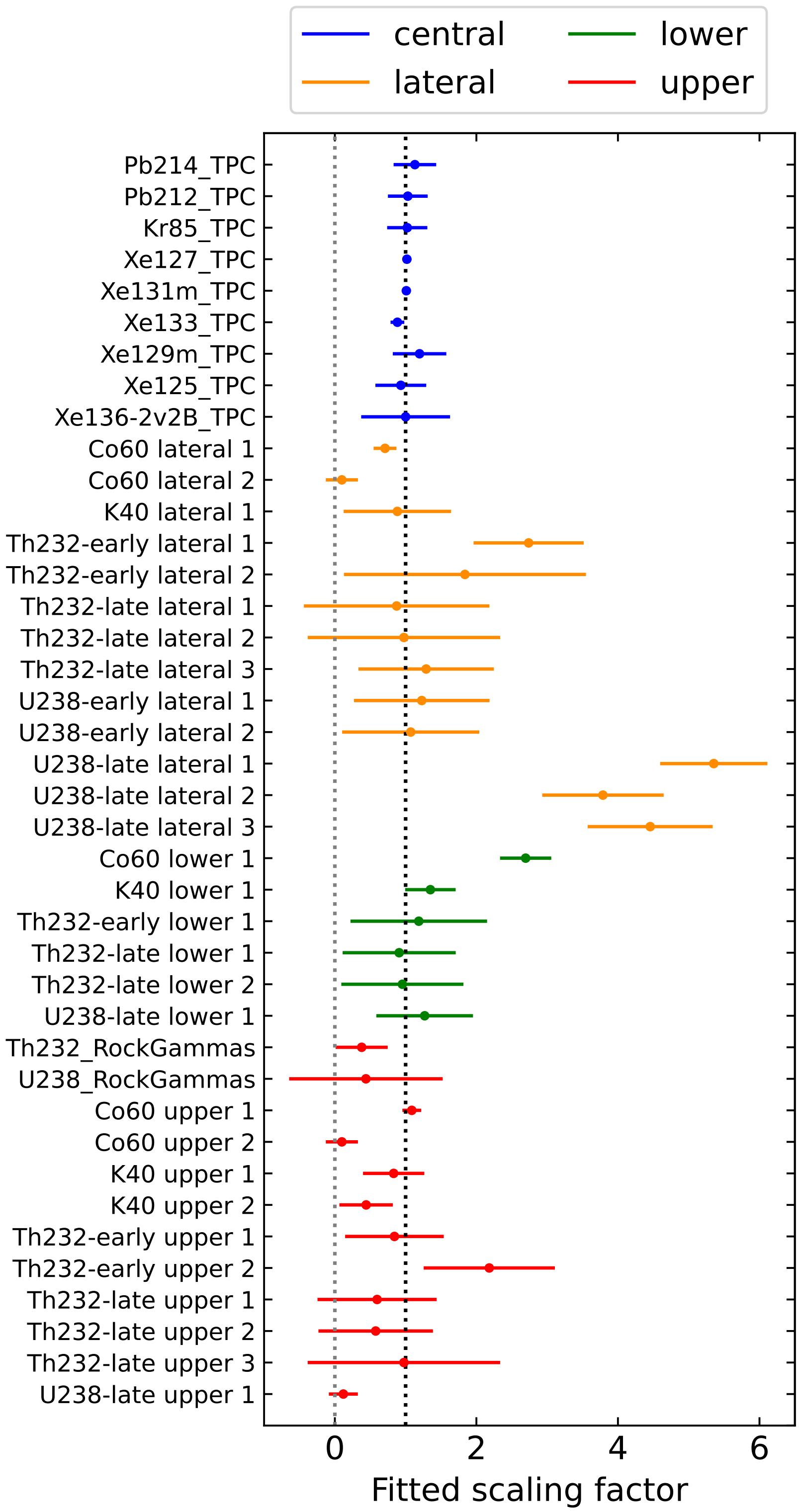

Figure 4.18: Effective scaling for each group as a result of the sub-volume fits. Note that the cavern gamma rays and ICV components were fitted in both the lateral and upper sub-volumes. For a given source, the number of groups can change between sub-volumes due to the positional dependence of relative event proportions and spectral shapes.

- **Decreased ^{60}Co in the cryostat** – a reduction in ^{60}Co rates for the ICV and OCV flange bolts was noted. In particular, a scaling factor of $0.10^{+0.19}_{-0.1}$ was observed for the latter. The initial overestimation was suspected to be a result of assaying titanium alloy material similar to that of the installed bolts as a proxy for the activity, rather than the actual bolts themselves.

- **Elevated ^{238}U-late in the cryostat** – although radioassay measurements assumed that each chain is in secular equilibrium, this was not necessarily the case as chemical processes at the manufacturing stage can deplete the concentrations of late-stage daughters. Due to the long half-lives involved, this induces a quasi-permanent break in secular equilibrium for the typical $\mathcal{O}(10)$ year timescale of a dark matter experiment, and therefore leads to an under-representation of some radionuclides [262]. This is reflected by a mean scaling factor of (4.54 ± 0.78) for ^{238}U-late in the lateral sub-volume fit.

The final SR1 FV fit is presented in Figure 4.19. An initial underestimation in material backgrounds is visible in the residuals plot, which is rectified by the fitted model. Table 4.5 compares the fitted material activities with assay estimates for each of the regional groups floated in the SR1 FV fit. To ensure these comparisons are meaningful, the accumulated activities only included components that were reasonably captured by the fit, as assessed according to two criteria: the component should provide $>1\%$ of all FV events, and $>1\%$ of its decays should produce hits in the TPC. Imposing these conditions discarded components that possess high intrinsic activities and a low yield of events in the TPC, such as OD PMTs.

Inspecting the position distributions of events in simulations and data prior to fitting revealed a potential mismodelling issue; more simulated events were recorded at the side than the top of the TPC with respect to data. This may be responsible for the observed exchange in activity between the side and top groups in Table 4.5, for sources such as ^{40}K. This behaviour is most directly corroborated by the contradictory fitted scaling factors for cavern gamma ray contributions, with (3.5 ± 1.3)

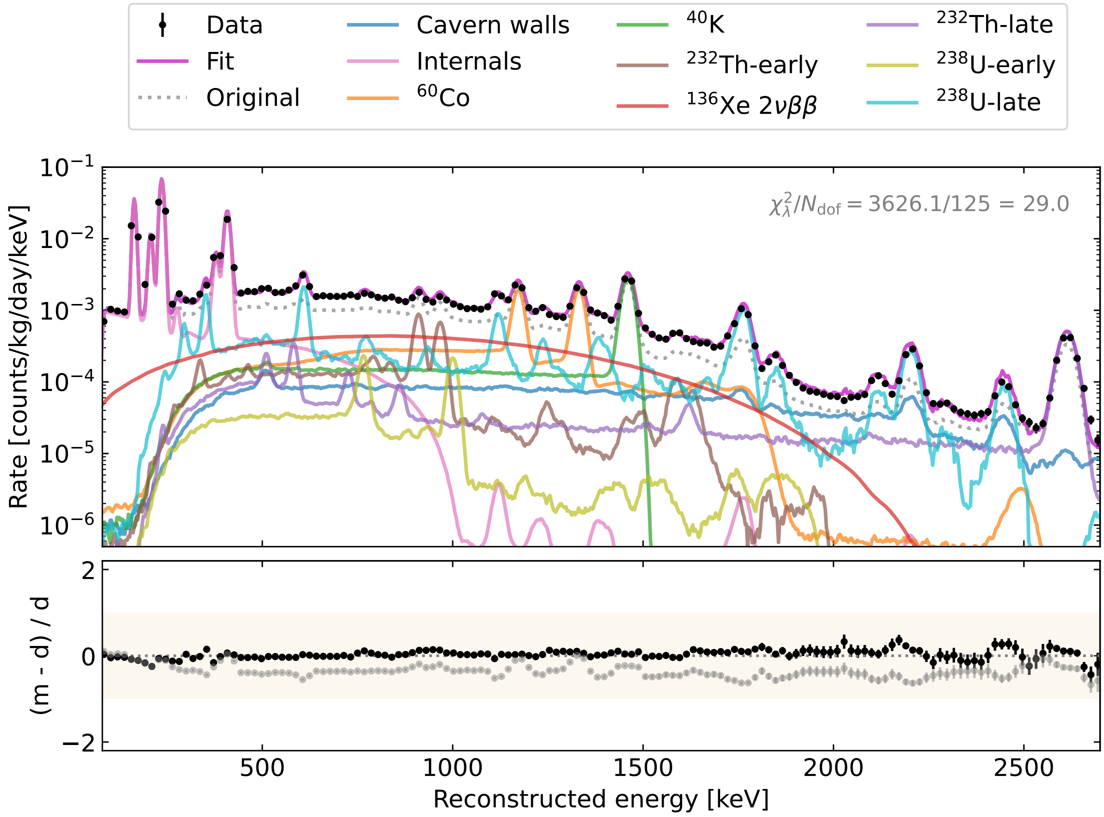

Figure 4.19: Fitted spectra in the SR1 FV, following the prescribed sequence of sub-volume fits. The residuals are approximately zero on average, with fluctuations around certain peaks arising from imperfections in energy resolution matching. Contributions from internals were fixed in this fit according to the central sub-volume results. For clarity, groups have been combined by source and hence there are fewer curves than the 21 total parameters involved in this fit.

for the lateral sub-volume as opposed to (0.4 ± 0.1) for the upper sub-volume fits. The upper sub-volume result, along with the SR1 FV value of $0.6^{+0.7}_{-0.6}$, are consistent with the factor (0.65 ± 0.14) measured when the OD and water tank were empty and the xenon target was in a gaseous phase [248].

In the case of ^{238}U-early however, an overall increase was recorded rather than a trade-off in activity between groups. This behaviour is suspected as a consequence of the inherently low rate and hence the lack of sensitivity to ^{238}U-early sources. The systematic boost to these rates for all regions is likely a result of correlation with other groups.

Table 4.5: Overview of radioassay estimates and best-fit results for source activities of groups considered in the SR1 FV fit. A general exchange between top and side regions is indicatave of a possible mismodelling issue in the simulations. Late-stage decays for the ^{238}U and ^{232}Th chains observe an increase due to a breakdown in the assumption of secular equilibrium made in the radioassay measurements.

Source	Region	Screening estimate [Bq]	Best fit [Bq]	Scaling factor
^{60}Co	Top	1.13 ± 0.11	1.17 ± 0.11	1.04 ± 0.14
	Side	1.71 ± 0.17	0.79 ± 0.49	0.46 ± 0.29
	Bottom	0.81 ± 0.08	1.76 ± 0.23	2.17 ± 0.35
	Total	3.65 ± 0.22	3.72 ± 0.55	1.02 ± 0.16
^{40}K	Top	7.63 ± 0.76	3.74 ± 2.10	0.49 ± 0.28
	Side	2.56 ± 0.26	7.02 ± 1.54	2.74 ± 0.66
	Bottom	6.54 ± 0.65	6.30 ± 2.61	0.96 ± 0.41
	Total	16.73 ± 1.04	17.05 ± 3.68	1.02 ± 0.23
^{232}Th-early	Top	0.28 ± 0.03	0.51 ± 0.44	1.83 ± 1.57
	Side	0.66 ± 0.07	0.45 ± 0.35	0.68 ± 0.54
	Bottom	0.22 ± 0.02	0.27 ± 0.19	1.23 ± 0.88
	Total	1.16 ± 0.07	1.23 ± 0.59	1.06 ± 0.52
^{232}Th-late	Top	0.25 ± 0.02	0.14 ± 0.18	0.57 ± 0.74
	Side	1.05 ± 0.10	2.41 ± 1.76	2.31 ± 1.70
	Bottom	0.30 ± 0.03	0.23 ± 0.23	0.77 ± 0.77
	Total	1.59 ± 0.11	2.78 ± 1.78	1.75 ± 1.13
^{238}U-early	Top	2.37 ± 0.24	2.41 ± 0.75	1.02 ± 0.33
	Side	1.99 ± 0.20	4.46 ± 3.83	2.24 ± 1.94
	Bottom	1.86 ± 0.19	2.76 ± 1.68	1.48 ± 0.92
	Total	6.21 ± 0.36	9.62 ± 4.25	1.55 ± 0.69
^{238}U-late	Top	0.84 ± 0.08	0.61 ± 0.28	0.72 ± 0.34
	Side	0.54 ± 0.05	3.11 ± 0.64	5.78 ± 1.32
	Bottom	0.95 ± 0.09	1.27 ± 0.72	1.34 ± 0.77
	Total	2.32 ± 0.14	4.98 ± 1.00	2.14 ± 0.45

4.8 Implications for high energy searches

These findings only had a slight effect on the WIMP search; the expected number of detector ER background events in the WIMP ROI increased marginally from 1.2 events to 1.4 events, after accounting for cut acceptances. However, the elevated material background rates have significant implications for high energy searches. In particular, the doubled activity for ^{238}U-late components poses a concern to the search for ^{136}Xe $0\nu\beta\beta$ decay as it translates into a larger background from the ^{214}Bi gamma-ray line. This is counteracted by the observed improvement to the energy resolution at $Q_{\beta\beta}$ – from 1% assumed in the official sensitivity study [247], to 0.75% as demonstrated in Figure 4.10 (d). In order to assess the overall impact on the half-life sensitivity, the published study was repeated with an updated energy resolution and background model. The PLR was evaluated in (E, R^2, z) space for exposures of 1000 live days within a cylindrical 5.6 tonne volume, which produced the median sensitivity profile shown in Figure 4.20, as a function of the ^{238}U-late activity. The resulting exclusion sensitivity is at a half-life of 0.98×10^{26} years, which is slightly worse than the initial reported estimate of 1.06×10^{26} years. In the future, this outcome may improve with refinements to signal non-uniformity corrections and hence the energy resolution, as well as with the development of techniques to enhance the vertical position resolution for better SS-MS discrimination.

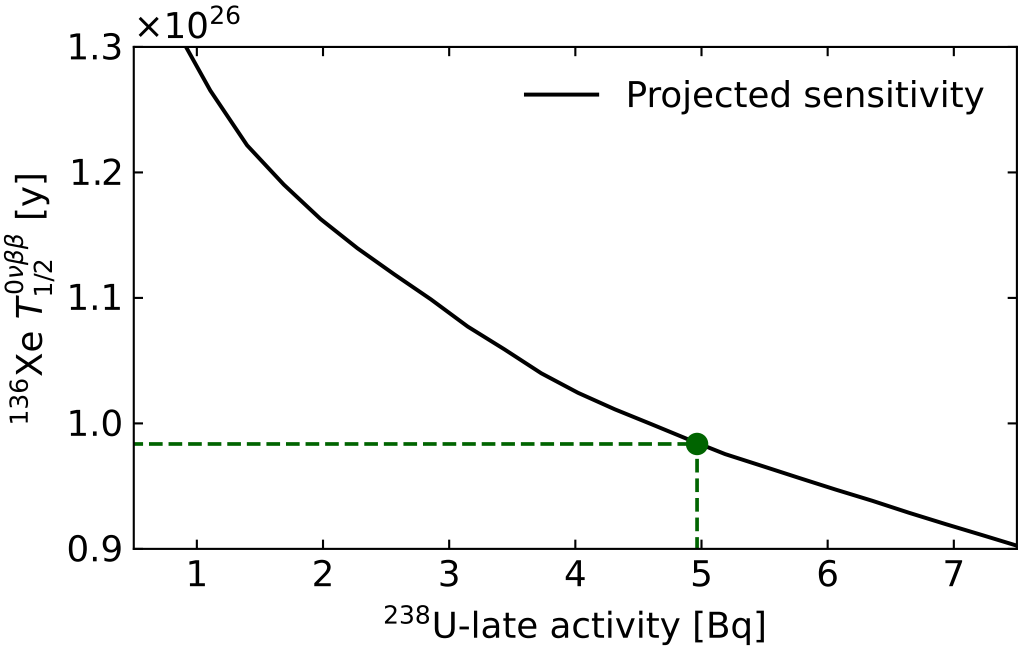

Figure 4.20: Updated projection for the median sensitivity to the ^{136}Xe $0\nu\beta\beta$ half-life at 90% confidence level, as a function of the ^{238}U-late activity, and over an exposure of 1000 live days. An energy resolution of 0.75% at $Q_{\beta\beta}$ is assumed. The green point and dashed lines indicate the new sensitivity estimate corresponding to a ^{238}U-late activity scaled up by a factor of 2.14, as per the fit results. The framework used to produce this result was developed for the official sensitivity study by R. Taylor [168].

4.9 Conclusion

The measurement of detector material backgrounds in LZ has implications beyond the vanilla WIMP search, since high-energy gamma sources impact the sensitivity towards other searches for new physics, such as ^{136}Xe $0\nu\beta\beta$ decay, as well as ^{134}Xe $0\nu\beta\beta$ and $2\nu\beta\beta$ decays [245, 247]. In turn, the ability to leverage radioassay measurements also influences the strategies and requirements for larger next-generation dark matter detectors.

The process of constructing a material background model for SR1 was outlined, which involves binned maximum-likelihood fits of simulated energy spectra to data. To treat the position dependence of various components, as well as handle the high multiplicity of sources, an approach employing a series of fits within different partitions of the detector was developed to prime a final fit within the SR1 FV. The level of complexity was further reduced by the implementation of a component grouping algorithm. In tandem, these methods simplified the task down from over a thousand components to ≤ 21 model parameters in a given fit.

To maximise compatibility between simulated and measured spectra, and hence improve the overall fit quality and robustness, a dedicated energy calibration extending up to 3 MeV was performed, along with treatment of subtle energy reconstruction effects. This included corrections to a systematic shift in the peak means from their expected values, which improved the level of agreement from $\pm 0.8\%$ to $\pm 0.2\%$, along with the data-driven implementation of an energy-dependent smearing model in simulations.

Results from the fitting process predominantly verified radioassay measurements, with the majority of effective scaling factors for component rates at values consistent with 1. Observed discrepancies between the fitted model and initial expectations were generally supported by supplementary information: rates of ^{60}Co in the bottom array were raised by a factor of (2.17 ± 0.35), as explained by the placement of neutron-activated PMTs; and an underestimation of ^{238}U-late and ^{232}Th-late rates was attributed to breaks in secular equilibrium during the manufacturing stage, in conflict with the assumptions made for radioassay measurements. Furthermore, potential simulation mismodelling issues were revealed by discrepancies between fitted activities in the sides and top of the TPC, particularly in the case of cavern gamma components.

The fitted scaling factors, along with the measured energy resolution at $Q_{\beta\beta}$, were propagated into the official sensitivity study for ^{136}Xe $0\nu\beta\beta$ decay. As a consequence of the increased ^{238}U-late activity, the updated median half-life exclusion sensitivity was slightly reduced, at 0.98×10^{26} years for a run exposure of 1000 live days.

5 Two-neutrino double electron capture of ^{124}Xe

First observations of the decay of ^{124}Xe in LZ via two-neutrino double electron capture ($2\nu 2$EC) are presented in this chapter. Thus far, the half-life of this extremely rare decay has only been measured by the XENON1T experiment. However, the SR1 exposure is sufficiently high to enable a competitive measurement of the half-life, along with a preliminary estimate of the decay mode capture fractions.

5.1 Context and motivation

In addition to rare double beta decay searches, the advent of new detector technologies has enabled the detection of rare $2\nu 2$EC decays with half-lives that exceed the age of the universe by several orders of magnitude. Thus far, $2\nu 2$EC decay has been observed for ^{130}Ba in geochemical surveys [263, 264], ^{78}Kr in BNO [265, 266], and ^{124}Xe in XENON1T [267, 268]. LZ satisfies all the necessary requirements for conducting this measurement for ^{124}Xe: a large quantity of xenon, a low-background environment, excellent energy resolution, and long-term operation. Constraints of the $2\nu 2$EC half-life play an important role in the development of nuclear structure models [269], and pave the way towards the detection of more exotic variants of double positron emission ($2\nu\beta^+\beta^+$) and EC coincident with positron emission (2νECβ^+), as well as beyond-the-Standard-Model neutrinoless modes [270]. Moreover, understanding the rate of $2\nu 2$EC decays in LZ is crucial as it contributes a background to the WIMP search, as well as low-energy ER searches for light dark matter candidates such as axion-like particles and hidden photons [142, 271, 272].

5.2 Signal model

$2\nu 2$EC is a second-order weak process allowed by the Standard Model, whereby two electrons are absorbed from atomic shells, resulting in the conversion of two protons into neutrons and the simultaneous emission of two neutrinos. ^{124}Xe undergoes $2\nu 2$EC to ^{124}Te with a reaction Q-value of $(2856.73 \pm 0.12)\,\mathrm{keV}$ [273]:

$$^{124}\mathrm{Xe} + 2e^- \longrightarrow {}^{124}\mathrm{Te} + 2\nu_e + (\text{X-rays \& Auger electrons}). \quad (5.1)$$

The subsequent de-excitation of the ^{124}Te daughter results in the emission of a cascade of X-rays and Auger electrons as the shell vacancies are refilled. These form the only detectable signals as most of the energy is carried by the escaping neutrinos, whilst the nuclear recoil energy is only $\mathcal{O}(10)$ eV [274]. Furthermore, due to the sub-millimetre mean free path of these signals and the short timescales involved, they cannot be individually resolved in the detector and are hence expected to manifest purely as SS interactions.

The energy of the experimental signature depends on the combination of atomic shells from which electrons were captured. To date, the most sophisticated model of the energies and relative capture fractions has been developed by the XENON collaboration, which considers up to the N5 shell ($4\mathrm{d}_{5/2}$ in atomic notation [275]) in the theoretical calculation [268]; these values are listed in Table 5.1. This model was implemented in BACCARAT by approximating the X-ray and Auger electron cascade as a single beta, which correctly reproduces the $\sim$100% SS efficiency. The associated energy spectrum is illustrated in Figure 5.1.

For an isotopic exposure of $0.87\,\mathrm{kg} \times \mathrm{y}$, XENON1T reports the half-life of ^{124}Xe at $T_{1/2}^{2\nu 2\mathrm{EC}} = (1.1 \pm 0.2_{\mathrm{stat}} \pm 0.1_{\mathrm{sys}}) \times 10^{22}\,\mathrm{years}$, with a statistical significance of 7σ [268].

Table 5.1: Energies and capture fractions for different shell combinations in ^{124}Xe double electron capture, as produced by the XENON1T model. The pair of letters for each mode denote the atomic shells from which electrons were captured. The LM mode energy was obtained using values from [276].

Decay mode	Capture fraction [%]	Energy [keV]
KK	72.4	64.3
KL	20.0	36.7–37.3
KM	4.3	32.9–33.3
KN	1.0	32.3–32.4
LL	1.4	8.8–10.0
LM	0.8	6.0
Other	0.1	<6.0

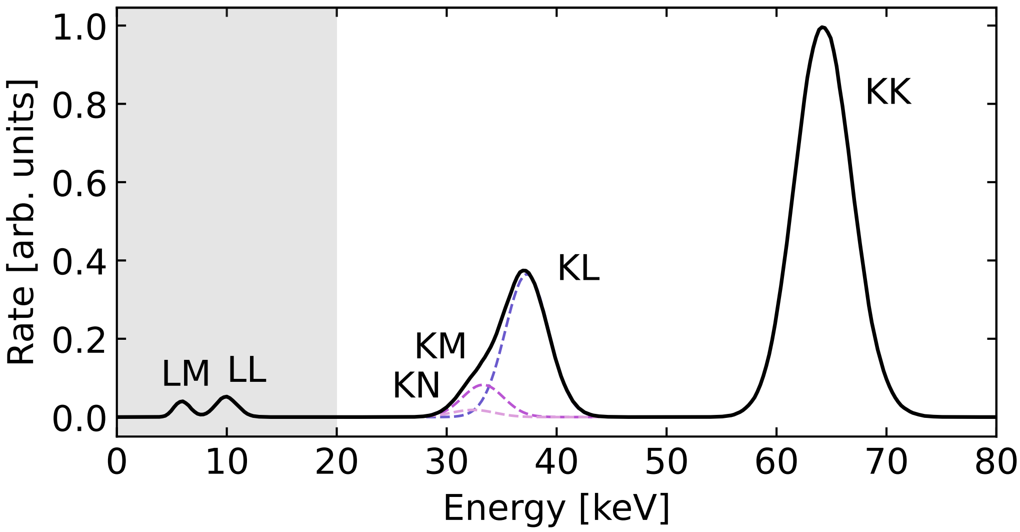

Figure 5.1: Simulated energy spectrum of the ^{124}Xe 2ν2EC signal model. Dashed lines are used to visualise the substructure of the secondary peak. The shaded region is excluded from the fits in this work, but encompasses peaks that pose a background to low energy searches in LZ.

The half-life is related to the activity $A_{2\nu2\text{EC}}$ by

$$A_{2\nu2\text{EC}} = \frac{\eta N_A}{T_{1/2}^{2\nu2\text{EC}} M_A} \ln 2, \tag{5.2}$$

where N_A is Avogadro's constant, $M_A = (131.293 \pm 0.006)$ g/mol is the molar mass of xenon [277], and η is the isotopic abundance of ^{124}Xe, assumed to be consistent with the natural composition at $(0.0952 \pm 0.0003)\%$ [246]. This leads to a predicted rate of (8.72 ± 2.38) nBq/kg, which translates into (5.3 ± 1.4) counts/d within the 7-tonne active volume. Over the entire course of SR1, < 17 events are predicted to occur from the LL and LM captures. Therefore, a 20–120 keV interval was set as the ROI for this search; the lower bound reflects the lack of sensitivity to these modes, whereas the upper bound encapsulates the energies of flat backgrounds occurring below the 163.9 keV $^{131\mathrm{m}}$Xe activation peak.

5.3 Fiducialisation

As mentioned in Section 3.5.3, a suite of data quality cuts was developed for the SR1 WIMP search, with a focus on suppressing accidental coincidence backgrounds. However, within the 2ν2EC ROI, the complete set of data quality cuts only accounts for $< 0.08\%$ of discarded events beyond a set of four core cuts: the FV cut, area thresholds (S1c > 100 phd) and ($\mathrm{S2_{raw}} > 600$ phd), and vetoes from the skin and OD. This is predominantly due to a significant overlap with the FV cut; accidental backgrounds and misreconstructed events addressed by the data quality cuts mainly occur within proximity to the gate grid and the TPC wall, and are hence also removed through fiducialisation. Consequently, this places an emphasis on the importance of a tuned FV.

The role of the FV cut in the 2ν2EC measurement is primarily to limit the background from detector materials, which is already extremely subdominant below $\sim$200 keV, as well as to minimise the effects of charge loss due to field non-uniformities, which impact the energy reconstruction and resolution. This presents a trade-off with respect to the fiducial mass, which is directly proportional to the number of signal events. By inspecting simulated material backgrounds in the ROI shown in Figure 5.2, it is evident that whilst the SR1 FV with (5.5 ± 0.2) tonnes of xenon is effective, there is more mass to be gained both radially and at the top of the TPC. Therefore, to maximise the amount of ^{124}Xe and hence the sensitivity, it was necessary to expand into a new FV.

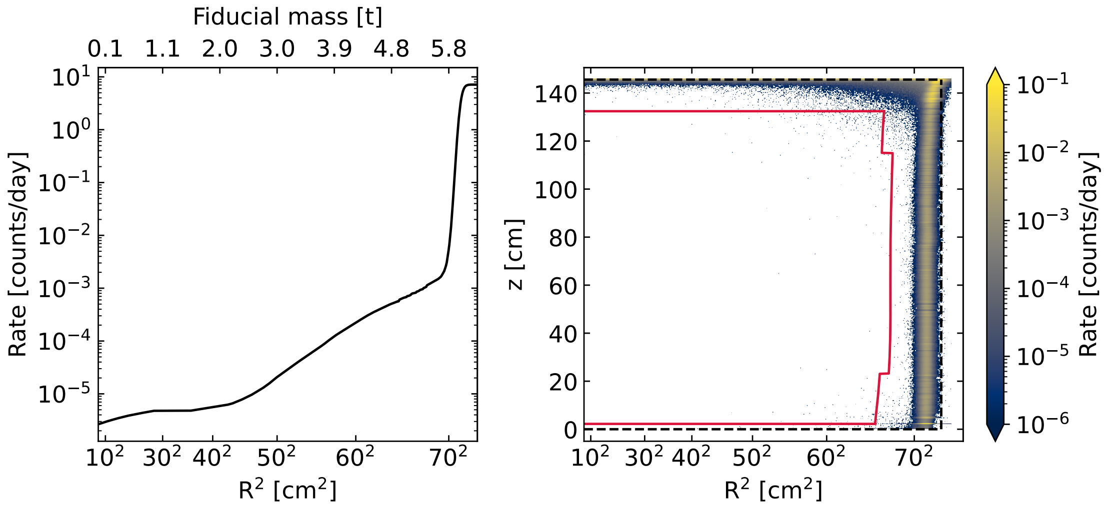

Figure 5.2: The rate of simulated material backgrounds for a cylindrical volume with ($2.2\,\mathrm{cm} \leq z \leq 132.4\,\mathrm{cm}$) and radius R (left), and their positional distribution with the SR1 FV outlined in red (right). Both cases only consider SS events within the 20–120 keV ROI, with area threshold cuts and vetos applied. The dashed black border indicates the boundaries of the active xenon volume.

The fiducialisation process utilised SS events within an 80–120 keV sideband, with area threshold cuts and vetos applied. In order to simplify the procedure, the vertical and radial aspects were considered separately, since the optimal z boundaries are expected to remain consistent across all potential FV shapes. The suitability of a given FV geometry was assessed according to a sensitivity metric S_{V}, defined as

$$S_{\mathrm{V}} = \frac{M}{\sqrt{N_{\mathrm{B}}}}, \tag{5.3}$$

which resembles the discovery significance for a counting experiment with N_{B} background events, and the fiducial mass M substituted for the number of signal events as they are directly related.

The z limits were optimised first by maximising S_{V} for a cylindrical volume with its radius fixed at a conservative value of 68 cm, including a short stand-off distance to mitigate for charge loss at the TPC wall. This reproduced the same lower z bound as SR1 at 2.22 cm, but extended the upper z bound by 4.57 cm up to 136.97 cm. The fitted z bounds were then propagated into the optimisation of three candidate FV shapes:

- **Cylinder** – the simplest available choice is a cylindrical volume, as was often assumed for sensitivity studies in LZ [229, 245, 247]. With the z limits fixed at the values obtained above, the optimised maximum radius was $R_{\mathrm{max}} = 67.9\,\mathrm{cm}$. To check that this value was not biased as a consequence of fixing the vertical bounds, all three parameters were allowed to float together, which produced the same results.

- **Superellipsoid** – a more generalised form of the cylindrical volume is a superellipsoid, commonly employed by the XENON collaboration. This is parametrised in (R^2, z) space as a semi-superellipse with the functional form

$$\left|\frac{R^2}{a}\right|^n + \left|\frac{z+z_0}{b}\right|^n = 1, \tag{5.4}$$

  where the first and second terms pertain to the radial and vertical aspects of the shape, respectively. The semi-minor axis $b = 67.4\,\mathrm{cm}$ and the vertical offset $z_0 = 3.2\,\mathrm{cm}$ were determined first by iterative means with the other parameters fixed, such that the vertical bounds of the semi-superellipse matched the optimised z limits. With b and z_0 then fixed, maximising S_{V} produced an index $n = 9.1$ and a semi-major axis of $a = 4742.6\,\mathrm{cm}^2$. An index of $n = 2$ corresponds to a standard ellipse, whereas values of $n > 2$ create a rectangle with rounded corners, eventually approaching an ordinary rectangle as n tends to infinity. The relatively high value of n generated by the fit suggests that there is little benefit in using a superellipsoidal volume, hence the outcome starts to closely resemble a cylindrical volume.

- **Poly-wall** – to reliably capture the profile of the reconstructed TPC wall, following the curvature of the drift field lines, a more tailored shape was also considered. The detector volume was sliced in z between the optimised limits, effectively creating a stack of flat cylindrical volumes. A contour of the wall was then approximated by extracting the radius that maximises S_{V} for each slice, and subsequently fitting the set of radii with a fifth-order polynomial. Minimal differences in the final value of S_{V} were observed for higher order polynomials or more than $\sim$50 slices.

All three optimised FV candidates are superimposed on data in Figure 5.3, along with the SR1 FV for reference. To inform the choice of FV, the behaviour of S_V as a function of M was explored by varying the radial aspect of each volume: R_{max} for the cylinder, a for the superellipsoid, and a radial offset for the poly-wall volume. In each case, M was estimated numerically on the basis of the active detector volume containing 7 tonnes of xenon. As shown in Figure 5.4, although the three candidate volumes perform similarly well, S_V is generally higher for the poly-wall volume, and it peaks in sensitivity at a greater fiducial mass. Thus, the poly-wall volume was selected as the optimal FV for this analysis.

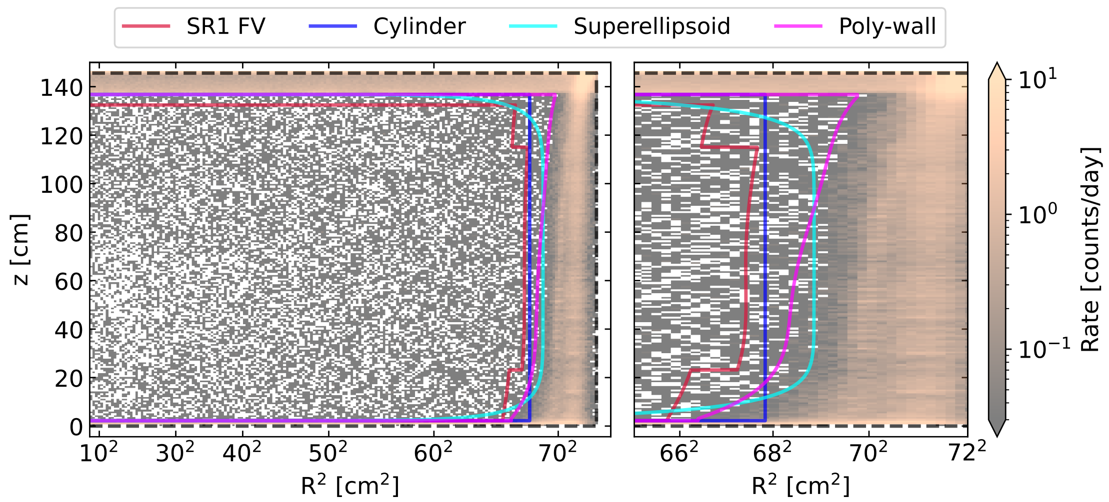

Figure 5.3: Optimised FV candidates overlaid on the position distribution of SS events within the 20–120 keV ROI in SR1 data, with area threshold cuts and vetos applied. The boundaries of the active volume are marked with a dashed black line. It is visually apparent that all candidates lead to a gain in fiducial mass, with the poly-wall volume following the reconstructed wall shape most closely.

The fiducial mass M_{poly} of the poly-wall FV was approximated using data from a post-SR1 ^{83m}Kr injection. This calibration source is ideal for this purpose as it is dispersed throughout the TPC and yields many events. Moreover, since the decay of ^{83m}Kr consists of a two-step process with a separation of 154 ns, it displays a characteristic double-S1 signature and is hence straightforward to select [278]. By comparing the number of ^{83m}Kr events in the poly-wall volume as a fraction of those within a reference cylindrical volume, which uses the same z limits and a

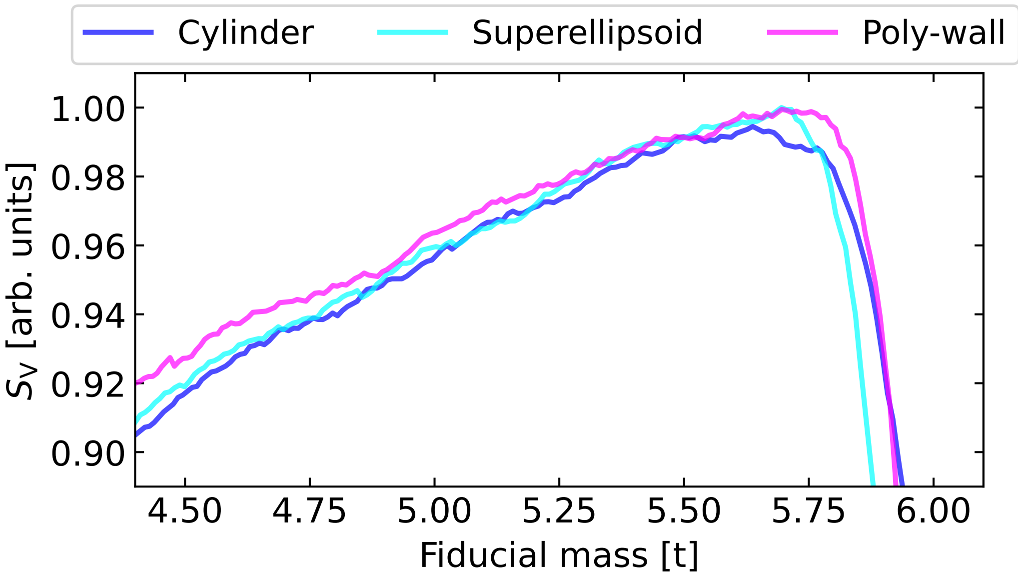

Figure 5.4: Profiles of the sensitivity metric S_V as a function of the fiducial mass M, for each of the three FV candidates. The y-axis is arbitrarily normalised to aid in interpretability.

radius of 70 cm, the fiducial mass was measured as

$$M_{\text{poly}} = (5.73 \pm 0.01_{\text{stat}} \pm 0.03_{\text{sys}})\,\text{tonnes}, \tag{5.5}$$

where the systematic uncertainty originates from the difference with respect to the numerical estimate; for the SR1 FV, a greater uncertainty resulted from the combination of results from multiple methods and datasets. Overall, switching from the SR1 FV to the poly-wall FV achieves a 3.8% gain to the overall exposure. However, although the contribution of detector materials to the background remains minuscule, it is larger in the poly-wall FV than the SR1 FV by a factor of ∼4.8.

5.4 Background model

The majority of backgrounds within the 20–120 keV 2ν2EC ROI, summarised in Table 5.2, exhibit flat and continuous energy spectra, which makes them more straightforward to model. Furthermore, their rates in SR1 have been well-constrained by a variety of sideband studies [248]. In particular, a subset of these backgrounds is comprised of unstable xenon isotopes, which are produced via neutron activation as a result of deploying neutron sources to calibrate the detector response to

NRs. Aside from ^{133}Xe, which features as a beta spectrum with a shoulder starting at 81.0 keV, these can deposit energies within close proximity to the secondary ^{124}Xe signal peak. Isotopes with decays involving a single EC, namely ^{125}Xe and ^{127}Xe, involve cascades with a total deposited energy of 33.2 keV for K-shell captures [279]. However, these decays are accompanied by a gamma ray, which often gives rise to a MS topology or is tagged by the veto detectors with an efficiency of $(78.0 \pm 5.0)\%$, and hence they are suppressed by the SS and veto cuts. Similarly, ^{129m}Xe emits a pair of 196.6 keV and 39.6 keV gamma rays in its transitions to the ground state, with a low probability of detecting the lower energy gamma in isolation as the other escapes.

Table 5.2: Summary of backgrounds to the ^{124}Xe 2ν2EC measurement. Reported rate estimates are for SS events within the ROI, after the application of area thresholds, vetos, and a FV cut. Solar neutrino and detector material backgrounds consist of a sum over all relevant ER sources. Half-lives are omitted in cases where they exceed the lifetime of the experiment, or for sources that are continuously produced.

Source	ROI signature	Half-life	Average rate [mHz]
^{125}I	Multiple EC peaks	59.4 d	(0.28 ± 0.04)
^{125}Xe	K-shell EC (33.2 keV)	16.9 h	$(9.7 \pm 0.6) \times 10^{-5}$
^{127}Xe	K-shell EC (33.2 keV)	36.3 d	$(8.5 \pm 0.1) \times 10^{-3}$
^{129m}Xe	γ (39.6 keV)	8.9 d	$(6.7 \pm 0.3) \times 10^{-3}$
^{133}Xe	$\beta + \gamma$	5.2 d	(10.9 ± 0.4)
^{136}Xe $2\nu\beta\beta$	continuous	-	(0.21 ± 0.01)
^{212}Pb	continuous	-	$(7.6 \pm 0.8) \times 10^{-3}$
^{214}Pb	continuous	-	(0.29 ± 0.01)
^{85}Kr	continuous	-	$(5.1 \pm 0.5) \times 10^{-2}$
Solar neutrinos	continuous	-	$(6.9 \pm 0.7) \times 10^{-2}$
Materials	continuous	-	$(4.3 \pm 0.4) \times 10^{-3}$

5.4.1 ^{125}I

An especially problematic background is ^{125}I, which is produced by the neutron activation of ^{124}Xe according to the following steps:

$$^{124}\text{Xe} + n \longrightarrow {}^{125}\text{Xe} + \gamma, \tag{5.6}$$

$$^{125}\text{Xe} \xrightarrow{\text{EC}} {}^{125}\text{I} + \nu_e + \gamma + (\text{X-rays \& Auger electrons}), \tag{5.7}$$

and decays to an excited state of ^{125}Te via EC:

$$^{125}\text{I} \xrightarrow{\text{EC}} {}^{125}\text{Te} + \nu_e + \gamma + (\text{X-rays \& Auger electrons}). \tag{5.8}$$

The combination of the subsequent de-excitation cascades and the 35.5 keV gamma ray emitted by the ^{125}Te daughter generates peaks that significantly overlap with the ^{124}Xe signals. For instance, the K-shell capture mode of ^{125}I has an associated total energy of 67.3 keV; with a measured energy resolution of $(4.5 \pm 0.4)\%$, this peak is within 1σ of the 64.3 keV KK capture combination of ^{124}Xe. This is similarly the case for the other ^{125}I decay modes, listed in Table 5.3.

Table 5.3: Energies and capture fractions for ^{125}I background peaks. The capture fractions are quoted from [280], and the X-ray transition energies are taken from [281, 282] with uncertainties excluded as they are of $\mathcal{O}(1)$ eV.

Decay mode	Capture fraction [%]	Energy [keV]
γ + K	80.11 ± 0.17	67.3 (35.5 + 31.8)
γ + L	15.61 ± 0.13	40.4 (35.5 + 4.9)
γ + M	3.49 ± 0.07	36.5 (35.5 + 1.0)

Getter removal

Whilst ^{125}I has a natural half-life of 59.4 d, it is efficiently removed by the LZ purification system, which employs a hot zirconium getter. To quantify the removal rate during SR1, the 67.3 keV ^{125}I peak was isolated by fitting the corresponding population in $(\text{S1c}, \text{S2c}_{\text{bot}})$ space with a two-dimensional Gaussian, and keeping events within the 2σ elliptical contour as depicted in Figure 5.5 (a). This was performed for a selection of SS events that passed a minimal set of cuts, namely the area thresholds, vetoes, and FV cut, all alongside the exclusion of periods with elevated detector activity. The effect of applying the minimal cuts, the rest of the SR1 data quality cuts, and the elliptical contour cut on the ROI energy spectrum in succession are illustrated in Figure 5.5 (b).

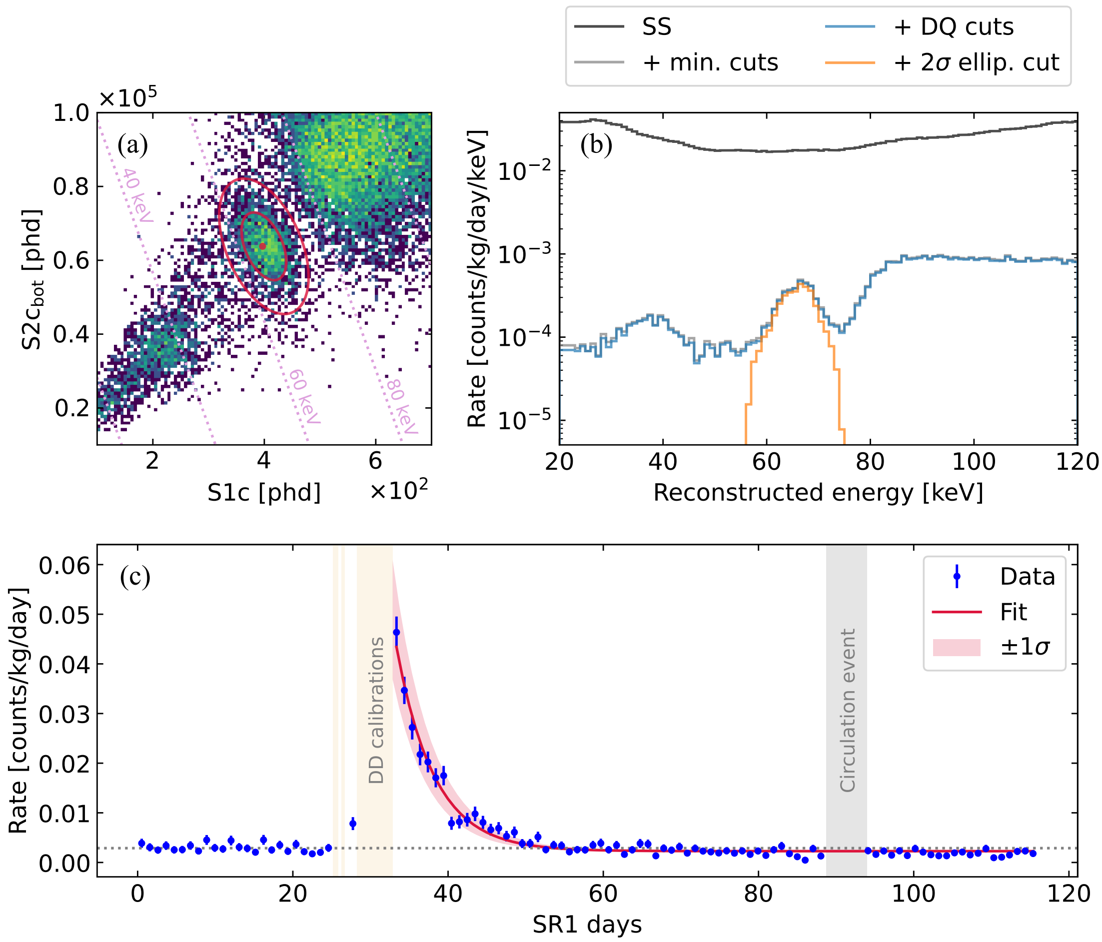

Figure 5.5: Characterisation of ^{125}I removal in SR1 by the LZ purification system. (a) Selection of K-shell EC mode of ^{125}I from events passing minimal cuts, by means of an elliptical cut formed by the 2σ contour of a two-dimensional Gaussian fit. (b) ROI energy spectrum for a series of cuts, demonstrating the near-negligible impact of applying data quality (DQ) cuts after the minimal cuts. (c) Fitted time profile of ^{125}I rates during SR1, with neutron activation due to a DD calibration period. The additional intermission window was caused by a circulation event, over which the detector purity temporarily decreased. For clarity, the error band only includes uncertainties in the getter removal half-life and the baseline rate.

SS events passing the minimal and elliptical cuts were divided into one-day bins according to their registered trigger timestamps, with the rate calculated in each bin taking the 80.11% capture fraction and the DAQ dead time into account. The time profile of ^{125}I over the course of SR1 is presented in Figure 5.5 (c), with a pronounced spike due to neutron activation following a $\sim$4.5 d calibration campaign with the DD generator. To model the behaviour of rates in the post-

DD period, the number of ^{125}I atoms at a given time $N_{^{125}\text{I}}(t)$ was described by a differential equation:

$$\frac{dN_{^{125}\text{I}}(t)}{dt} = \lambda_{^{125}\text{Xe}} N_{^{125}\text{Xe}}(t) - \left(\lambda_{^{125}\text{I}} + \lambda_g\right) N_{^{125}\text{I}}(t), \tag{5.9}$$

in which the positive term represents the production of ^{125}I from the decay of ^{125}Xe, and λ_g denotes the getter removal component of the effective decay constant, defined as $\lambda_{\text{eff}} = (\lambda_{^{125}\text{I}} + \lambda_g)$. This equation is solved by a function of the form

$$\begin{aligned} N_{^{125}\text{I}}(t) = N_{^{125}\text{Xe}}(t_0) &\frac{\lambda_{^{125}\text{Xe}}}{\lambda_{\text{eff}} - \lambda_{^{125}\text{Xe}}} \left(e^{-\lambda_{^{125}\text{Xe}} t} - e^{-\lambda_{\text{eff}} t}\right) && \text{(production term)} \\ &+ N_{^{125}\text{I}}(t_0) e^{-\lambda_{\text{eff}} t} && \text{(decay term)} \\ &+ b, && \text{(baseline term)} \end{aligned} \tag{5.10}$$

where t_0 is defined as the point at which the neutron source is removed, and hence no additional ^{125}Xe atoms are produced. A fit of Equation 5.10 to the post-DD period, as depicted in Figure 5.5 (c), yields $N_{^{125}\text{Xe}}(t_0) = (9.1 \pm 3.6) \times 10^4$ atoms and $N_{^{125}\text{I}}(t_0) = (6.1 \pm 4.5) \times 10^4$ atoms, along with a getter removal half-life of

$$t^g_{1/2} = (3.6 \pm 0.2)\,\text{d}, \tag{5.11}$$

which translates into an effective ^{125}I half-life of $t^{\text{eff}}_{1/2} = (3.4 \pm 0.2)\,\text{d}$ with the natural decay component included. For reference, LUX and XENON1T reported values of (3.7 ± 0.3) d and (4.6 ± 1.6) d for $t^g_{1/2}$, respectively [268, 274]. In each case, the corresponding getter removal time constant was consistent with the interval for xenon to flow through one cycle of the circulation system.

In general, the baseline rate was expected to consist of flat backgrounds, some contamination from the 2νKK mode of ^{124}Xe, and a very small amount of ^{125}I from thermal neutron activation. However, a slight shift was observed between the pre-DD and post-DD baseline rates, from $(2.9 \pm 0.2) \times 10^{-3}$ counts/kg/d down to $(2.3 \pm 0.2) \times 10^{-3}$ counts/kg/d. This was attributed to a residual ^{125}I population in the pre-DD window, from activation during neutron calibrations performed a month prior to the start of SR1. With different circulation settings used in the physics commissioning period leading up to SR1, such as a higher flow rate through the getter, the ^{125}I removal efficiency was slightly lower and hence extended the preceding decay curve.

Depth migration

Since the ^{125}I removal time constant is comparable to the timescale of one circulation cycle, inhomogeneities can occur for the distribution of this background in z as there is insufficient time to establish a mixed state. This is shown in Figure 5.6 for events passing the set of minimal and elliptical cuts, along with their average z position over time. Calibration source neutrons are delivered to the TPC through a conduit connected to the upper third of the cryostat, and the activated xenon subsequently returns to the purification circuit by spilling over three weirs around the liquid surface. Therefore, disproportionately more ^{125}I decays are observed towards the bottom, where circulated xenon re-enters via inlets in the TPC and skin. This is evident in the biased average z values immediately following the DD calibrations. As ^{124}Xe events should be homogeneously distributed in position, this behaviour offers an additional route for identifying background-like events.

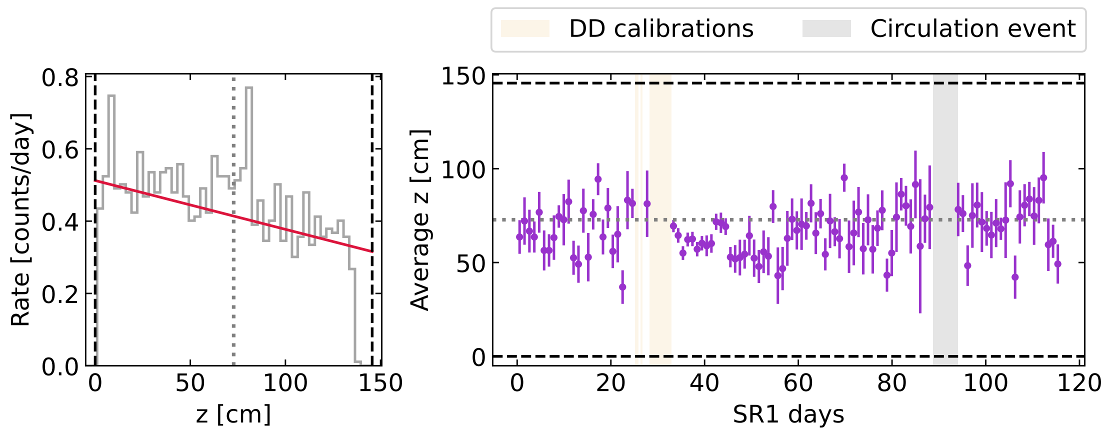

Figure 5.6: Distribution of all z positions with a guiding linear fit (left) and the average z position over time (right), for events passing the minimal and elliptical cuts. The active volume boundaries are indicated by black dashed lines, and the vertical centre of the TPC is marked with a grey dotted line for reference.

Activation model

In order to verify activation estimates from the fit of Equation 5.10, and hence model the amount of ^{125}I background more confidently, the neutron activation rate of ^{124}Xe into ^{125}Xe was constrained with DD calibration data. As different trigger conditions were set for the DD runs, it was necessary to measure the trigger efficiencies in DD data with respect to background data first. For this purpose, the 380.2 keV and 408.2 keV pair of ^{127}Xe peaks were utilised, which occur from the coincidence of a 375.0 keV gamma ray and either a 5.2 keV L-shell or a 33.2 keV K-shell cascade in the decay of ^{127}Xe by EC. In addition to providing a relatively clean selection, these peaks are situated in the same energy region as ^{125}Xe peaks, which are ultimately used to obtain the activation rate.

The rate of ^{127}Xe over time was tracked by fitting a double-Gaussian function plus a linear background to the pair of peaks within one-day bins, in the same manner as for the ^{125}I population discussed previously. As demonstrated in Figure 5.7, the ^{127}Xe rate was then extrapolated into the DD window by means of an exponential decay fit to background data, with the half-life fixed at the literature value of 36.3 d [224]. This approximation is valid within the DD calibration window as the impact of neutron activation on the amount of ^{127}Xe is negligible, due to the large proportion of pre-existing ^{127}Xe, along with the low natural abundance of ^{126}Xe at $(0.0890 \pm 0.0002)\%$ [246], on which neutron capture can produce ^{127}Xe. Therefore, the efficiency of each DD trigger type was extracted by taking the ratios of ^{127}Xe rates in DD data to those predicted by the exponential curve, and then averaging:

$$\epsilon_{\mathrm{DD}}^{\mathrm{S2}} = (88.6 \pm 6.1)\,\%, \tag{5.12}$$

$$\epsilon_{\mathrm{DD}}^{\mathrm{plasma}} = (20.5 \pm 3.3)\,\%, \tag{5.13}$$

with standard errors taken as the uncertainties.

To measure the activation rate, the prominent 276.6 keV peak from the decay of ^{125}Xe by EC was chosen. This is composed of a 243.4 keV gamma ray emitted by

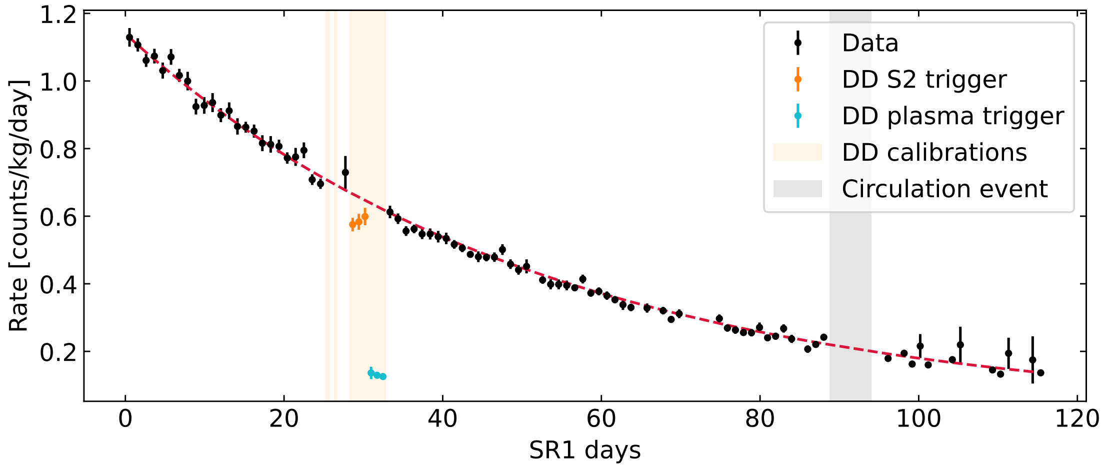

Figure 5.7: Rates of ^{127}Xe in the FV over time, with equivalent values for DD calibration data. Each bin is normalised by the DAQ live time, hence the rates within the DD window are different primarily due to the change in trigger settings. A few points where the double-Gaussian fits failed to converge were excluded, mainly towards the end of SR1 where there are lower statistics. A red dashed curve marks the exponential fit to background data.

the ^{125}I daughter with a 32.4% branching ratio [283], alongside a 33.2 keV cascade from the K-shell vacancy with an 88.4% capture probability [284]. In addition to these branching factors, it was important to consider the fact that ^{125}Xe decays can produce MS events as well. This was accounted for with a measured SS fraction of $(55.2 \pm 7.1)\%$ for the 276.6 keV peak, which is consistent with the value of $(57.8 \pm 0.1)\%$ from ^{125}Xe simulations. Since the calibration source neutrons only irradiated the top third of the TPC, events were restricted to a small cylindrical volume with a radius of 68.8 cm and height limits of $(99.7\,\text{cm} \leq z \leq 132.4\,\text{cm})$.

To illustrate the ^{125}Xe population growth due to neutron activation, the rate over time is illustrated in Figure 5.8 (a), with the trigger efficiencies compensated for. Due to the instability of measurements with the DD plasma trigger, only runs utilising the DD S2 trigger were considered, with a DAQ live time of 2.1 d. Therefore, with corrections for the branching factors, SS fraction, and trigger efficiencies, the fitted 276.6 keV peak as in Figure 5.8 (b) yielded an activation rate of

$$A_n = (15.2 \pm 3.4)\,\text{atoms/kg/d}. \tag{5.14}$$

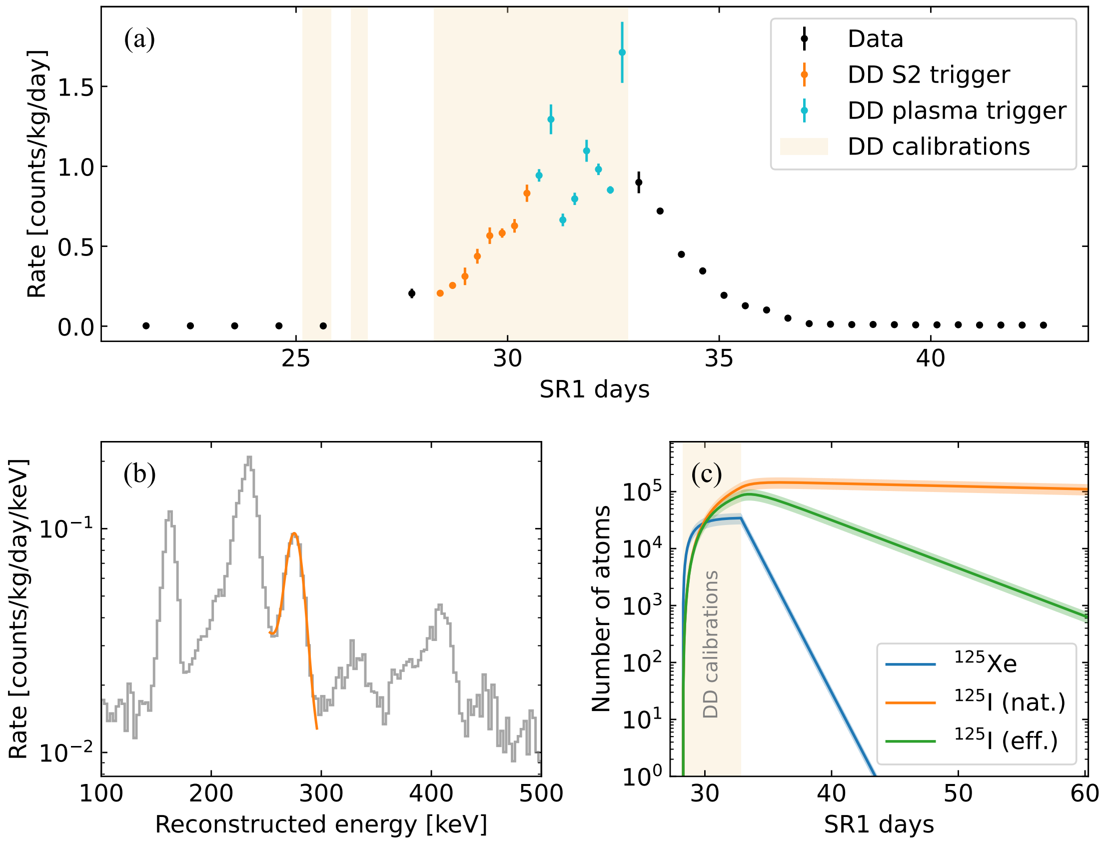

Figure 5.8: Formulation of the ^{124}Xe neutron activation model. (a) The rate of ^{125}Xe decays through the DD calibration window, with trigger efficiencies factored into data points from DD runs. (b) Fit of the 276.6 keV ^{125}Xe peak with a Gaussian plus a linear background, for events from DD S2 trigger runs occurring within a cylindrical volume in the upper third of the TPC, which receives most of the calibration source neutrons. (c) A model of the number of ^{125}Xe and ^{125}I atoms over time, with A_n set to zero beyond the DD calibration period. For reference, both of the natural and effective (natural plus getter removal) decay schemes of ^{125}I are included.

As such, applying this to the top third of the TPC in conjunction with Equation 5.10, the resulting activation model is displayed in Figure 5.8 (c). This predicts the following values for the number of atoms at the start of the post-DD window:

$$N_{^{125}\mathrm{Xe}}(t_0) = (3.4 \pm 0.8) \times 10^4 \,\text{atoms} \quad \text{and} \quad N_{^{125}\mathrm{I}}(t_0) = (8.5 \pm 1.9) \times 10^4 \,\text{atoms}.$$

Although these estimates are relatively close to those generated by the fit of Equation 5.10 to ^{125}I, the activation model implies that $N_{^{125}\mathrm{I}}(t_0) > N_{^{125}\mathrm{Xe}}(t_0)$, in contrast to what is measured. During the calibration period, the DD S2 trigger was used for a mode in which (2450 ± 20) keV neutrons were fired directly into the conduit, whereas the DD plasma trigger was tuned to match the high intensity D-reflector and H-reflector modes, where neutrons were scattered off a deuterium-based or hydrogen-based target to produce 272–400 keV or $\leq$100 keV neutrons, respectively [204]. As ^{124}Xe has a higher capture cross section for lower energy neutrons, it is likely that solely considering the DD S2 trigger points led to an underestimate in the number of ^{125}Xe atoms in the activation model [285, 286].

A minor amount of activation can also occur with ambient thermal neutrons originating from the cavern rock structure surrounding the LZ detector, which contributes to the baseline rate observed in Figure 5.5 (c). The thermal neutron activation rate A_t can be expressed as

$$A_t = \left(\frac{\eta N_A M_{\mathrm{Xe}}}{M_A}\right) \sigma_n \phi_n, \tag{5.15}$$

where $\sigma_n = (165 \pm 11) \times 10^{-24}\,\mathrm{cm}^2$ is the thermal neutron capture cross section for ^{124}Xe [287], $\phi_n = (1.7 \pm 0.2) \times 10^{-6}/\mathrm{cm}^2/\mathrm{s}$ is the thermal neutron flux in the Davis Cavern at SURF [288], and the factor contained in the brackets represents the number of ^{124}Xe atoms in a xenon mass of M_{Xe}, with the other terms defined as in Equation 5.2. Although a vast majority of the LZ xenon inventory is contained within the detector, shielded from ambient radiation by the water tank, a small portion is exposed when in circulation. At a given time, a substantial amount of this is held in the xenon tower, where xenon is evaporated and condensed as it flows from and to the detector; this is approximated as $M_{\mathrm{Xe}} = (70 \pm 10)\,\mathrm{kg}$, which leads to a value of $A_t = (7.4 \pm 1.5)\,\mathrm{atoms/d}$. Accounting for removal by the getter, this can be translated into an event rate R_t by

$$R_t = A_t \frac{\lambda_{^{125}\mathrm{I}}}{\lambda_{^{125}\mathrm{I}} + \lambda_g}, \tag{5.16}$$

which therefore predicts a ^{125}I rate of $R_t = (0.5 \pm 0.1)\,\mathrm{counts/d}$ originating from thermal neutron activation. Since this contributes $<4\%$ of the baseline rate in Figure 5.5 (c), it is taken as a negligible effect.

5.5 Fit procedure

The background contributions were constrained along with the ^{124}Xe signal activity by fitting simulated energy spectra to data, which leveraged the same high-statistics simulations as those produced by the parametric chain for the work in Chapter 4. For simplicity, reconstructed energy was selected as the fit observable since both the signals and backgrounds produce ERs, and hence $(\mathrm{S1c}, \mathrm{S2c_{bot}})$ space offers no additional discrimination power.

Fits were performed according to a binned maximum likelihood approach as described in Section 4.6.1, using the same implementation and form for the log-likelihood defined in Equation 4.9, repeated here for completeness:

$$\begin{aligned}\ln \mathcal{L}(\boldsymbol{d}|\boldsymbol{\theta}, \boldsymbol{\mu}, \boldsymbol{\sigma}) = &\sum_{i=1}^{N_b} d_i \ln f_i(\boldsymbol{\theta}) && \text{(model term)} \\ &- \nu(\boldsymbol{\theta}) && \text{(extended term)} \\ &- \sum_{k=1}^{N_c} \frac{1}{2}\left(\frac{\theta_k - \mu_k}{\sigma_k}\right)^2 && \text{(Gaussian constraint term)} \qquad (5.17)\end{aligned}$$

where the energy spectra are divided into N_b bins, with d_i observed counts and $f_i(\boldsymbol{\theta})$ expected counts in the ith bin. For each of N_c components, there is an associated energy PDF p_j scaled by a corresponding model parameter θ_j, which comprise $f_i(\boldsymbol{\theta}) = \sum_{j=1}^{N_c} \theta_j p_{ji}$. The model parameters $\boldsymbol{\theta}$ are regularised by a Gaussian constraint term, which penalises significant deviations from the initial estimates of the counts $\boldsymbol{\mu}$ with uncertainties $\boldsymbol{\sigma}$ provided by sideband analyses, as listed in Table 5.2. The extended Poisson term $\nu(\boldsymbol{\theta}) = \sum_{i=1}^{N_b} f_i(\boldsymbol{\theta})$ serves to include information from the observed sample size $n = \sum_{i=1}^{N_b} d_i$.

Furthermore, the goodness-of-fit was evaluated with the Poisson-likelihood χ^2_λ test statistic noted in Equation 4.10:

$$\chi^2_\lambda = 2\sum_{i=1}^{N_b}\left(d_i \ln \frac{d_i}{f_i(\hat{\boldsymbol{\theta}})} + f_i(\hat{\boldsymbol{\theta}}) - d_i\right), \qquad (5.18)$$

which obeys a χ^2 distribution with $N_b - N_c$ degrees of freedom [259, 260].

Taking into account the DAQ dead time as well as the exclusion of periods with anomalous trigger rates and deployed calibration sources, the SR1 dataset consisted of 89.6 live days, with 22.0 d and 67.6 d as part of the pre-DD and post-DD windows, respectively. With the assumption of natural isotopic abundance, this corresponds to an isotopic exposure of 1.3 kg × y for the poly-wall FV.

The inflated amount of ^{125}I immediately following the DD calibrations motivates the definition of a post-DD exclusion period, which presents a trade-off between high background rates and exposure. To operate with $< 99\%$ of the peak ^{125}I rate, the size of this exclusion window must be ≥ 23.7 d, equivalent to at least 7.4 effective half-lives. However, proceeding with the standard fit procedure, the resulting ^{124}Xe activity displayed a strong dependence on the length of the exclusion period. This was likely to have been caused by background contamination, with a higher signal activity obtained for shorter exclusion windows. To overcome this, alternative methods were devised in which the time-dependence of background rates is included in the model:

- **Simultaneous fit** – as opposed to regarding SR1 as a single dataset, it can be split into pre-DD and post-DD subsets $(\boldsymbol{d}_A, \boldsymbol{d}_B)$. This allows for the treatment of backgrounds affected by the DD calibrations as separate components, and hence enables the assertion of tighter constraints as informed by the activation model. To maintain continuity between the two subsets for sources with constant rates, including the signal term, they must be fit simultaneously by maximising the sum of two log-likelihoods akin to

$$\ln \mathcal{L}(\boldsymbol{d}_A, \boldsymbol{d}_B | \boldsymbol{\theta}, \boldsymbol{\eta}_A, \boldsymbol{\eta}_B) = \ln \mathcal{L}(\boldsymbol{d}_A | \boldsymbol{\theta}, \boldsymbol{\eta}_A) + \ln \mathcal{L}(\boldsymbol{d}_B | \boldsymbol{\theta}, \boldsymbol{\eta}_B), \tag{5.19}$$

  where $\boldsymbol{\theta}$ denotes model parameters shared between the two datasets, and $(\boldsymbol{\eta}_A, \boldsymbol{\eta}_B)$ contain pre-DD and post-DD parameters for each time-varying background. A benefit to this approach is that it is relatively straightforward to incorporate additional datasets into the fit, such as pre-SR2 detector monitoring runs and SR2 background runs.

- **Explicit time-dependence** – a more complicated but comprehensive alternative is to explicitly include time dependence in the form of live time PDFs t_j with N_t bins. The height of each bin would represent the fraction of the total expected counts at a given time, and the overall shape of the PDF would be dictated by the half-life or expected behaviour of each component. This would imply a new definition for the expected counts in each energy bin:

$$f_{mi}(\boldsymbol{\theta}) = \sum_{j=1}^{N_c} \theta_j t_{mj} p_{ji}, \tag{5.20}$$

  where the original version of $f_i(\boldsymbol{\theta})$ is recovered by performing the sum over the time bin index m. Similarly, the observed counts $\boldsymbol{d}$ would be split into m parts. This procedure is effectively an extension of the simultaneous fit method up to a sum of N_t log-likelihoods, with a model term of the form

$$\ln \mathcal{L}(\boldsymbol{d}|\boldsymbol{\theta})_{\text{model}} = \sum_{m=1}^{N_t} \sum_{i=1}^{N_b} d_{mi} \ln f_{mi}(\boldsymbol{\theta}). \tag{5.21}$$

On the timescale of SR1, ^{125}I and ^{133}Xe rates experience the greatest variation within the ROI; the time profiles of all other sources would be uniform, with the exception of ^{127}Xe. As such, the implementation of explicit time dependence would provide limited benefit, and thus the simultaneous fit approach was adopted. With ^{212}Pb and material contributions fixed due as they are comparatively subdominant, the fit involved a total of 10 parameters: 6 shared between the two likelihoods, along a pair for pre-DD and post-DD parameters of ^{125}I and ^{133}Xe. Whereas initial estimates for the ^{133}Xe parameters—as well as the shared parameters—were derived from the results of xenon activation studies [248], those of ^{125}I were determined using the measurements made in Section 5.4.1. The pre-DD rate was approximated as $(2.5 \pm 0.2) \times 10^{-3}$ counts/kg/d from the mean of the flat baseline at the start of SR1, with the standard error taken as the uncertainty. On the other hand, the average post-DD rate of $(4.7 \pm 0.8) \times 10^{-3}$ counts/kg/d was estimated by normalising the integral of the exponential decay curve by the live time, and equivalently for the error bands to obtain the uncertainty. These values account for the 80.11% branching ratio in the ^{125}I population selection, as well as some contamination from 2νKK with an estimated rate of $(5.3 \pm 1.4) \times 10^{-4}$ counts/kg/d.

5.6 Results and discussion

The outcome of the simultaneous fit of the pre-DD and post-DD subsets is presented in Figure 5.9. Along with the low values of reduced χ^2_λ, the residuals are indicative of a high-quality fit, with the most significant differences occurring in the low-statistics regions between features. Moreover, to probe the relationship between the best-fit values $\hat{\boldsymbol{\theta}}$ and the constraints, a plot of parameter pulls $(\hat{\boldsymbol{\theta}}-\boldsymbol{\mu})/\boldsymbol{\sigma}$ is displayed in Figure 5.10. This demonstrates that no significant deviations from the initial expectations are observed, with fixed sources excluded and the signal term omitted as it was left unconstrained. However, most pulls exhibit a negative directionality, suggesting that the initial values $\boldsymbol{\mu}$ were generally slightly overestimated.

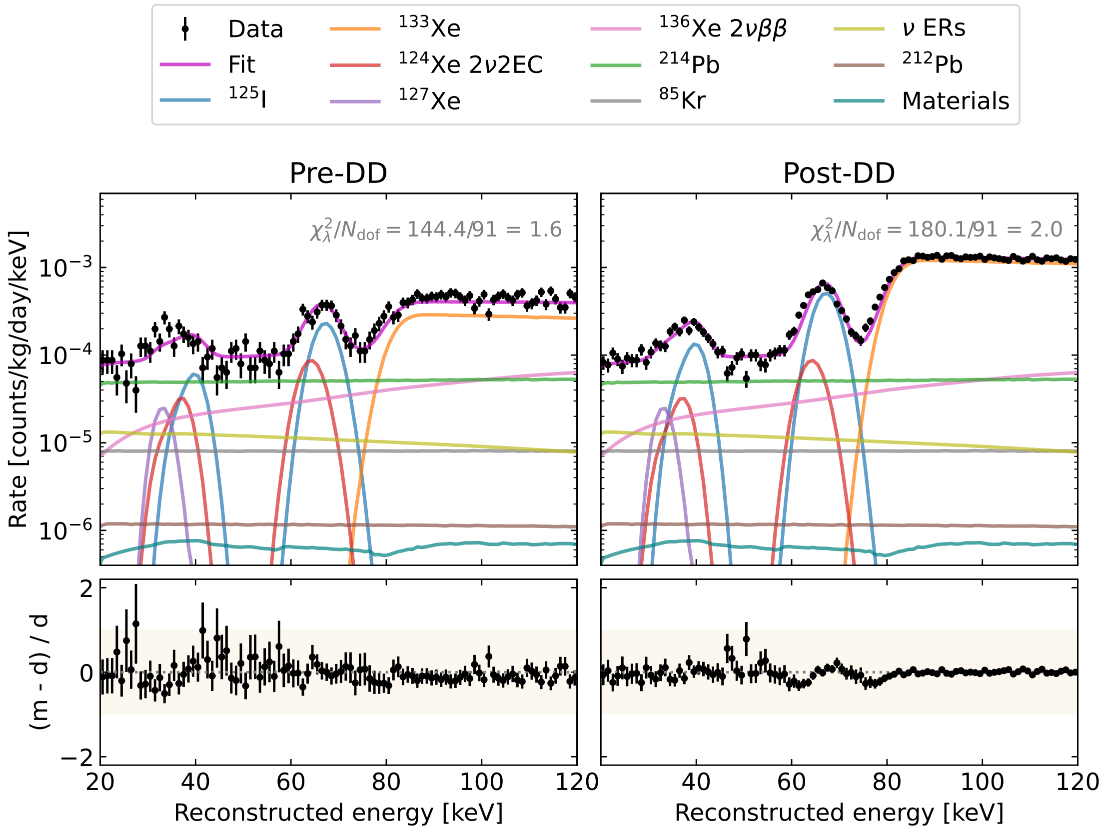

Figure 5.9: Simultaenous fit of pre-DD and post-DD subsets of SR1, for SS events in the ROI with the minimal set of cuts applied. Both ^{212}Pb and the detector material contributions were fixed as they are subdominant. Since the materials component is a sum of many low-rate lines, a smoothing filter was applied for clarity. Fractional differences between the fitted models $\boldsymbol{m}$ and the data $\boldsymbol{d}$ are added as residual plots to visualise the fit quality.

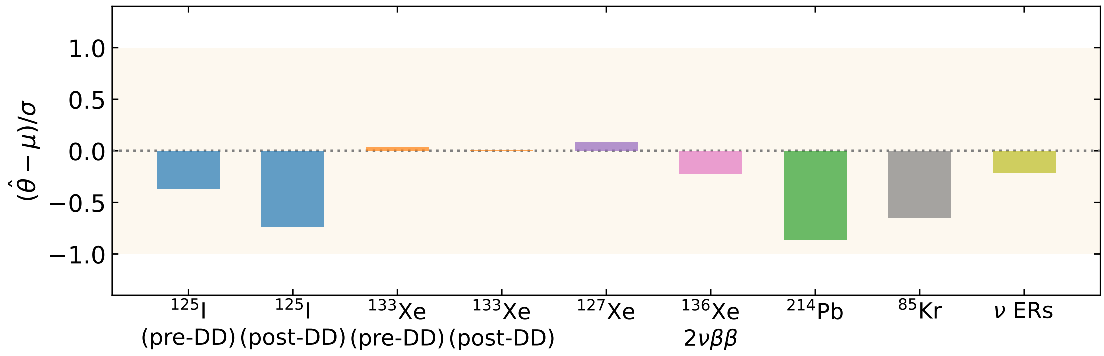

Figure 5.10: Parameter pulls for the simultaneous fit of pre-DD and post-DD periods. The unconstrained signal term is excluded, along with those associated with the fixed ^{212}Pb and material components. The band signifies a $\pm 1\sigma$ tolerance.

To verify that the time dependence of background sources was appropriately captured by the fitted model, the best-fit values for the average rates were converted into pre-DD and post-DD starting rates using the known half-lives, and projected in time. As shown in Figure 5.11, the model is in agreement with the data overall, with a minor departure in the post-DD baseline. The error band was calculated from the parameter errors estimated by `iminuit`, which are extracted using a numerical approximation of the inverse Hessian [261].

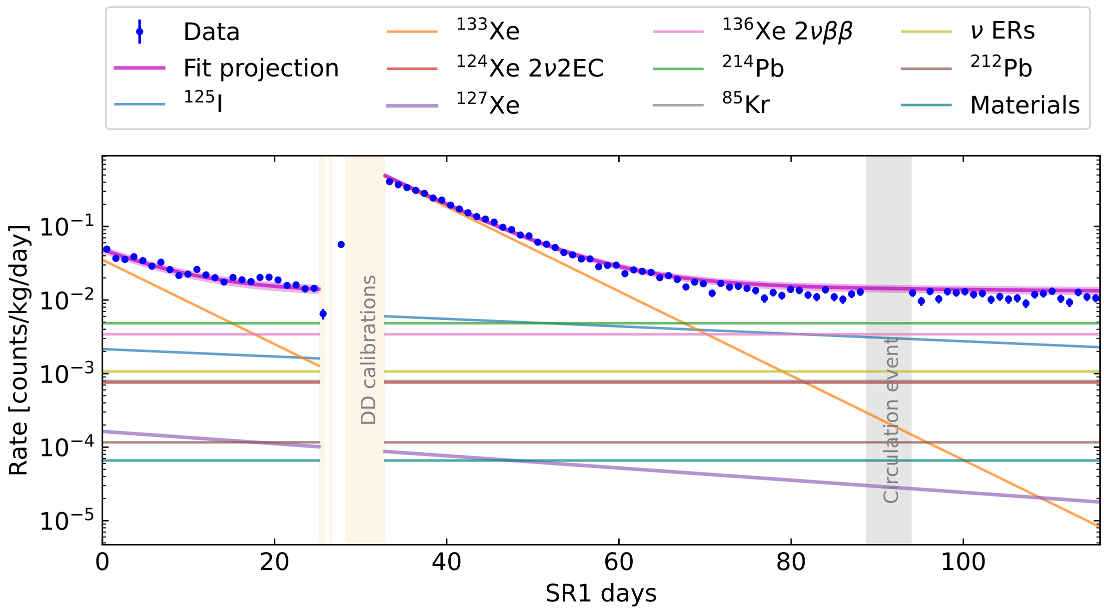

Figure 5.11: Time projection of the fitted rates overlaid onto SR1 data, for SS events in the ROI with the minimal set of cuts applied. Aside from ^{125}I, ^{133}Xe, and ^{127}Xe, sources were modelled with uniform rates over the entire course of SR1.

With a best-fit activity of $A_{2\nu2\text{EC}} = (0.28 \pm 0.04)\,\text{counts/kg/y}$, Equation 5.2 can be used to infer the half-life:

$$T_{1/2}^{2\nu2\text{EC}} = (1.09 \pm 0.18_{\text{stat}} \pm 0.03_{\text{sys}}) \times 10^{22}\,\text{years}, \tag{5.22}$$

which is remarkably close to the result of $(1.1 \pm 0.2_{\text{stat}} \pm 0.1_{\text{sys}}) \times 10^{22}$ years reported by XENON1T [268]. A breakdown of the systematic uncertainties is given in Table 5.4. Although the simultaneous fit procedure dramatically reduced the dependence on the length of a post-DD exclusion period, a small amount of bias remains as shown in Figure 5.12. This forms the largest contribution to the systematic uncertainty, taken as the highest absolute difference in half-life over the considered range of exclusion window sizes. Secondary sources of uncertainty stem from the energy reconstruction parameters $g_1 = (0.114 \pm 0.002)$ phd/photon and $g_2^{\text{bot}} = (15.1 \pm 0.4)$ phd/electron as calibrated for the WIMP search, as well as the live time (89.6 ± 1.0) d. As XENON1T observed a higher ^{124}Xe abundance than that of natural xenon, it is possible that this contribution to the systematic uncertainty is subject to change with upcoming measurements of the isotopic abundance in LZ.

Table 5.4: Summary of the systematic uncertainties on the ^{124}Xe 2ν2EC half-life, with the total calculated by summing the individual contributions in quadrature.

Contribution	Uncertainty [10^{22} y]	Relative uncertainty [%]
Exclusion period	0.03	2.8
Energy reconstruction	0.012	1.1
Live time	0.011	1.0
Fiducial mass	0.005	0.5
^{124}Xe abundance	0.003	0.3
Total	0.03	5.7

Since the χ^2_λ statistic was formulated with a likelihood ratio, the significance for a given hypothesis test can be approximated by taking $\sqrt{\chi^2_\lambda}$ [289]. A statistic which tests the signal-plus-background hypothesis against the background-only hypothesis may be constructed by taking the difference between the two corresponding

χ^2_λ expressions. Therefore, the discovery significance for the half-life measurement can be calculated according to

$$\sqrt{\Delta\chi^2_\lambda} = \sqrt{\chi^2_\lambda(\hat{\boldsymbol{\theta}}_0) - \chi^2_\lambda(\hat{\boldsymbol{\theta}})}, \tag{5.23}$$

where the first term represents the background-only case, in which the maximum likelihood estimators $\hat{\boldsymbol{\theta}}_0$ are obtained by performing a fit with the signal term set to zero, and the second term contains a non-zero signal term as normally considered. By repeating the fit with the signal activity fixed at a range of sampled values, a $\Delta\chi^2_\lambda$ profile was generated as depicted in Figure 5.12. The minimum coincides with the best-fit value for a non-zero signal term, whereas the $\Delta\chi^2_\lambda$ value at an activity of zero corresponds to the background-only scenario. The difference between these two scenarios thus yields a significance of 7σ.

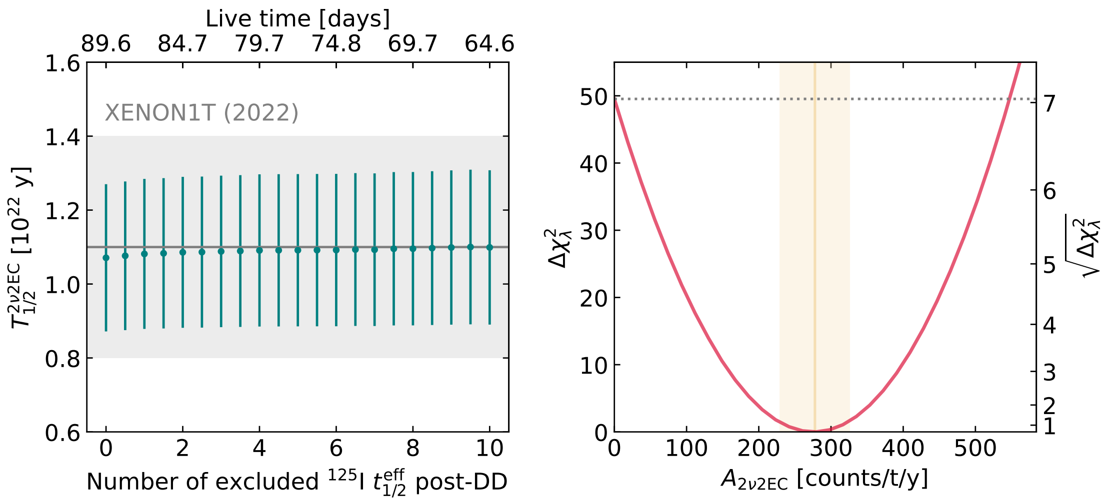

Figure 5.12: Outcomes for the half-life measurement over a range of post-DD exclusion periods, with the XENON1T result highlighted in grey (left); the $\Delta\chi^2_\lambda$ profile as a function of fixed values of the signal activity, with the best-fit activity marked by a vertical line and uncertainty band (right). For clarity, the profile amplitudes were subtracted such that the minimum is at a $\Delta\chi^2_\lambda$ value of zero.

In order to attempt a measurement of the relative capture fractions, the signal model was deconstructed into individual Gaussian peaks, as per Figure 5.1. This adds three more signal terms to the likelihood expression, all of which were initialised with the expected proportions and left unconstrained. The result of this fit is showcased in Figure 5.13, with comparisons between the modelled and measured capture fractions summarised in Table 5.5. Despite being in good agreement with the XENON1T signal model, large error bars are attached to these values due to the limited statistics provided by SR1. With upcoming science runs in LZ, the influx of more data will enable more confident extensions to this measurement.

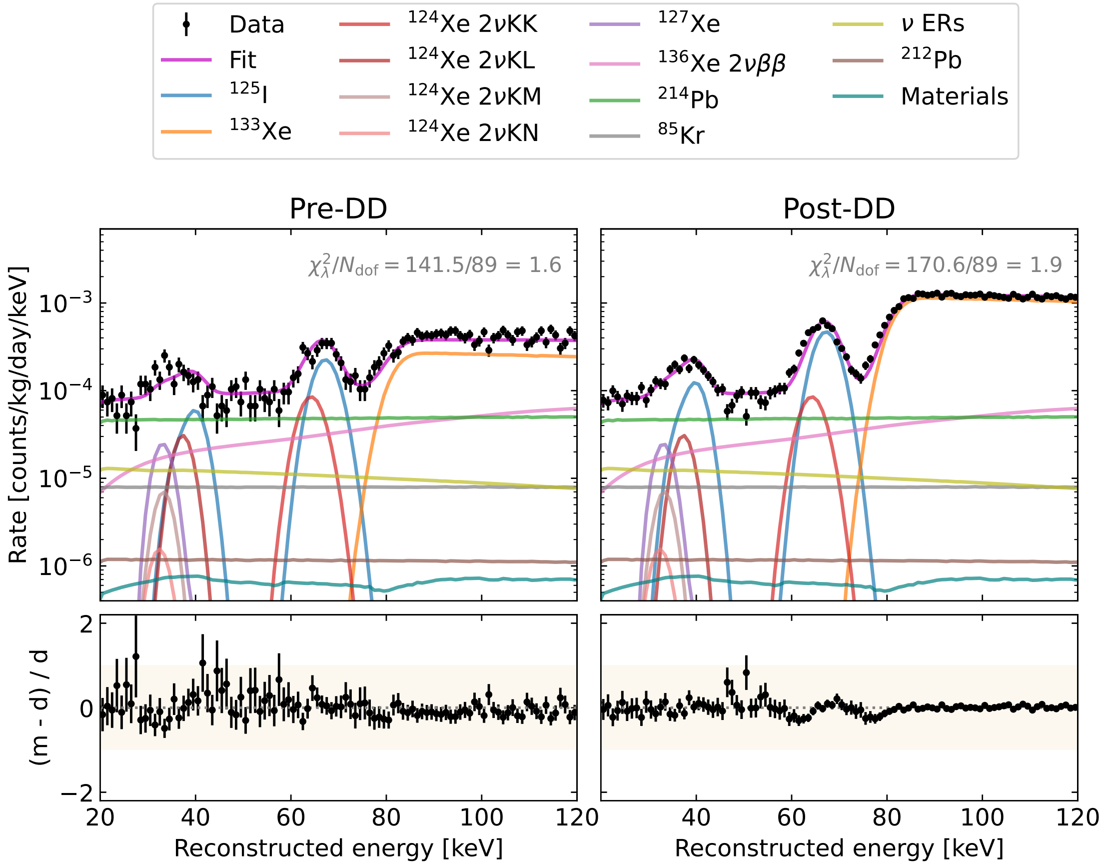

Figure 5.13: Alternative version of the simultaneous fit, with the ^{124}Xe signal broken down into four Gaussian peaks representing each EC combination. The capture fractions were extracted from the relative proportions of each activity.

Table 5.5: Comparisons between measured capture fractions and those predicted by the XENON1T model, for the four most dominant capture combinations.

Decay mode	Model fraction [%]	Measured faction [%]
KK	72.4	(72.6 ± 11.4)
KL	20.0	(19.9 ± 3.3)
KM	4.3	(4.3 ± 0.7)
KN	1.0	(1.0 ± 0.2)

The measured half-life is compared with recent predictions from different theoretical frameworks and lower limits set by other experiments in Figure 5.14. The result obtained in this work is compatible with effective theory (ET) and large-scale nuclear shell model (NSM) calculations [290], and is in agreement with those from the quasiparticle random-phase approximation (QRPA) [269, 291] approach at the 2σ level. Moreover, this measurement is also consistent with the 90% confidence level lower limits set by XENON100 [292] and LUX [274]. Although a discrepancy is observed with respect to the limit produced by XMASS [293], this was attributed to ineffective removal of the dominant ^{125}I background by their purification system, combined with a higher thermal neutron flux in the Kamioka mine and a substandard energy resolution.

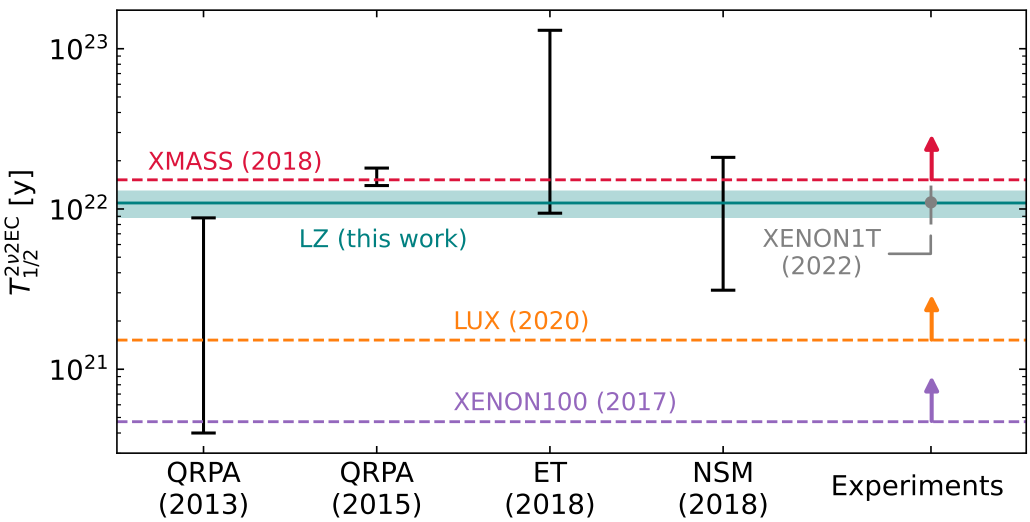

Figure 5.14: Comparison of the measured half-life with theoretical predictions represented by black bars and experimental lower limits indicated by dashed lines. For instances where the reported half-life is for the KK capture mode, the value is scaled by the 72.4% capture fraction. The result obtained in this work is depicted as a solid horizontal line with a $\pm 1\sigma$ combined statistical and systematic uncertainty band, which aligns with the XENON1T result shown in grey.

Future runs in LZ will facilitate tighter experimental constraints on the half-life and relative capture fraction for NME calculations; independent measurements of the 2νKL and 2νLL modes would allow the decoupling of NMEs from phase space factors. Applying the best-fit activity, an estimated total of (394±57) 2ν2EC events were observed within the SR1 dataset, which translates to ∼4400 events over the nominal LZ exposure of 1000 live days. Over such a timescale, direct measurements of ^{124}Xe decays via $2\nu\mathrm{EC}\beta^+$ will be within reach, presenting approximately ∼400 events for a predicted half-life of $(1.7 \pm 0.6) \times 10^{23}$ years [270].

5.7 Conclusion

A first measurement of the extremely rare Standard Model decay of ^{124}Xe by 2ν2EC was performed in LZ using an SR1 dataset with a total of 89.6 live days, yielding a half-life of $T_{1/2}^{2\nu 2\mathrm{EC}} = (1.09 \pm 0.18_{\mathrm{stat}} \pm 0.03_{\mathrm{sys}}) \times 10^{22}$ years with a statistical significance of 7σ. In addition, an early attempt at constraining the relative capture fractions for different shell combinations yielded values consistent with the signal model developed by XENON1T.

The exposure—and hence the sensitivity—was maximised through the optimisation of a specialised FV, for which detector material backgrounds at the TPC wall were the limiting factor. An overall 4% increase in fiducial mass was achieved with respect to the SR1 FV definition. In addition, thorough studies of ^{125}I production via neutron activation and its removal by the LZ purification system were conducted, as it forms the main background to this search. The rate of xenon activation in the presence of a DD neutron calibration source was estimated at $A_n = (15.2 \pm 3.4)$ atoms/kg/d. Predictions for the number of ^{125}I atoms produced was consistent with estimates from a fit of ^{125}I rates over the course of SR1. Moreover, the getter removal component of the ^{125}I half-life was measured at (3.6 ± 0.2) d – drastically lower than the natural 59.4 d half-life.

Constraining the rate of ^{124}Xe decays in LZ is critical as it contributes a background to a variety of low energy searches, including WIMPs and light dark matter candidates. Furthermore, this measurement opens new avenues for the detection or limit-setting of even rarer decay modes in upcoming science runs, namely $2\nu\mathrm{EC}\beta^+$, as well as the more exotic neutrinoless modes [270].

Conclusions and outlook

With an unprecedented sensitivity to WIMPs, the LZ experiment has recently set a world-leading limit on WIMP-nucleon interactions from its first science run. As the dual-phase xenon TPC technology employed in LZ is highly versatile, the detector also has the capacity to probe various other interesting phenomena. The focus of the work presented in this thesis has been on leveraging this to expand the scientific programme to rare interactions beyond the primary WIMP search.

For one, there is the $0\nu\beta\beta$ decay of ^{136}Xe – the observation of which would confirm the existence of massive Majorana particles and lepton number violation. LZ is set to make a measurement of this that is competitive with dedicated experiments, which use xenon with isotopic enrichment. The success of such a measurement is critically underpinned by comprehensive modelling of the dominant backgrounds originating from detector materials. As detailed in Chapter 4, the construction of this background model utilised the results of an extensive radioassay campaign, as well as a large-scale simulations production. The activities of naturally occurring radioactive materials and anthropogenic isotopes in numerous detector components were constrained through fits of simulated energy spectra to SR1 data. A novel approach was developed to reduce the high level of complexity associated with this, which involved conducting fits within a series of detector sub-volumes, paired with a specialised component grouping algorithm. To improve the fit robustness, a modified energy calibration extending up to 3 MeV was performed, and corrections were implemented to optimise the energy reconstruction and resolution in both simulations and data. Although most fitted activities remained consistent with assay measurements, an overall increase in rates was observed and discussed. The implications for the sensitivity to $0\nu\beta\beta$ decays of ^{136}Xe were assessed, producing an updated projection for the median exclusion half-life at 0.98×10^{26} years for a nominal exposure of 1000 live days.

In the context of future experiments, such as the recent XLZD consortium, a larger detector size is part of the natural progression towards achieving a greater sensitivity. This is likely to incur a cost in the form of elevated detector ER backgrounds, which are especially important in the prospect of maintaining a competitive sensitivity to $0\nu\beta\beta$ decays. The capability of exploiting fine-grained assay measurements at the analysis stage, as demonstrated here for LZ, thus informs the requirements and procedures for future detectors. In addition, for the delivery of high statistics simulations in future experiments, the trade-off between realism and computational cost—as highlighted in this thesis—poses greater concerns in light of the growing climate crisis. Along with scientific and economic incentives, the implementation of simulation methods and computational infrastructure has the added obligation of reducing impact on the climate [294]. Recent developments in the field of machine learning, such as advanced generative techniques, offer means to produce realistic simulations more efficiently, with trained models that can often be repurposed [295].

The first LZ measurement of the decay of ^{124}Xe through $2\nu2$EC was presented in Chapter 5. The dominant ^{125}I background was constrained with an effective neutron activation model, as informed by studies of the removal efficiency of the online purification system. Moreover, a gain in exposure was achieved using an optimised FV, with methods that will be applicable to other analyses. A half-life of $T_{1/2}^{2\nu2\mathrm{EC}} = (1.09 \pm 0.18_{\mathrm{stat}} \pm 0.03_{\mathrm{sys}}) \times 10^{22}$ years was obtained with a statistical significance of 7σ, as well as the first measurements of the relative shell capture fractions. This result is consistent with recent experiments and theoretical predictions. With future science runs, tighter constraints on the capture fractions will be made, and the discovery of the more exotic $2\nu\mathrm{EC}\beta^+$ decay mode will be within reach.

References

[1] G. Bertone and D. Hooper, "History of dark matter", *Rev. Mod. Phys.*, vol. 90, p. 045 002, 2018.

[2] F. Zwicky, "Die Rotverschiebung von extragalaktischen Nebeln", *Helv. Phys. Acta*, vol. 6, pp. 110–127, 1933.

[3] F. Zwicky, "On the masses of nebulae and of clusters of nebulae", *Astrophys. J.*, vol. 86, p. 217, 1937.

[4] L. W. T. Kelvin, *Baltimore Lectures on Molecular Dynamics and the Wave Theory of Light*. CUP Archive, 1904.

[5] H. Poincaré, "The Milky Way and the theory of gases", *Pop. Astro.*, vol. 14, pp. 475–488, 1906.

[6] E. Öpik, "Selective absorption of light in space, and the dynamics of the Universe", *Bull. de la Soc. Astr. de Russie*, vol. 21, no. 150, p. 5, 1915.

[7] J. C. Kapteyn, "First attempt at a theory of the arrangement and motion of the sidereal system", *Astrophys. J.*, vol. 55, p. 302, 1922.

[8] J. H. Oort, "The force exerted by the stellar system in the direction perpendicular to the galactic plane and some related problems", *Bulletin of the Astronomical Institutes of the Netherlands*, vol. 6, p. 249, 1932.

[9] M. Schwarzschild, "Mass distribution and mass-luminosity ratio in galaxies", *Astron. J.*, vol. 59, p. 273, 1954.

[10] V. C. Rubin and W. K. Ford Jr., "Rotation of the Andromeda nebula from a spectroscopic survey of emission regions", *Astrophys. J.*, vol. 159, p. 379, 1970.

[11] M. S. Roberts, "A high-resolution 21-cm hydrogen-line survey of the Andromeda nebula", *Astrophys. J.*, vol. 144, p. 639, 1966.

[12] H. W. Babcock, "The rotation of the Andromeda Nebula", *Lick observatory bulletin*, vol. 19, pp. 41–51, 1939.

[13] D. H. Rogstad and G. S. Shostak, "Gross properties of five Scd galaxies as determined from 21-centimeter observations", *Astrophys. J.*, vol. 176, p. 315, 1972.

[14] A. Bosma, "The distribution and kinematics of neutral hydrogen in spiral galaxies of various morphological types", Ph.D. dissertation, Rijksuniversiteit te Groningen, 1978.

[15] V. C. Rubin, W. K. Ford Jr., and N. Thonnard, "Extended rotation curves of high-luminosity spiral galaxies. IV-Systematic dynamical properties, Sa→Sc", *Astrophys. J.*, vol. 225, pp. L107–L111, 1978.

[16] K. C. Freeman, "On the disks of spiral and S0 galaxies", *Astrophys. J.*, vol. 160, p. 811, 1970.

[17] S. M. Faber and J. S. Gallagher, "Masses and mass-to-light ratios of galaxies", *Annu. Rev. Astron. Astr.*, vol. 17, no. 1, pp. 135–187, 1979.

[18] J. P. Ostriker and P. J. E. Peebles, "A numerical study of the stability of flattened galaxies: or, can cold galaxies survive?", *Astrophys. J.*, vol. 186, pp. 467–480, 1973.

[19] J. Binney and S. Tremaine, "Chapter 9: Galaxy Formation", in *Galactic Dynamics*, 2nd ed., Princeton University Press, 2008.

[20] T. S. Van Albada *et al.*, "Distribution of dark matter in the spiral galaxy NGC 3198", *Astrophys. J.*, vol. 295, pp. 305–313, 1985.

[21] A. Einstein, "Lens-like action of a star by the deviation of light in the gravitational field", *Science*, vol. 84, no. 2188, pp. 506–507, 1936.

[22] H. Hoekstra *et al.*, "Masses of galaxy clusters from gravitational lensing", *Space Sci. Rev.*, vol. 177, pp. 75–118, 2013.

[23] R. Gavazzi *et al.*, "The sloan lens ACS survey. IV: the mass density profile of early-type galaxies out to 100 effective radii", *Astrophys. J.*, vol. 667, no. 1, p. 176, 2007.

[24] C. Chang *et al.*, "Dark Energy Survey Year 1 results: curved-sky weak lensing mass map", *Mon. Notices Royal Astron. Soc.*, vol. 475, no. 3, pp. 3165–3190, 2018.

[25] Q. Xia *et al.*, "A gravitational lensing detection of filamentary structures connecting luminous red galaxies", *Astron. & Astrophys.*, vol. 633, A89, 2020.

[26] M. Markevitch *et al.*, "Direct constraints on the dark matter self-interaction cross section from the merging galaxy cluster 1E0657–56", *Astrophys. J.*, vol. 606, no. 2, p. 819, 2004.

[27] D. Clowe *et al.*, "A direct empirical proof of the existence of dark matter", *Astrophys. J.*, vol. 648, no. 2, p. L109, 2006.

[28] H. R. Russell *et al.*, "Chandra observation of two shock fronts in the merging galaxy cluster Abell 2146", *Mon. Notices Royal Astron. Soc.*, vol. 406, no. 3, pp. 1721–1733, 2010.

[29] B. Ragozzine *et al.*, "Weak-lensing Results for the Merging Cluster A1758", *Astrophys. J.*, vol. 744, no. 2, p. 94, 2011.

[30] A. Liddle, "Chapter 10: The Cosmic Microwave Background", in *An Introduction to Modern Cosmology*, John Wiley & Sons, 2015.

[31] A. A. Penzias and R. W. Wilson, "A measurement of excess antenna temperature at 4080 Mc/s", *Astrophys. J.*, vol. 142, pp. 419–421, 1965.

[32] D. Eisenstein *et al.*, "Detection of the baryon acoustic peak in the large-scale correlation function of SDSS luminous red galaxies", *Astrophys. J.*, vol. 633, no. 2, p. 560, 2005.

[33] G. F. Smoot *et al.*, "Structure in the COBE differential microwave radiometer first-year maps", *Astrophys. J.*, vol. 396, pp. L1–L5, 1992.

[34] S. Dodelson and F. Schmidt, "Chapter 8: Anisotropies", in *Modern cosmology*, Academic Press, 2020.

[35] N. Aghanim *et al.* (Planck Collaboration), "Planck 2018 results. VI. Cosmological parameters", *Astron. & Astrophys.*, vol. 641, A6, 2020.

[36] W. Hu, N. Sugiyama, and J. Silk, "The physics of microwave background anisotropies", *Nature*, vol. 386, no. 6620, pp. 37–43, 1997.

[37] G. R. Blumenthal *et al.*, "Formation of galaxies and large-scale structure with cold dark matter", *Nature*, vol. 311, no. 5986, pp. 517–525, 1984.

[38] M. Davis *et al.*, "The evolution of large-scale structure in a universe dominated by cold dark matter", *Astrophys. J.*, vol. 292, pp. 371–394, 1985.

[39] C. S. Frenk and S. D. M. White, "Dark matter and cosmic structure", *Ann. Phys.*, vol. 524, no. 9-10, pp. 507–534, 2012.

[40] S. D. M. White and M. J. Rees, "Core condensation in heavy halos: a two-stage theory for galaxy formation and clustering", *Mon. Notices Royal Astron. Soc.*, vol. 183, no. 3, pp. 341–358, 1978.

[41] B. J. Richard, K. Lev, and P. Dmitri, "How filaments are woven into the cosmic web", *Nature*, vol. 380, pp. 603–606, 1996.

[42] L. A. Kofman, N. Y. Gnedin, and N. A. Bahcall, "Cosmological constant, COBE cosmic microwave background anisotropy, and large-scale clustering", *Astrophys. J.*, vol. 413, pp. 1–9, 1993.

[43] N. Aghanim *et al.* (Planck Collaboration), "Planck 2018 results. I. Overview and the cosmological legacy of Planck", *Astron. & Astrophys.*, vol. 641, A1, 2020.

[44] J. R. Gott III *et al.*, "A Map of the Universe", *Astrophys. J.*, vol. 624, no. 2, p. 463, 2005.

[45] E. Abdalla *et al.*, "Cosmology intertwined: A review of the particle physics, astrophysics, and cosmology associated with the cosmological tensions and anomalies", *J. High Energy Astrophys.*, vol. 34, pp. 49–211, 2022.

[46] A. Kosowsky, M. Milosavljevic, and R. Jimenez, "Efficient cosmological parameter estimation from microwave background anisotropies", *Phys. Rev. D*, vol. 66, no. 6, p. 063 007, 2002.

[47] M. Taoso, G. Bertone, and A. Masiero, "Dark matter candidates: a ten-point test", *J. Cosmol. Astropart. Phys.*, vol. 2008, no. 03, p. 022, 2008.

[48] B. Moore *et al.*, "Dark matter substructure within galactic halos", *Astrophys. J.*, vol. 524, no. 1, p. L19, 1999.

[49] A. Klypin *et al.*, "Where are the missing galactic satellites?", *Astrophys. J.*, vol. 522, no. 1, p. 82, 1999.

[50] P. Bode, J. P. Ostriker, and N. Turok, "Halo formation in warm dark matter models", *Astrophys. J.*, vol. 556, no. 1, p. 93, 2001.

[51] D. N. Spergel and P. J. Steinhardt, "Observational evidence for self-interacting cold dark matter", *Phys. Rev. Lett.*, vol. 84, no. 17, p. 3760, 2000.

[52] V. A. Acciari *et al.*, "Constraining dark matter lifetime with a deep gamma-ray survey of the Perseus galaxy cluster with MAGIC", *Phys. Dark Universe*, vol. 22, pp. 38–47, 2018.

[53] D. N. Schramm and M. S. Turner, “Big-bang nucleosynthesis enters the precision era”, *Rev. Mod. Phys.*, vol. 70, no. 1, p. 303, 1998.

[54] D. Tytler, X.-M. Fan, and S. Burles, “Cosmological baryon density derived from the deuterium abundance at redshift $z = 3.57$”, *Nature*, vol. 381, pp. 207–209, 1996.

[55] S. D. McDermott, H.-B. Yu, and K. M. Zurek, “Turning off the lights: how dark is dark matter?”, *Phys. Rev. D*, vol. 83, no. 6, p. 063 509, 2011.

[56] A. D. Dolgov, S. L. Dubovsky, G. I. Rubtsov, and I. I. Tkachev, “Constraints on millicharged particles from Planck data”, *Phys. Rev. D*, vol. 88, no. 11, p. 117 701, 2013.

[57] D. Harvey *et al.*, “The non-gravitational interactions of dark matter in colliding galaxy clusters”, *Science*, vol. 347, no. 6229, pp. 1462–1465, 2015.

[58] S. Adhikari *et al.*, “Astrophysical Tests of Dark Matter Self-Interactions”, 2022.

[59] R. Foot, “Mirror dark matter: Cosmology, galaxy structure and direct detection”, *Int. J. Mod. Phys. A*, vol. 29, no. 11n12, p. 1 430 013, 2014.

[60] G. Bertone, D. Hooper, and J. Silk, “Particle dark matter: Evidence, candidates and constraints”, *Phys. Rep.*, vol. 405, no. 5-6, pp. 279–390, 2005.

[61] R. D. Peccei and H. R. Quinn, “CP conservation in the presence of pseudoparticles”, *Phys. Rev. Lett.*, vol. 38, no. 25, p. 1440, 1977.

[62] F. C. Porter and K. C. Königsmann, “Unambiguous test for the axion”, *Phys. Rev. D*, vol. 25, no. 7, p. 1993, 1982.

[63] M. Kuster, G. Raffelt, and B. Beltrán, “Chapter 5: Axions and Their Relatives”, in *Axions: Theory, Cosmology, and Experimental Searches*, vol. 741, Springer, 2007.

[64] L. D. Duffy and K. Van Bibber, “Axions as dark matter particles”, *New J. Phys.*, vol. 11, no. 10, p. 105 008, 2009.

[65] L. J. Rosenberg and K. A. Van Bibber, “Searches for invisible axions”, *Phys. Rep.*, vol. 325, no. 1, pp. 1–39, 2000.

[66] J. B. Dent, B. Dutta, J. L. Newstead, and A. Thompson, “Inverse Primakoff scattering as a probe of solar axions at liquid xenon direct detection experiments”, *Phys. Rev. Lett.*, vol. 125, no. 13, p. 131 805, 2020.

[67] S. Dimopoulos, G. D. Starkman, and B. W. Lynn, “Atomic enhancements in the detection of weakly interacting particles”, *Phys. Lett. B*, vol. 168, no. 1-2, pp. 145–150, 1986.

[68] J. R. Bond, G. Efstathiou, and J. Silk, “Massive neutrinos and the large-scale structure of the universe”, *Phys. Rev. Lett.*, vol. 45, no. 24, 1980.

[69] A. D. Dolgov, “Neutrinos in cosmology”, *Phys. Rep.*, vol. 370, no. 4-5, pp. 333–535, 2002.

[70] M. Aker *et al.* (KATRIN Collaboration), “Direct neutrino-mass measurement with sub-electronvolt sensitivity”, *Nature Physics*, vol. 18, no. 2, pp. 160–166, 2022.

[71] S. Dodelson and L. M. Widrow, "Sterile neutrinos as dark matter", *Phys. Rev. Lett.*, vol. 72, no. 1, p. 17, 1994.

[72] A. Merle, "keV neutrino model building", *Int. J. Mod. Phys. D*, vol. 22, no. 10, p. 1 330 020, 2013.

[73] E. W. Kolb and M. S. Turner, "Chapter 5: Thermodynamics in the Expanding Universe", in *The Early Universe*, vol. 69, 1990.

[74] K. Freese, "Status of dark matter in the universe", *Int. J. Mod. Phys. D*, vol. 26, no. 06, p. 1 730 012, 2017.

[75] G. Gelmini and P. Gondolo, "Chapter 7: DM production mechanisms", in *Particle Dark Matter: Observations, Models and Searches*, G. Bertone, Ed., Cambridge University Press, 2010.

[76] K. Griest, "Galactic microlensing as a method of detecting massive compact halo objects", *Astrophys. J.*, vol. 366, pp. 412–421, 1991.

[77] K. Griest, "The search for the dark matter: WIMPs and MACHOs", 1993.

[78] C. Alcock *et al.*, "The MACHO project: microlensing results from 5.7 years of Large Magellanic Cloud observations", *Astrophys. J.*, vol. 542, no. 1, p. 281, 2000.

[79] A. Escrivà, F. Kuhnel, and Y. Tada, "Primordial Black Holes", 2022.

[80] B. Carr *et al.*, "Constraints on primordial black holes", *Rep. Prog. Phys.*, vol. 84, no. 11, p. 116 902, 2021.

[81] P. Villanueva-Domingo, O. Mena, and S. Palomares-Ruiz, "A brief review on primordial black holes as dark matter", *Frontiers in Astronomy and Space Sciences*, vol. 8, p. 681 084, 2021.

[82] R. Saito and J. Yokoyama, "Gravitational-wave background as a probe of the primordial black-hole abundance", *Phys. Rev. Lett.*, vol. 102, no. 16, p. 161 101, 2009.

[83] M. Milgrom, "A modification of the Newtonian dynamics as a possible alternative to the hidden mass hypothesis", *Astrophys. J.*, vol. 270, pp. 365–370, 1983.

[84] J. D. Bekenstein, "Relativistic gravitation theory for the modified Newtonian dynamics paradigm", *Phys. Rev. D*, vol. 70, p. 083 509, 2004.

[85] K. G. Begeman, A. H. Broeils, and R. H. Sanders, "Extended rotation curves of spiral galaxies: Dark haloes and modified dynamics", *Mon. Notices Royal Astron. Soc.*, vol. 249, no. 3, pp. 523–537, 1991.

[86] B. Famaey and S. S. McGaugh, "Modified Newtonian dynamics (MOND): observational phenomenology and relativistic extensions", *Living reviews in relativity*, vol. 15, pp. 1–159, 2012.

[87] A. Boveia and C. Doglioni, "Dark matter searches at colliders", *Annu. Rev. Nucl. Part. Sci.*, vol. 68, pp. 429–459, 2018.

[88] M. Aaboud *et al.* (ATLAS Collaboration), "Search for dark matter and other new phenomena in events with an energetic jet and large missing transverse momentum using the ATLAS detector", *J. High Energy Phys.*, vol. 2018, no. 1, pp. 1–53, 2018.

[89] C. Collaboration, “Search for new physics in final states with an energetic jet or a hadronically decaying W or Z boson and transverse momentum imbalance at $\sqrt{s} = 13\,\text{TeV}$”, 2017.

[90] G. Aad *et al.* (ATLAS Collaboration), “Search for associated production of a Z boson with an invisibly decaying Higgs boson or dark matter candidates at $\sqrt{s} = 13\,\text{TeV}$ with the ATLAS detector”, *Phys. Lett. B*, vol. 829, p. 137 066, 2022.

[91] A. M. Sirunyan *et al.* (CMS Collaboration), “Search for dark matter produced in association with a leptonically decaying Z boson in proton–proton collisions at $\sqrt{s} = 13\,\text{TeV}$”, *Eur. Phys. J. C*, vol. 81, pp. 1–33, 2021.

[92] M. Aaboud *et al.* (ATLAS Collaboration), “Search for dark matter in association with a Higgs boson decaying to two photons at $\sqrt{s} = 13\,\text{TeV}$ with the ATLAS detector”, *Phys. Rev. D*, vol. 96, no. 11, p. 112 004, 2017.

[93] A. M. Sirunyan *et al.* (CMS Collaboration), “Search for dark matter particles produced in association with a Higgs boson in proton-proton collisions at $\sqrt{s} = 13\,\text{TeV}$”, *J. High Energy Phys.*, vol. 2020, no. 3, pp. 1–57, 2020.

[94] A. Collaboration, “Measurement of detector-corrected observables sensitive to the anomalous production of events with jets and large missing transverse momentum in *pp* collisions at $\sqrt{s} = 13\,\text{TeV}$”, *Eur. Phys. J. C*, vol. 77, p. 765, 2017.

[95] M. Carena *et al.*, “Invisible Z-boson decays at e^+e^- colliders”, *Phys. Rev. D*, vol. 68, no. 11, p. 113 007, 2003.

[96] M. Aaboud *et al.* (ATLAS Collaboration), “Constraints on mediator-based dark matter and scalar dark energy models using $\sqrt{s} = 13\,\text{TeV}$ *pp* collision data collected by the ATLAS detector”, *J. High Energy Phys.*, vol. 2019, no. 5, 2019.

[97] C. Pérez de los Heros, “Status, challenges and directions in indirect dark matter searches”, *Symmetry*, vol. 12, no. 10, p. 1648, 2020.

[98] C. A. Argüelles *et al.*, “Dark matter annihilation to neutrinos”, *Rev. Mod. Phys.*, vol. 93, no. 3, p. 035 007, 2021.

[99] A. Albert *et al.* (ANTARES Collaboration), “Search for dark matter towards the Galactic Centre with 11 years of ANTARES data”, *Phys. Lett. B*, vol. 805, p. 135 439, 2020.

[100] S. Adrián-Martınez *et al.* (ANTARES Collaboration), “Limits on dark matter annihilation in the sun using the ANTARES neutrino telescope”, *Phys. Lett. B*, vol. 759, pp. 69–74, 2016.

[101] R. Abbasi *et al.* (IceCube Collaboration), “Search for neutrino lines from dark matter annihilation and decay with IceCube”, 2023.

[102] M. G. Aartsen *et al.* (IceCube Collaboration), “Search for annihilating dark matter in the Sun with 3 years of IceCube data”, *Eur. Phys. J. C*, vol. 77, no. 3, pp. 1–12, 2017.

[103] K. Abe *et al.* (Super-Kamiokande Collaboration), “Indirect search for dark matter from the Galactic Center and halo with the Super-Kamiokande detector”, *Phys. Rev. D*, vol. 102, no. 7, p. 072 002, 2020.

[104] K. Choi *et al.* (Super-Kamiokande Collaboration), "Search for neutrinos from annihilation of captured low-mass dark matter particles in the Sun by Super-Kamiokande", *Phys. Rev. Lett.*, vol. 114, no. 14, p. 141 301, 2015.

[105] A. Albert *et al.* (Fermi-LAT and DES collaborations), "Searching for dark matter annihilation in recently discovered Milky Way satellites with Fermi-LAT", *Astrophys. J.*, vol. 834, no. 2, p. 110, 2017.

[106] M. Aguilar *et al.* (AMS Collaboration), "The Alpha Magnetic Spectrometer (AMS) on the international space station: Part II – Results from the first seven years", *Phys. Rep.*, vol. 894, pp. 1–116, 2021.

[107] H. Abdallah *et al.* (H.E.S.S. Collaboration), "Search for γ-ray line signals from dark matter annihilations in the inner galactic halo from 10 years of observations with H.E.S.S.", *Phys. Rev. Lett.*, vol. 120, no. 20, p. 201 101, 2018.

[108] L. Goodenough and D. Hooper, "Possible evidence for dark matter annihilation in the inner Milky Way from the Fermi Gamma Ray Space Telescope", 2009.

[109] M. Ackermann *et al.* (Fermi-LAT collaborations), "Searching for dark matter annihilation from Milky Way dwarf spheroidal galaxies with six years of Fermi Large Area Telescope data", *Phys. Rev. Lett.*, vol. 115, no. 23, p. 231 301, 2015.

[110] R. Bartels, S. Krishnamurthy, and C. Weniger, "Strong support for the millisecond pulsar origin of the Galactic center GeV excess", *Phys. Rev. Lett.*, vol. 116, no. 5, p. 051 102, 2016.

[111] I. Cholis *et al.*, "The PAMELA positron excess from annihilations into a light boson", *J. Cosmol. Astropart. Phys.*, vol. 2009, no. 12, p. 007, 2009.

[112] M. Aguilar *et al.* (AMS Collaboration), "First result from the Alpha Magnetic Spectrometer on the International Space Station: precision measurement of the positron fraction in primary cosmic rays of 0.5–350 GeV", *Phys. Rev. Lett.*, vol. 110, no. 14, p. 141 102, 2013.

[113] M. Aguilar *et al.* (AMS Collaboration), "Antiproton flux, antiproton-to-proton flux ratio, and properties of elementary particle fluxes in primary cosmic rays measured with the alpha magnetic spectrometer on the international space station", *Phys. Rev. Lett.*, vol. 117, no. 9, p. 091 103, 2016.

[114] G. Giesen *et al.*, "AMS-02 antiprotons, at last! Secondary astrophysical component and immediate implications for Dark Matter", *J. Cosmol. Astropart. Phys.*, vol. 2015, no. 09, p. 023, 2015.

[115] J. F. Navarro, C. S. Frenk, and S. D. M. White, "The Structure of Cold Dark Matter Halos", *Astrophys. J.*, vol. 462, p. 563, 1996.

[116] F. Mayet *et al.*, "A review of the discovery reach of directional Dark Matter detection", *Phys. Rep.*, vol. 627, pp. 1–49, 2016.

[117] M. C. Smith *et al.*, "The RAVE survey: constraining the local galactic escape speed", *Mon. Notices Royal Astron. Soc.*, vol. 379, no. 2, pp. 755–772, 2007.

[118] F. J. Kerr and D. Lynden-Bell, "Review of galactic constants", *Mon. Notices Royal Astron. Soc.*, vol. 221, no. 4, pp. 1023–1038, 1986.

[119] N. W. Evans, C. A. J. O'Hare, and C. McCabe, "Refinement of the standard halo model for dark matter searches in light of the Gaia Sausage", *Phys. Rev. D*, vol. 99, no. 2, p. 023 012, 2019.

[120] D. G. Cerdeño and A. M. Green, "Chapter 17: Direct detection of WIMPs", in *Particle Dark Matter: Observations, Models and Searches*, G. Bertone, Ed., Cambridge University Press, 2010.

[121] A. L. Fitzpatrick *et al.*, "The effective field theory of dark matter direct detection", *J. Cosmol. Astropart. Phys.*, vol. 2013, no. 02, p. 004, 2013.

[122] E. Del Nobile, "Chapter 6: Scattering Cross Section", in *The Theory of Direct Dark Matter Detection*, Springer, 2022, pp. 129–196.

[123] J. Aalbers *et al.*, *JelleAalbers/wimprates*, version v0.5.0, 2023.

[124] M. Schumann, "Direct detection of WIMP dark matter: concepts and status", *J. Phys. G*, vol. 46, no. 10, p. 103 003, 2019.

[125] Z. Y. Zhang *et al.* (CDEX Collaboration), "Constraints on Sub-GeV Dark Matter–Electron Scattering from the CDEX-10 Experiment", *Phys. Rev. Lett.*, vol. 129, no. 22, p. 221 301, 2022.

[126] I. Arnquist *et al.* (DAMIC-M Collaboration), "The DAMIC-M experiment: Status and first results", 2022.

[127] L. Barak *et al.* (SENSEI Collaboration), "SENSEI: Direct-Detection Results on sub-GeV Dark Matter from a New Skipper-CCD", *Phys. Rev. Lett.*, vol. 125, no. 17, p. 171 802, 2020.

[128] J. Amaré *et al.*, "Annual modulation results from three-year exposure of ANAIS-112", *Phys. Rev. D*, vol. 103, no. 10, p. 102 005, 2021.

[129] G. Adhikari *et al.* (COSINE-100 Collaboration), "Three-year annual modulation search with COSINE-100", *Phys. Rev. D*, vol. 106, no. 5, p. 052 005, 2022.

[130] R. Bernabei *et al.*, "First model independent results from DAMA/LIBRA–phase2", *Universe*, vol. 4, no. 11, p. 116, 2018.

[131] Y. S. Yoon *et al.* (KIMS Collaboration), "Search for solar axions with CsI(Tl) crystal detectors", *J. High Energy Phys.*, vol. 2016, no. 6, pp. 1–10, 2016.

[132] K. Freese, M. Lisanti, and C. Savage, "Annual modulation of dark matter: a review", 2012.

[133] R. Agnese *et al.* (SuperCDMS Collaboration), "Search for low-mass dark matter with CDMSlite using a profile likelihood fit", *Phys. Rev. D*, vol. 99, no. 6, p. 062 001, 2019.

[134] D. W. Amaral *et al.* (SuperCDMS Collaboration), "Constraints on low-mass, relic dark matter candidates from a surface-operated SuperCDMS single-charge sensitive detector", *Phys. Rev. D*, vol. 102, no. 9, p. 091 101, 2020.

[135] Q. Arnaud *et al.* (EDELWEISS Collaboration), "First germanium-based constraints on sub-MeV Dark Matter with the EDELWEISS experiment", *Phys. Rev. Lett.*, vol. 125, no. 14, p. 141 301, 2020.

[136] G. Angloher *et al.* (CRESST Collaboration), "Results on light dark matter particles with a low-threshold CRESST-II detector", *Eur. Phys. J. C*, vol. 76, pp. 1–8, 2016.

[137] A. H. Abdelhameed *et al.* (CRESST Collaboration), "First results from the CRESST-III low-mass dark matter program", *Phys. Rev. D*, vol. 100, no. 10, p. 102 002, 2019.

[138] R. Ajaj *et al.* (DEAP Collaboration), "Search for dark matter with a 231-day exposure of liquid argon using DEAP-3600 at SNOLAB", *Phys. Rev. D*, vol. 100, no. 2, p. 022 004, 2019.

[139] K. Abe *et al.* (XMASS Collaboration), "A direct dark matter search in XMASS-I", *Phys. Lett. B*, vol. 789, pp. 45–53, 2019.

[140] P. Agnes *et al.* (DarkSide Collaboration), "DarkSide-50 532-day dark matter search with low-radioactivity argon", *Phys. Rev. D*, vol. 98, no. 10, p. 102 006, 2018.

[141] D. S. Akerib *et al.* (LUX Collaboration), "Results from a search for dark matter in the complete LUX exposure", *Phys. Rev. Lett.*, vol. 118, no. 2, p. 021 303, 2017.

[142] J. Aalbers *et al.* (LZ Collaboration), "First Dark Matter Search Results from the LUX-ZEPLIN (LZ) Experiment", *Phys. Rev. Lett.*, vol. 131, p. 041 002, 2023.

[143] E. Aprile *et al.* (XENON Collaboration), "First Dark Matter Search with Nuclear Recoils from the XENONnT Experiment", 2023.

[144] Y. Meng *et al.* (PandaX Collaboration), "Dark matter search results from the PandaX-4T commissioning run", *Phys. Rev. Lett.*, vol. 127, no. 26, p. 261 802, 2021.

[145] E. Behnke *et al.* (PICASSO Collaboration), "Final results of the PICASSO dark matter search experiment", *Astropart. Phys.*, vol. 90, pp. 85–92, 2017.

[146] C. Amole *et al.* (PICO Collaboration), "Dark matter search results from the complete exposure of the PICO-60 C_3F_8 bubble chamber", *Phys. Rev. D*, vol. 100, no. 2, p. 022 001, 2019.

[147] J. B. R. Battat *et al.* (DRIFT Collaboration), "Low threshold results and limits from the DRIFT directional dark matter detector", *Astropart. Phys.*, vol. 91, pp. 65–74, 2017.

[148] A. H. G. Peter *et al.*, "WIMP physics with ensembles of direct-detection experiments", *Phys. Dark Universe*, vol. 5, pp. 45–74, 2014.

[149] T. Braine *et al.* (ADMX Collaboration), "Extended search for the invisible axion with the axion dark matter experiment", *Phys. Rev. Lett.*, vol. 124, no. 10, p. 101 303, 2020.

[150] Q. Arnaud *et al.* (NEWS-G Collaboration), "First results from the NEWS-G direct dark matter search experiment at the LSM", *Astropart. Phys.*, vol. 97, pp. 54–62, 2018.

[151] S. A. Hertel *et al.*, "Direct detection of sub-GeV dark matter using a superfluid ^{4}He target", *Phys. Rev. D*, vol. 100, no. 9, p. 092 007, 2019.

[152] D. Akerib *et al.*, *HydroX – Using hydrogen doped in liquid xenon to search for dark matter*, 2021.

[153] S. Kravitz *et al.*, "Operation and performance of a dual-phase crystalline/vapor xenon time projection chamber", *J. Instrum.*, vol. 17, no. 04, P04014, 2022.

[154] S. P. Ahlen *et al.*, "Limits on cold dark matter candidates from an ultralow background germanium spectrometer", *Phys. Lett. B*, vol. 195, no. 4, pp. 603–608, 1987.

[155] C. A. J. O'Hare, "New definition of the neutrino floor for direct dark matter searches", *Phys. Rev. Lett.*, vol. 127, no. 25, p. 251 802, 2021.

[156] J. Billard, E. Figueroa-Feliciano, and L. Strigari, "Implication of neutrino backgrounds on the reach of next generation dark matter direct detection experiments", *Phys. Rev. D*, vol. 89, no. 2, p. 023 524, 2014.

[157] A. S. Chou *et al.*, "Snowmass Cosmic Frontier Report", 2022.

[158] J. Aalbers *et al.*, "A next-generation liquid xenon observatory for dark matter and neutrino physics", *J. Phys. G*, vol. 50, no. 1, p. 013 001, 2022.

[159] M. Thomson, "Chapter 13: Neutrinos and neutrino oscillations", in *Modern Particle Physics*, Cambridge University Press, 2013.

[160] I. Esteban *et al.*, "Global analysis of three-flavour neutrino oscillations: Synergies and tensions in the determination of θ_{23}, δ_{CP}, and the mass ordering", *J. High Energy Phys.*, vol. 2019, no. 1, pp. 1–35, 2019.

[161] C. Giunti and C. W. Kim, "Chapter 6: Massive neutrinos", in *Fundamentals of Neutrino Physics and Astrophysics*, Oxford University Press, 2007.

[162] K. Zuber, "Chapter 2: Properties of Neutrinos", in *Neutrino Physics*, 3rd ed., Taylor & Francis, 2020.

[163] M. Thomson, "Chapter 17: The Higgs boson", in *Modern Particle Physics*, Cambridge University Press, 2013.

[164] A. D. Sakharov, "Violation of CP Invariance, C asymmetry, and baryon asymmetry of the universe", *Pisma Zh. Eksp. Teor. Fiz.*, vol. 5, pp. 32–35, 1967.

[165] S. Davidson, E. Nardi, and Y. Nir, "Leptogenesis", *Physics Reports*, vol. 466, no. 4-5, pp. 105–177, 2008.

[166] M. Goeppert-Mayer, "Double beta-disintegration", *Phys. Rev.*, vol. 48, pp. 512–516, 1935.

[167] S. D'Auria, "Chapter 7: Introduction to Nuclear Physics", in *Introduction to Nuclear and Particle Physics*, Springer, 2019.

[168] R. Taylor, "Neutrinoless Double Beta Decay in Dual-phase Xenon Time Projection Chambers: LUX, LZ and Prospects for G3", Ph.D. dissertation, Imperial College London, 2020.

[169] A. S. Barabash, "Average and recommended half-life values for two-neutrino double beta decay", *Nucl. Phys. A*, vol. 935, pp. 52–64, 2015.

[170] S. R. Elliott, A. A. Hahn, and M. K. Moe, "Direct evidence for two-neutrino double-beta decay in ^{82}Se", *Phys. Rev. Lett.*, vol. 59, pp. 2020–2023, 1987.

[171] J. Kotila and F. Iachello, "Phase space factors for $\beta^+\beta^+$ decay and competing modes of double-β decay", *Phys. Rev. C*, vol. 87, no. 2, p. 024 313, 2013.

[172] W. H. Furry, "On transition probabilities in double beta-disintegration", *Phys. Rev.*, vol. 56, pp. 1184–1193, 1939.

[173] S. Dell'Oro *et al.*, "Neutrinoless double beta decay: 2015 review", *Adv. High Energy Phys.*, vol. 2016, p. 2 162 659, 2016.

[174] S. Bilenky, "Chapter 9: Neutrinoless double beta-decay", in *Introduction to the Physics of Massive and Mixed Neutrinos*, 2nd ed., vol. 947, Springer, 2018.

[175] S. M. Bilenky and C. Giunti, "Neutrinoless Double-Beta Decay: a Probe of Physics Beyond the Standard Model", *Int. J. Mod. Phys. A*, vol. 30, p. 1 530 001, 2015.

[176] R. Arnold *et al.* (NEMO-3 Collaboration), "Results of the search for neutrinoless double-β decay in ^{100}Mo with the NEMO-3 experiment", *Phys. Rev. D*, vol. 92, no. 7, p. 072 011, 2015.

[177] M. Agostini *et al.* (GERDA Collaboration), "Final results of GERDA on the search for neutrinoless double-β decay", *Physical review letters*, vol. 125, no. 25, p. 252 502, 2020.

[178] I. Nutini *et al.* (CUORE Collaboration), "Latest results from the CUORE experiment", *J. Low Temp. Phys.*, vol. 209, no. 5-6, pp. 927–935, 2022.

[179] S. Abe *et al.* (KamLAND-Zen Collaboration), "Search for the Majorana Nature of Neutrinos in the Inverted Mass Ordering Region with KamLAND-Zen", *Phys. Rev. Lett.*, vol. 130, no. 5, p. 051 801, 2023.

[180] A. Mastbaum, *Neutrinoless double-beta decay "lobster" plot*, 2015.

[181] M. J. Dolinski, A. W. P. Poon, and W. Rodejohann, "Neutrinoless Double-Beta Decay: Status and Prospects", *Ann. Rev. Nucl. Part. Sci.*, vol. 69, pp. 219–251, 2019.

[182] J. Kotila, J. Barea, and F. Iachello, "Neutrinoless double-electron capture", *Phys. Rev. C*, vol. 89, no. 6, p. 064 319, 2014.

[183] J. J. Gomez-Cadenas *et al.*, "The search for neutrinoless double beta decay", *Riv. Nuovo Cimento*, vol. 35, pp. 29–98, 2012.

[184] B. Pritychenko *et al.*, "Nuclear reaction and structure data services of the National Nuclear Data Center", *Ann. Nucl. Energy*, vol. 33, no. 4, pp. 390–399, 2006.

[185] T. Iida *et al.* (CANDLES Collaboration), "The CANDLES experiment for the study of Ca-48 double beta decay", *Nucl. Part. Phys. Proc.*, vol. 273-275, pp. 2633–2635, 2016.

[186] S. Umehara *et al.*, "Neutrino-less double-β decay of ^{48}Ca studied by CaF_2(Eu) scintillators", *Phys. Rev. C*, vol. 78, p. 058 501, 2008.

[187] R. Arnold *et al.* (NEMO-3 Collaboration), "Measurement of the double-beta decay half-life and search for the neutrinoless double-beta decay of ^{48}Ca with the NEMO-3 detector", *Phys. Rev. D*, vol. 93, p. 112 008, 2016.

[188] I. J. Arnquist *et al.* (MAJORANA Collaboration), "Final Result of the Majorana Demonstrator's Search for Neutrinoless Double-β Decay in ^{76}Ge", *Phys. Rev. Lett.*, vol. 130, p. 062 501, 2023.

[189] O. Azzolini *et al.* (CUPID Collaboration), "Final Result of CUPID-0 Phase-I in the Search for the ^{82}Se Neutrinoless Double-β Decay", *Phys. Rev. Lett.*, vol. 123, p. 032 501, 2019.

[190] R. Arnold *et al.* (NEMO-3 Collaboration), "Final results on ^{82}Se double beta decay to the ground state of ^{82}Kr from the NEMO-3 experiment", *Eur. Phys. J. C*, vol. 78, no. 10, pp. 1–15, 2018.

[191] J. Argyriades *et al.* (NEMO-3 Collaboration), “Measurement of the two neutrino double beta decay half-life of Zr-96 with the NEMO-3 detector”, *Nucl. Phys. A*, vol. 847, no. 3, pp. 168–179, 2010.

[192] C. Augier *et al.* (CUPID Collaboration), “Final results on the $0\nu\beta\beta$ decay half-life limit of ^{100}Mo from the CUPID-Mo experiment”, *Eur. Phys. J. C*, vol. 82, no. 11, p. 1033, 2022.

[193] R. Arnold *et al.* (NEMO-3 Collaboration), “Measurement of the $2\nu\beta\beta$ decay half-life and search for the $0\nu\beta\beta$ decay of ^{116}Cd with the NEMO-3 detector”, *Phys. Rev. D*, vol. 95, p. 012 007, 2017.

[194] G. Anton *et al.* (EXO-200 Collaboration), “Search for Neutrinoless Double-β Decay with the Complete EXO-200 Dataset”, *Phys. Rev. Lett.*, vol. 123, p. 161 802, 2019.

[195] P. Novella *et al.* (NEXT Collaboration), “Demonstration of neutrinoless double beta decay searches in gaseous xenon with NEXT”, 2023.

[196] R. Arnold *et al.* (NEMO-3 Collaboration), “Measurement of the $2\nu\beta\beta$ decay half-life of ^{150}Nd and a search for $0\nu\beta\beta$ decay processes with the full exposure from the NEMO-3 detector”, *Phys. Rev. D*, vol. 94, p. 072 003, 2016.

[197] N. Abgrall *et al.* (LEGEND Collaboration), “The large enriched germanium experiment for neutrinoless double beta decay (LEGEND)”, vol. 1894, 2017.

[198] D. S. Akerib *et al.* (LZ Collaboration), “Identification of radiopure titanium for the LZ dark matter experiment and future rare event searches”, *Astropart. Phys.*, vol. 96, pp. 1–10, 2017.

[199] R. Linehan *et al.* (LZ Collaboration), “Design and production of the high voltage electrode grids and electron extraction region for the LZ dual-phase xenon time projection chamber”, *Nucl. Instrum.*, vol. 1031, p. 165 955, 2022.

[200] F. Neves *et al.*, “Measurement of the absolute reflectance of polytetrafluoroethylene (PTFE) immersed in liquid xenon”, *J. Instrum.*, vol. 12, no. 01, P01017, 2017.

[201] D. Akerib *et al.* (LZ Collaboration), “The LUX-ZEPLIN (LZ) experiment”, *Nucl. Instrum.*, vol. 953, p. 163 047, 2020.

[202] B. L. Paredes *et al.*, “Response of photomultiplier tubes to xenon scintillation light”, *Astropart. Phys.*, vol. 102, pp. 56–66, 2018.

[203] D. Y. Akimov *et al.*, “Observation of light emission from Hamamatsu R11410-20 photomultiplier tubes”, *Nucl. Instrum.*, vol. 794, pp. 1–2, 2015.

[204] B. J. Mount *et al.* (LZ Collaboration), *LUX-ZEPLIN (LZ) Technical Design Report*, 2017.

[205] S. J. Haselschwardt *et al.*, “A liquid scintillation detector for radioassay of gadolinium-loaded liquid scintillator for the LZ outer detector”, *Nucl. Instrum.*, vol. 937, pp. 148–163, 2019.

[206] A. Dobi *et al.*, “Study of a zirconium getter for purification of xenon gas”, *Nucl. Instrum.*, vol. 620, no. 2-3, pp. 594–598, 2010.

[207] K. Abe *et al.*, “Radon removal from gaseous xenon with activated charcoal”, *Nucl. Instrum.*, vol. 661, no. 1, pp. 50–57, 2012.

[208] M. Arthurs *et al.*, “Performance study of charcoal-based radon reduction systems for ultraclean rare event detectors”, *J. Instrum.*, vol. 16, no. 07, P07047, 2021.

[209] R. L. Platzman, “Total ionization in gases by high-energy particles: An appraisal of our understanding”, *Appl. Radiat. Isot.*, vol. 10, no. 2-3, pp. 116–127, 1961.

[210] T. Doke *et al.*, “Absolute scintillation yields in liquid argon and xenon for various particles”, *Jap. J. Appl. Phys.*, vol. 41, no. 3R, p. 1538, 2002.

[211] P. Sorensen and C. E. Dahl, “Nuclear recoil energy scale in liquid xenon with application to the direct detection of dark matter”, *Phys. Rev. D*, vol. 83, no. 6, p. 063 501, 2011.

[212] C. E. Dahl, “The physics of background discrimination in liquid xenon, and first results from Xenon10 in the hunt for WIMP dark matter”, Ph.D. dissertation, Princeton U., 2009.

[213] F. Bezrukov, F. Kahlhoefer, and M. Lindner, “Interplay between scintillation and ionization in liquid xenon Dark Matter searches”, *Astropart. Phys.*, vol. 35, no. 3, pp. 119–127, 2011.

[214] V. Chepel and H. Araújo, “Liquid noble gas detectors for low energy particle physics”, *J. Instrum.*, vol. 8, no. 04, R04001, 2013.

[215] A. Hitachi, T. Doke, and A. Mozumder, “Luminescence quenching in liquid argon under charged-particle impact: Relative scintillation yield at different linear energy transfers”, *Phys. Rev. B*, vol. 46, no. 18, p. 11 463, 1992.

[216] J. Mock *et al.*, “Modeling pulse characteristics in Xenon with NEST”, *J. Instrum.*, vol. 9, no. 04, T04002, 2014.

[217] E. Hogenbirk *et al.*, “Precision measurements of the scintillation pulse shape for low-energy recoils in liquid xenon”, *J. Instrum.*, vol. 13, no. 05, P05016, 2018.

[218] L. Baudis, P. Sanchez-Lucas, and K. Thieme, “A measurement of the mean electronic excitation energy of liquid xenon”, *Eur. Phys. J. C*, vol. 81, pp. 1–12, 2021.

[219] G. Anton *et al.* (EXO-200 Collaboration), “Measurement of the scintillation and ionization response of liquid xenon at MeV energies in the EXO-200 experiment”, *Phys. Rev. C*, vol. 101, no. 6, p. 065 501, 2020.

[220] T. Shutt *et al.*, “Performance and fundamental processes at low energy in a two-phase liquid xenon dark matter detector”, *Nucl. Phys. B Proc.*, vol. 173, pp. 160–163, 2007.

[221] J. Lindhard *et al.*, “Integral equations governing radiation effects”, *Mat. Fys. Medd. Dan. Vid. Selsk.*, vol. 33, no. 10, pp. 1–42, 1963.

[222] D. S. Akerib *et al.* (LUX Collaboration), “Liquid xenon scintillation measurements and pulse shape discrimination in the LUX dark matter detector”, *Phys. Rev. D*, vol. 97, no. 11, p. 112 002, 2018.

[223] W. H. o. Lippincott, “Scintillation time dependence and pulse shape discrimination in liquid argon”, *Phys. Rev. C*, vol. 78, no. 3, p. 035 801, 2008.

[224] M. J. Berger *et al.*, *XCOM: Photon Cross Sections Database*, 2010.

[225] M. Szydagis *et al.*, “NEST: a comprehensive model for scintillation yield in liquid xenon”, *J. Instrum.*, vol. 6, no. 10, P10002, 2011.

[226] M. Szydagis *et al.*, "A Review of NEST Models, and Their Application to Improvement of Particle Identification in Liquid Xenon Experiments", 2022.

[227] D. S. Akerib *et al.* (LZ Collaboration), "The LUX-ZEPLIN (LZ) radioactivity and cleanliness control programs", *Eur. Phys. J. C*, vol. 80, no. 11, 2020.

[228] V. A. Kudryavtsev, P. Zakhary, and B. Easeman, "Neutron production in (α, n) reactions", *Nucl. Instrum.*, vol. 972, p. 164 095, 2020.

[229] D. S. Akerib *et al.* (LZ Collaboration), "Projected WIMP sensitivity of the LUX-ZEPLIN dark matter experiment", *Phys. Rev. D*, vol. 101, p. 052 002, 2020.

[230] F. E. Gray *et al.*, "Cosmic ray muon flux at the Sanford Underground Laboratory at Homestake", *Nucl. Instrum.*, vol. 638, no. 1, pp. 63–66, 2011.

[231] D. S. Akerib *et al.* (LZ Collaboration), "Measurement of the gamma ray background in the Davis cavern at the Sanford Underground Research Facility", *Astropart. Phys.*, vol. 116, p. 102 391, 2020.

[232] J. Aalbers *et al.* (LZ Collaboration), "Cosmogenic production of ^{3}7Ar in the context of the LUX-ZEPLIN experiment", *Phys. Rev. D*, vol. 105, no. 8, p. 082 004, 2022.

[233] J. B. Albert *et al.* (EXO-200 Collaboration), "Improved measurement of the $2\nu\beta\beta$ half-life of ^{136}Xe with the EXO-200 detector", *Phys. Rev. C*, vol. 89, no. 1, p. 015 502, 2014.

[234] J. B. Albert *et al.* (EXO-200 Collaboration), "Measurements of the ion fraction and mobility of α- and β-decay products in liquid xenon using the EXO-200 detector", *Phys. Rev. C*, vol. 92, no. 4, p. 045 504, 2015.

[235] D. S. Akerib *et al.* (LUX Collaboration), "Tritium calibration of the LUX dark matter experiment", *Phys. Rev. D*, vol. 93, no. 7, p. 072 009, 2016.

[236] D. S. Akerib *et al.* (LUX Collaboration), "Low-energy (0.7-74 keV) nuclear recoil calibration of the LUX dark matter experiment using DD neutron scattering kinematics", 2016.

[237] W. Turner *et al.*, "Optical calibration system for the LUX-ZEPLIN (LZ) outer detector", *Nucl. Instrum.*, vol. 1010, p. 165 551, 2021.

[238] D. S. Akerib *et al.* (LZ Collaboration), "Simulations of events for the LUX-ZEPLIN (LZ) dark matter experiment", *Astropart. Phys.*, vol. 125, p. 102 480, 2021.

[239] S. Agostinelli *et al.*, "GEANT4–a simulation toolkit", *Nucl. Instrum.*, vol. 506, no. 3, pp. 250–303, 2003.

[240] P. Brás *et al.*, "A machine learning-based methodology for pulse classification in dual-phase xenon time projection chambers", *Eur. Phys. J. C*, vol. 82, no. 6, p. 553, 2022.

[241] V. N. Solovov *et al.*, "Position reconstruction in a dual phase xenon scintillation detector", *IEEE Trans. Nucl. Sci.*, vol. 59, no. 6, pp. 3286–3293, 2012.

[242] D. S. Akerib *et al.* (LUX Collaboration), "Position reconstruction in LUX", *J. Instrum.*, vol. 13, no. 02, P02001, 2018.

[243] G. Cowan *et al.*, "Asymptotic formulae for likelihood-based tests of new physics", *Eur. Phys. J. C*, vol. 71, pp. 1–19, 2011.

[244] D. Baxter *et al.*, “Recommended conventions for reporting results from direct dark matter searches”, *Eur. Phys. J. C*, vol. 81, pp. 1–19, 2021.

[245] D. S. Akerib *et al.* (LZ Collaboration), “Projected sensitivity of the LUX-ZEPLIN experiment to the two-neutrino and neutrinoless double β decays of ^{134}Xe”, *Phys. Rev. C*, vol. 104, p. 065 501, 2021.

[246] S. Valkiers *et al.*, “A primary xenon isotopic gas standard with SI traceable values for isotopic composition and molar mass”, *Int. J. Mass Spectron.*, vol. 173, no. 1-2, pp. 55–63, 1998.

[247] D. S. Akerib *et al.* (LZ Collaboration), “Projected sensitivity of the LUX-ZEPLIN experiment to the $0\nu\beta\beta$ decay of ^{136}Xe”, *Phys. Rev. C*, vol. 102, p. 014 602, 2020.

[248] J. Aalbers *et al.* (LZ Collaboration), “Background determination for the LUX-ZEPLIN dark matter experiment”, *Phys. Rev. D*, vol. 108, no. 1, p. 012 010, 2022.

[249] *International Atomic Energy Agency (IAEA) LiveChart of Nuclides database.*

[250] D. Khaitan, “Signal processing and electronic noise in LZ”, *J. Instrum.*, vol. 11, no. 03, p. C03029, 2016.

[251] D. S. Akerib *et al.* (LUX Collaboration), “Calibration, event reconstruction, data analysis, and limit calculation for the LUX dark matter experiment”, *Phys. Rev. D*, vol. 97, p. 102 008, 2018.

[252] T. Doke *et al.*, “Absolute Scintillation Yields in Liquid Argon and Xenon for Various Particles”, *Jap. J. Appl. Phys.*, vol. 41, pp. 1538–1545, 2002.

[253] D. S. Akerib *et al.* (LUX Collaboration), “Radiogenic and muon-induced backgrounds in the LUX dark matter detector”, *Astropart. Phys.*, vol. 62, pp. 33–46, 2015.

[254] A. N. Kolmogorov, “Sulla determinazione empirica di una legge didistribuzione”, *Giorn Dell’inst Ital Degli Att*, vol. 4, pp. 89–91, 1933.

[255] N. V. Smirnov, “On the probabilities of large deviations”, *Mat. Sb.*, vol. 40, pp. 443–454, 1933.

[256] H. Dembinski *et al.*, *scikit-hep/iminuit*, version v2.22.0, If you use this software, please cite it using the metadata from this file and the MINUIT paper at https://doi.org/10.1016/0010-4655(75)90039-9. This software includes source code under other licenses, see LICENSE in the repository for details., 2023.

[257] F. James and M. Roos, “Minuit: A System for Function Minimization and Analysis of the Parameter Errors and Correlations”, *Comput. Phys. Commun.*, vol. 10, pp. 343–367, 1975.

[258] R. Barlow, “Extended maximum likelihood”, *Nucl. Instrum.*, vol. 297, no. 3, pp. 496–506, 1990.

[259] G. Cowan, “Chapter 6: The method of maximum likelihood”, in *Statistical Data Analysis*, Oxford University Press, 1998.

[260] S. Baker and R. D. Cousins, “Clarification of the use of chi-square and likelihood functions in fits to histograms”, *Nucl. Instrum.*, vol. 221, no. 2, pp. 437–442, 1984.

[261] F. James and M. Roos, "Interpretation of the Errors on Parameters as given by MINUIT, supplement to long write-up of routine D506 (1978)", 1989.

[262] D. C. Malling *et al.*, "Dark Matter Search Backgrounds from Primordial Radionuclide Chain Disequilibrium", 2013.

[263] A. P. Meshik *et al.*, "Weak decay of ^{130}Ba and ^{132}Ba: Geochemical measurements", *Phys. Rev. C*, vol. 64, p. 035 205, 2001.

[264] M. Pujol *et al.*, "Xenon in Archean barite: Weak decay of ^{130}Ba, mass-dependent isotopic fractionation and implication for barite formation", *Geochim. Cosmochim. Acta*, vol. 73, no. 22, pp. 6834–6846, 2009.

[265] Y. M. Gavrilyuk *et al.*, "Indications of $2\nu 2K$ capture in ^{78}Kr", *Phys. Rev. C*, vol. 87, p. 035 501, 2013.

[266] S. S. Ratkevich *et al.*, "Comparative study of the double-K-shell-vacancy production in single- and double-electron-capture decay", *Phys. Rev. C*, vol. 96, p. 065 502, 2017.

[267] E. Aprile *et al.* (XENON Collaboration), "Observation of two-neutrino double electron capture in ^{124}Xe with XENON1T", *Nature*, vol. 568, no. 7753, pp. 532–535, 2019.

[268] E. Aprile *et al.* (XENON Collaboration), "Double-weak decays of ^{124}Xe and ^{136}Xe in the XENON1T and XENONnT experiments", *Phys. Rev. C*, vol. 106, p. 024 328, 2022.

[269] J. Suhonen, "Double beta decays of ^{124}Xe investigated in the QRPA framework", *J. Phys. G*, vol. 40, p. 075 102, 2013.

[270] C. Wittweg *et al.*, "Detection prospects for the second-order weak decays of ^{124}Xe in multi-tonne xenon time projection chambers", *Eur. Phys. J. C*, vol. 80, no. 12, p. 1161, 2020.

[271] D. S. Akerib *et al.* (LZ Collaboration), "Projected sensitivities of the LUX-ZEPLIN experiment to new physics via low-energy electron recoils", *Phys. Rev. D*, vol. 104, p. 092 009, 2021.

[272] J. Aalbers *et al.* (LZ Collaboration), "A search for new physics in low-energy electron recoils from the first LZ exposure", Jul. 2023.

[273] D. A. Nesterenko *et al.*, "Double-β transformations in isobaric triplets with mass numbers $\mathbf{A} = \mathbf{124}$, 130, and 136", *Phys. Rev. C*, vol. 86, p. 044 313, 2012.

[274] D. S. Akerib *et al.* (LUX Collaboration), "Search for two neutrino double electron capture of ^{124}Xe and ^{126}Xe in the full exposure of the LUX detector", *J. Phys. G*, vol. 47, no. 10, p. 105 105, 2020.

[275] R. Jenkins *et al.*, "Nomenclature system for X-ray spectroscopy", *Pure Appl. Chem.*, vol. 63, no. 5, pp. 735–746, 1991.

[276] F. P. Larkins, "Semiempirical Auger-electron energies for elements $10 \leq Z \leq 100$", *At. Data Nucl. Data Tables*, vol. 20, no. 4, pp. 311–387, 1977.

[277] J. R. De Laeter *et al.*, "Atomic weights of the elements. Review 2000 (IUPAC Technical Report)", *Pure Appl. Chem.*, vol. 75, no. 6, pp. 683–800, 2003.

[278] L. W. Kastens *et al.*, "Calibration of a liquid xenon detector with $^{83\mathrm{m}}$Kr", *Phys. Rev. C*, vol. 80, no. 4, p. 045 809, 2009.

[279] D. S. Akerib *et al.* (LUX Collaboration), "Ultralow energy calibration of LUX detector using ^{127}Xe electron capture", *Phys. Rev. D*, vol. 96, p. 112 011, 2017.

[280] M.-M. Bé *et al.*, *Table of radionuclides (Vol. 6 – A = 22 to 242)*, 2011.

[281] R. D. Deslattes *et al.*, "X-ray transition energies: new approach to a comprehensive evaluation", *Rev. Mod. Phys.*, vol. 75, pp. 35–99, 2003.

[282] A. Thompson *et al.*, *X-ray data booklet*, 2009.

[283] J. Katakura, "Nuclear Data Sheets for A = 125", *Nucl. Data Sheets*, vol. 112, no. 3, pp. 495–705, 2011.

[284] M.-M. Bé *et al.*, *Table of radionuclides (Vol. 8 – A = 41 to 198)*, 2016.

[285] M. Bhike *et al.*, "Comprehensive sets of ^{124}Xe(n,γ) ^{125}Xe and ^{124}Xe$(n,2n)$ ^{123}Xe cross-section data for assessment of inertial-confinement deuterium-tritium fusion plasma", *Phys. Rev. C*, vol. 91, p. 011 601, 2015.

[286] B. N. Laboratory, *Evaluated Nuclear Data File (ENDF) Retrieval Plotting.*

[287] S. F. Mughabghab, "Thermal neutron capture cross sections resonance integrals and g-factors", 2003.

[288] A. Best *et al.*, "Low energy neutron background in deep underground laboratories", *Nucl. Instrum.*, vol. 812, pp. 1–6, 2016.

[289] G. Cowan *et al.*, "Asymptotic formulae for likelihood-based tests of new physics", *Eur. Phys. J. C*, vol. 71, pp. 1–19, 2011.

[290] E. A. Coello Pérez, J. Menéndez, and A. Schwenk, "Two-neutrino double electron capture on ^{124}Xe based on an effective theory and the nuclear shell model", *Phys. Lett. B*, vol. 797, p. 134 885, 2019.

[291] P. Pirinen and J. Suhonen, "Systematic approach to β and $2\nu\beta\beta$ decays of mass A =100–136 nuclei", *Phys. Rev. C*, vol. 91, no. 5, p. 054 309, 2015.

[292] E. Aprile *et al.* (XENON Collaboration), "Search for two-neutrino double electron capture of ^{124}Xe with XENON100", *Phys. Rev. C*, vol. 95, no. 2, p. 024 605, 2017.

[293] K. Abe *et al.* (XMASS Collaboration), "Improved search for two-neutrino double electron capture on ^{124}Xe and ^{126}Xe using particle identification in XMASS-I", *PTEP*, no. 5, p. 053D03, 2018.

[294] K. Bloom *et al.*, "Climate impacts of particle physics", 2022.

[295] G. Karagiorgi *et al.*, "Machine learning in the search for new fundamental physics", *Nat. Rev. Phys.*, vol. 4, no. 6, pp. 399–412, 2022.